UNIVERSITY OF SOUTH BOHEMIA
INSTITUTE OF PHYSICAL BIOLOGY
Department of Structure and Function of Proteins

M.Sc. Peter Palenčár

THE THEORETICAL STUDY
of Photosystem II, Chlorosomes and Flavoprotein WrbA

DOCTORAL DISSERTATION

Supervisor:
M.Sc. Michal Kutý, Ph.D.
Dept. of Structure and Function of Proteins
University of South Bohemia

Nové Hrady, 2007

Prohlašuji, že svoji disertační práci jsem vypracoval samostatně pouze s použitím pramenů a literatury uvedených v seznamu citované literatury.

Prohlašuji, že v souladu s § 47b zákona č. 111/1998 Sb. v platném znění souhlasím se zveřejněním své disertační práce, a to v nezkrácené podobě elektronickou cestou ve veřejně přístupné části databáze STAG provozované Jihočeskou univerzitou v Českých Budějovicích na jejích internetových stránkách.

V Nových Hradech 09/09/2007 Podpis studenta

“Computers are useless, they only give us answers.”

(Gaussian 98 log file)

Za výber náročnej ale zaujímavej témy dizertačnej práce, za množstvo užitočných rád a konzultácií, a tiež za príjemné pracovné prostredie ďakujem môjmu školiteľovi Michalovi Kutému. Osobitná vďaka patrí Frantovi Váchovi a Jakubovi Pšenčíkovi. Vďaka i Vám milí priatelia študenti, sympatickí ľudia z vrátnice a kamaráti zo športových aktivít. V neposlednom rade by som sa rád poďakoval týmto fajn ľudom, Rudi Ettrich, Dalibor Štys, Marcelka Pokorná, Ivana Kutá Smatanová, Otakar Jelínek, Tomáš Polívka, Karel Roháček, Petr Hamberger, Petr Chvosta, Dáša Kaftanová a Lucka Račáková.

Život je krásny vďaka Tebe moja Ivanka.

ABSTRACT

The power of the current computer clusters allows us to study relatively large biomolecular systems by theoretical computational methods, such as widely used classical molecular dynamics (MD) simulations, at atomic level on the time scale of tens of nanoseconds. The limiting factor for classical MD simulations on most of the physiologically relevant systems is the lack of available force field (FF) parameters. Three biomolecular systems were studied in this thesis, namely membrane protein photosystem II (PSII), green bacteria antennas called chlorosomes and flavoprotein WrbA from *E. coli*, and all of them contain molecules or molecular fragments for which no FF parameters are available. Therefore, development of new FF parameters for all non-protein molecules was performed by applying quantum-mechanics (QM) methods. Once all FF parameters were available, MD simulations were applied. The computational studies were based on the conditions from wet experiments performed earlier by our research group. For the first time, proposed light-induced conformational changes of the reaction center (RC) of PSII and subsequent changes in arrangement of PSII RC pigments, were confirmed and described at atomic level by series of MD simulations over 20 ns. Optical spectra calculated on equilibrated MD model of PSII RC were in better agreement with experimental analogues when compared with earlier calculations on static model of PSII RC taken from crystal structure. Successful application of classical mechanics, QM and advanced optical spectra calculations on PSII represents one of a few existing computational studies on similar membrane pigment-protein systems. In the case of chlorosomes, equilibrated molecular lamellar models were constructed and critical structural parameters were elucidated by series of MD simulations over 30 ns. The presented models are the first lamellar models of chlorosomes at such scale so far. The equilibrated MD models of flavoprotein WrbA based on recent crystal structure provides starting point for further theoretical studies aimed to elucidate structural details of proposed ping-pong mechanism.

ABSTRAKT

Vďaka narastajúcemu výkonu dnešných počítačov je možné študovať relatívne veľké bio-molekulárne systémy pomocou výpočtových metód, akou je aj rozšírená klasická molekulárna dynamika (MD), v časových škálach desiatok nanosekúnd. Faktorom, obmedzujúcim použitie metód MD na štúdium väčšiny fyziologicky relevantných systémov, je nedostatok kvalitných parametrov silového poľa (SP). Všetky tri bio-molekulárne systémy, ktoré boli predmetom štúdia, membránový pigment-proteínový komplex fotosystému II (FSII), chlorozómy zelených baktérií a flavoproteín WrbA, obsahujú molekuly a molekulárne fragmenty, pre ktoré nie sú dostupné parametre SP. Na výpočet nových parametrov SP pre tieto molekuly a fragmenty boli využité metódy kvantovej mechaniky (KM). Po získaní všetkých parametrov SP boli prevádzané MD simulácie. Základom pre všetky tri výpočtové projekty boli predošlé experimentálne práce našej skupiny. Po prvý krát, boli potvrdené a objasnené svetlom-indukované konformačné zmeny v reakčnom centre (RC) FSII a tiež následné zmeny v postavení pigmentov z RC FSII na úrovni jednotlivých molekúl a atómov za pomoci MD simulácií v dĺžke 20 ns. Optické spektrá, ktoré boli počítané na modeloch RC FSII získané z MD simulácií boli v lepšej zhode s experimentom v porovnaní so spektrami počítanými na statických modeloch RC FSII z kryštalických štruktúr. Kombinácia metód klasickej mechaniky, KM a výpočtov optických spektier na FSII je úspešným príkladom z mála podobných štúdií. V rámci druhého projektu, boli pripravené ekvilibrované lamelárne modely chlorozómov, ktoré boli podrobené MD simuláciám v dĺžke 30 ns, s cieľom objasniť kritické štruktúrne parametre. Prezentované modely predstavujú vôbec prvé takéto MD modely v takom rozsahu. Ekvilibrované MD modely flavoproteínu WrbA boli pripravené s využitím novej kryštalickej štruktúry, a budú ďalej využité na teoretické štúdium zamerané na objasnenie navrhnutého ping-pong mechanizmu.

ABBREVIATIONS *(alphabetically)*

ACE – acetyl (CH_3-CO-) N-terminal cap group
ADP – adenosine diphosphate
ATP – adenosine triphosphate
***β*-Car –** *β*-carotene
B3LYP - Becke3LYP (Becke, Lee, Yang, Parr) hybrid functional
BCT – bicarbonate ion
BChl *c* – bacteriochlorophyll *c*
BOPES – Born-Oppenheimer potential energy surface
Car – carotene
CASP – critical assessment of techniques for protein structure prediction
CBE – chlorobactene
CD – circular dichroism
D1 – PSII protein subunit A, *psbA* gene product
D2 – PSII protein subunit D, *psbD* gene product
DFT – density functional theory
DNA – deoxyribonucleic acid
Eq-PSII RC – equilibrated photosystem II
ES – electrochromic shift
FAD – flavin adenine dinucleotide
FF – force field
FMN – flavin mononucleotide
FMO – fragment molecular orbital method
FMR – double-reduced flavin mononucleotide
FMS – oxidized flavin mononucleotide
FWHM – full-width at half maximum
GAFF – general Amber force field,
H-bond – hydrogen bond
HF – Hartree-Fock
Chl *a* – chlorophyll *a*
LJ – Lennard-Jones
LSDA – local spin density approximation
MD – molecular dynamics
MM – molecular modeling
MO-LCAO – molecular orbitals defined by linear combination of atomic orbitals
NADP – nicotinamide adenine dinucleotide phosphate
Neutral-MD – molecular dynamics of PSII RC with neutral pigments
NME – (CH_3-NH-) C-terminal cap group
NMR – nuclear magnetic resonance
NPT – Canonical ensemble (constant Number, Pressure, Temperature)
NVT – Canonical ensemble (constant Number, Volume, Temperature)
OEC – oxygen evolving complex
P680 – specialized chlorophyll of the photosystem II reaction center (excited by photon of 680 nm wavelength)
P700 – specialized chlorophyll of the photosystem I reaction center (excited by photon of 700 nm wavelength)
PDB ID – identification code from protein data bank *www.pdb.org*
PES – potential energy surface
Pheo *a* – pheophytin *a*
Pheo-D1 – primary electron acceptor of photosystem II reaction center
Pheo$^-$-MD – molecular dynamics of PSII RC with reduced Pheo-D1
PQ9 – plastoquinone 9
PSI – photosystem I
PSII – photosystem II
PSII RC pigments – Chl-*a*-3, Chl-*a*-4, Chl-*a*-5, Chl-*a*-6, Pheo-*a*-7, Pheo-*a*-8, Chl-*a*-9 and Chl-*a*-10
PWD – potential well depth
QM – quantum mechanics
RC – reaction center
RESP – restrained electrostatic potential
RMSD – root-mean-square deviation
RMSF – root-mean-square fluctuation
RNA – ribonucleic acid
SAXS – small-angle X-ray scattering
vdW – van der Waals
WAXS – wide angle X-ray scattering
WrbA – tryptophan (W) repressor-binding protein
YASARA – Yet Another Scientific Artificial Reality Application

TABLE OF CONTENTS

A. STUDIED SYSTEMS – INTRODUCTION

A.1. PHOTOSYSTEM II AND CHLOROSOMES

A.1.1. Photosynthesis – What is Photosynthesis?

The most active photosynthetic tissue in higher plants is the mesophyll of leaves. Mesophyll cells have many chloroplasts, which contain the specialized light-absorbing green pigments, the chlorophylls. In photosynthesis, the plant uses solar energy to oxidize water, thereby releasing oxygen, and to reduce carbon dioxide, thereby forming large carbon compounds, primarily sugars. The complex series of reactions that culminate in the reduction of CO_2 include the thylakoid reactions and the carbon fixation reactions [Garab 1996].

A.1.1.1. Introduction to Photosynthesis – Location of Photosynthesis

The thylakoid reactions of photosynthesis take place in the specialized internal membranes of the chloroplast called thylakoids (Figure A-1). The end products of these thylakoid reactions are the high-energy compounds ATP and NADPH, which are used for the synthesis of sugars in the carbon fixation reactions. These synthetic processes take place in the stroma of the chloroplasts, the aqueous region that surrounds the thylakoids. As the main topic of the thesis is a theoretical study of the so-called light (light-induced) reactions of photosynthesis, also the main part of the A1 section is devoted to this field.

In the chloroplast, light energy is converted into chemical energy by two different functional units called photosystems. The absorbed light energy is used to power the transfer of electrons through a series of compounds that act as electron donors and electron acceptors. The majority of electrons ultimately reduces $NADP^+$ to NADPH and oxidizes H_2O to O_2. Light energy is also used to generate a proton motive force across the thylakoid membrane, which is used to synthesize ATP.

A.1.1.2. Photosynthetic Organelle – Chloroplast

In photosynthetic eukaryotes, photosynthesis takes place in the subcellular organelle known as the chloroplast. The most striking aspect of the structure of the chloroplast is the extensive system of internal membranes known as thylakoids. All the chlorophylls are contained within this membrane system, which is the site of the light reactions of photosynthesis. The carbon reduction reactions, which are catalyzed by water-soluble enzymes, take place in the stroma, the region of the chloroplast outside the thylakoids. Most of the thylakoids appear to be very closely associated with each other. These stacked membranes are known as grana lamellae and the exposed membranes in which stacking is absent are known as stroma lamellae. Two separate membranes, each composed of a lipid bilayer and together known as the envelope, surround most types of chloroplasts (Figure A-1).

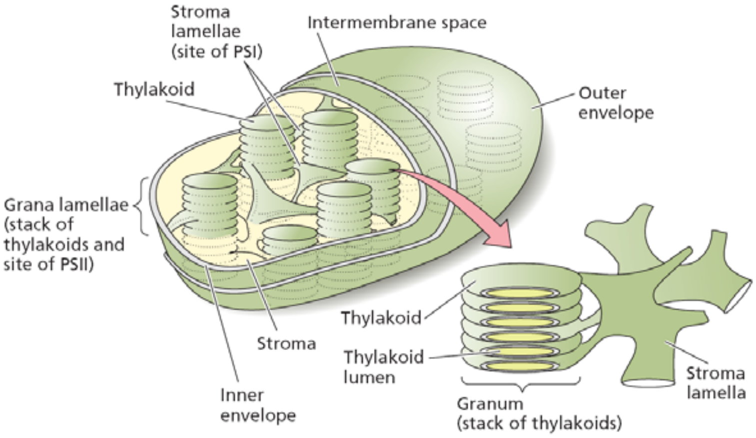

Figure A-1. Schematic picture of the overall organization of the membranes in the chloroplast. The chloroplast of higher plants is surrounded by the inner and outer membranes (envelope). The region of the chloroplast that is inside the inner membrane and surrounds the thylakoid membranes is known as the stroma. It contains the enzymes that catalyze carbon fixation and other biosynthetic pathways. The thylakoid membranes are highly folded and appear in many pictures to be stacked like coins (the granum), although in reality they form one or a few large interconnected membrane systems, with a welldefined interior and exterior with respect to the stroma. The inner space within a thylakoid is known as the lumen. (After Becker 1986.)

This double-membrane system contains a variety of metabolite transport systems. The chloroplast also contains its own DNA, RNA, and ribosomes. Some of the chloroplast proteins are products of transcription and translation within the chloroplast itself, whereas most of the others are encoded by nuclear DNA, synthesized on cytoplasmic ribosomes, and then imported into the chloroplast.

A.1.1.3. Chemical Reaction of Photosynthesis

Establishing the overall chemical equation of photosynthesis required several hundred years and contributions by many scientists. In 1771, Joseph Priestley observed that a sprig of mint growing in air in which a candle had burned out improved the air so that another candle could burn. He had discovered oxygen evolution by plants. A Dutchman, Jan Ingenhousz, documented the essential role of light in photosynthesis in 1779. Other scientists established the roles of O_2 and H_2O and showed that organic matter, specifically carbohydrate, is a product of photosynthesis along with oxygen. By the end of the nineteenth century, the balanced overall chemical reaction for photosynthesis could be written as follows:

$$6\ CO_2 + 6\ H_2O \rightarrow \text{light, plant} \rightarrow C_6H_{12}O_6 + 6\ O_2,$$

where $C_6H_{12}O_6$ represents a simple sugar such as glucose. The glucose is not the actual product of the carbon fixation reactions. However, the energetics for the actual products is approximately the same. The chemical reactions of photosynthesis are complex. In fact, at least 50 intermediate reaction steps have now been identified, and undoubtedly additional steps will be discovered. An early clue to the chemical nature of the essential chemical process of photosynthesis came in the 1920s from investigations of photosynthetic bacteria that did not produce oxygen as an end product. From his studies on these bacteria, C. B. van Niel concluded that photosynthesis is a redox process. This conclusion has served as a fundamental concept on which all subsequent research on photosynthesis has been based.

In 1988 the German scientists Deisenhofer, Huber and Michel received the Nobel Price for identifying the spatial structure of the photosynthesis reaction center. The structure of so-called RC, the key element of photosynthesis, was identified by using X-ray diffraction.

Rudolph A. Marcus was awarded the 1992 Nobel Prize in Chemistry. Marcus's theory explains the transfer of an electron between two molecules. The simplicity of Dr. Marcus's theory belies a host of practical consequences that extend over all areas of chemistry, ranging from photosynthesis, photochemical production of fuel, solar power, chemiluminescence ("cold light"), and electrically conducting polymers, to electrochemical synthesis and such commonplace concerns as battery technology and corrosion.

In 1997 American biochemist Paul D. Boyer who, with British chemist John E. Walker, was awarded the Nobel Prize for Chemistry for their explanation of the enzymatic process involved in the production of the energy-storage molecule adenosine triphosphate (ATP), which fuels the metabolic processes of the cells of all living things.

A.1.1.4. Primary Photochemistry – Four Pathways for Energy Disposing

Chlorophyll appears green to our eyes because it absorbs light mainly in the red and blue parts of the spectrum, so only some of the light within the green wavelengths (about 550 nm) is reflected into our eyes (Figure A-2).

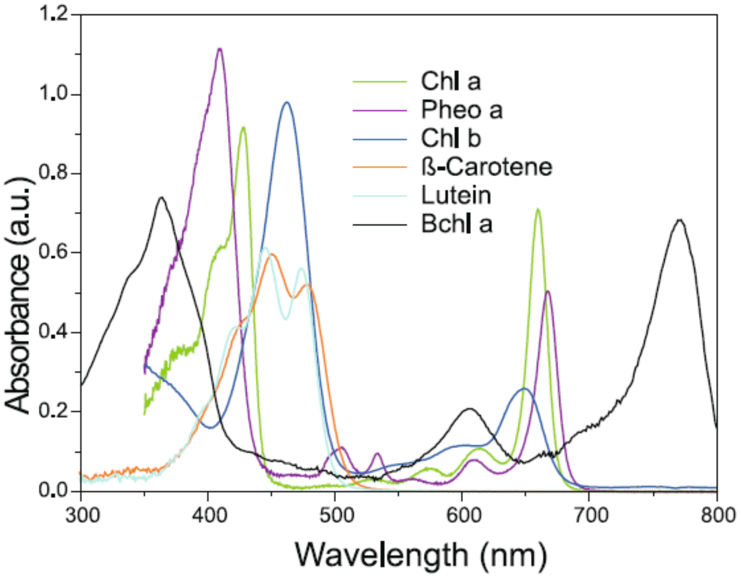

Figure A-2. Absorption spectra of some photosynthetic pigments. Abbreviations used in the figure are as follows, Chl *a* - chlorophyll *a*, Pheo *a* - pheophytin *a*, Chl *b* - chlorophyll *b* and Bchl *a* - bacteriochlorophyll *a*. The absorption spectra shown are for pure pigments (dissolved mainly in nonpolar solvents).

The absorption of light is represented by the equation below, in which chlorophyll (Chl) in its lowest-energy, or ground state, absorbs a photon (represented by $h\nu$) and makes a transition to a higher-energy, or excited, state (Chl^*)

$$Chl + h\nu \rightarrow Chl^*.$$

The distribution of electrons in the excited molecule is somewhat different from the distribution in the groundstate molecule. In the higher excited state, chlorophyll is extremely unstable, very rapidly gives up some of its energy to the surroundings as heat, and enters the lowest excited state, where it can be stable for a maximum of several nanoseconds (10^{-9} s). Because of this inherent instability of the excited state, any process that captures its energy must be extremely rapid [Diner and Rappaport 2002]. In the lowest excited state, the excited chlorophyll has four alternative pathways for disposing of its available energy.

a) Excited chlorophyll can emit a photon and thereby return to its ground state – a process known as fluorescence (Figure A-3). The wavelength of fluorescence is slightly longer than the wavelength of absorption, due to conversion of part of energy into heat.

b) Excited chlorophyll can return to its ground state by directly converting its excitation energy into heat (Figure A-3), with no emission of a photon.

c) Chlorophyll may participate in energy transfer, during which an excited chlorophyll transfers its energy to another molecule.

d) A fourth process is photochemistry, which is the crucial process at the early steps of photosynthesis. The photochemical reactions are extremely fast to compete with the three other possible reactions of the excited state just described.

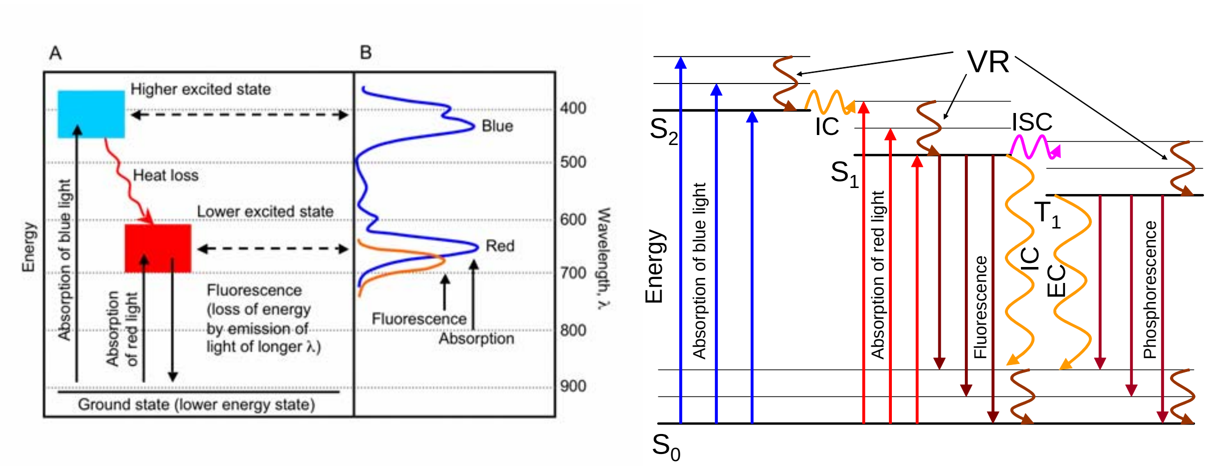

Figure A-3. Light absorption and emission by chlorophyll with highlighted fluorescence (left) and general scheme of Jablonsky diagram (right). Abbreviations used: S_0 - ground singlet state, S_1 - lowest excited state, S_2 - higher excited state, T_1 - lowest triplet state, IC and EC - internal conversion (heat), ISC - intersystem crossing, VR - vibrational relaxation.

A.1.1.5. Photosynthetic Pigments

The energy of sunlight is first absorbed by the pigments. Structures of several photosynthetic pigments [Warshel and Parson 1987] are shown in Figure A-4. The chlorophylls and bacteriochlorophylls (pigments found in certain bacteria) are the typical pigments of photosynthetic organisms, but all organisms contain a mixture of more than one kind of pigment, each serving a specific function. Chlorophylls *a* and *b* are abundant in green plants, and *c* and *d* are found in some protists and cyanobacteria. The bacteriochlorophyll type *a* is the most widely distributed in bacteria. All chlorophylls have a complex ring structure that is chemically related to the porphyrin-like groups found in hemoglobins and cytochromes. In addition, a long hydrocarbon tail is almost always attached to the ring structure. The tail anchors the chlorophyll to the protein matrix. The ring structure contains some loosely bound electrons and is the part of the molecule involved in electron transitions and redox (reduction–oxidation) reactions. The various types of carotenoids found in photosynthetic organisms are all linear molecules with multiple conjugated double bonds (Figure A-4). Carotenoids are found in all photosynthetic organisms, except for mutants incapable of living outside the laboratory. Carotenoids are integral constituents of the thylakoid membrane usually attached to photosynthetic proteins. The light absorbed by the carotenoids is transferred to chlorophyll for photosynthesis; because of this role they are called accessory pigments. Carotenoids also help protect the organism from damage caused by light.

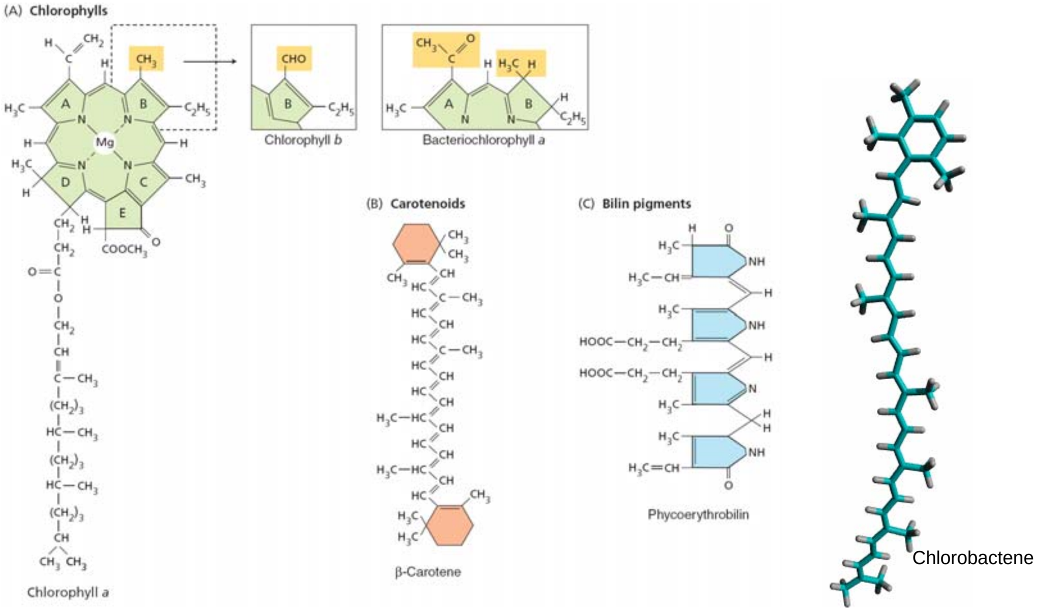

Figure A-4. Molecular structure of some photosynthetic pigments. (A) The chlorophylls *a*, *b* and bacteriochlorophyll *a*. Various chlorophylls differ particularly in the substituents around the porphyrin-like rings and the pattern of double bonds. (B) Carotenoids are linear polyenes that serve as both antenna pigments and photoprotective agents. (C) Bilin pigments are open-chain tetrapyrroles found in antenna structures known as phycobilisomes that occur in cyanobacteria and red algae. (After Taiz and Zeiger 2006.) Molecule of chlorobactene is shown as real structure optimized by *ab initio* calculations in Gaussian. Structures of other photosynthetic pigments such as plastoquinone 9, bacteriochlorophyll *c* and pheophytin *a* are shown in the *Results* chapter.

A.1.1.6. Photosystem I and II – Z scheme

Photosystems I and II (PSI and PSII), operate in series to carry out the early energy storage reactions of photosynthesis [Grossman et al. 1995; Green and Durnford 1996; Green and Parson 2003]. PSI preferentially absorbs far-red light of wavelengths greater than 680 nm; PSII preferentially absorbs red light of 680 nm. The scheme of photosynthesis depicted in Figure A-5, called the Z scheme, has become the basis for understanding O_2-evolving photosynthetic organisms.

PSI produces a strong reductant, capable of reducing $NADP^+$, and a weak oxidant. PSII produces a very strong oxidant, capable of oxidizing water, and a weaker reductant than the one produced by PSI.

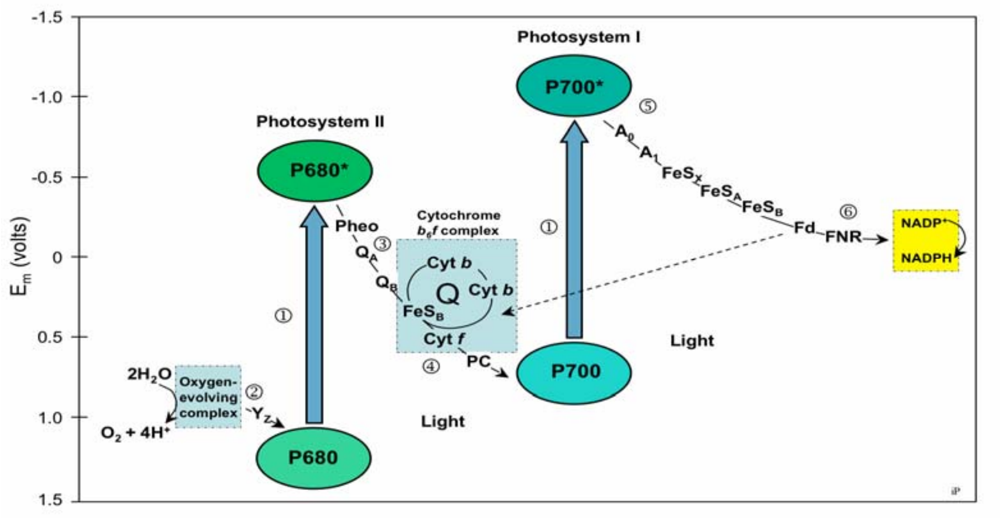

Figure A-5. Detailed Z scheme for O_2-evolving photosynthetic organisms. The redox carriers are placed at their midpoint redox potentials (at pH 7). (1) The vertical arrows represent photon absorption by the reaction center chlorophylls: P680 for photosystem II (PSII) and P700 for photosystem I (PSI). The excited PSII reaction center chlorophyll, P680*, transfers an electron to pheophytin (Pheo). (2) On the oxidizing side of PSII (to the left of the arrow joining P680 with P680*), P680 oxidized by light is re-reduced by Y_Z, that has received electrons from oxidation of water. (3) On the reducing side of PSII (to the right of the arrow joining P680 with P680*), pheophytin transfers electrons to the acceptors Q_A and Q_B, which are plastoquinones. (4) The cytochrome b6f complex transfers electrons to plastocyanin (PC), a soluble protein, which in turn reduces $P700^+$ (oxidized P700). (5) The acceptor of electrons from P700* (A0) is thought to be a chlorophyll, and the next acceptor (A1) is a quinone. A series of membrane-bound iron–sulfur proteins (FeS_X, FeS_A, and FeS_B) transfers electrons to soluble ferredoxin (Fd). (6) The soluble flavoprotein ferredoxin–NADP reductase (FNR) reduces $NADP^+$ to NADPH, which is used in the Calvin cycle to reduce CO_2. The dashed line indicates cyclic electron flow around PSI. (After Blankenship and Prince 1985.)

A.1.1.7. Primary Photochemistry - Electron Transport

Photons excite the specialized chlorophylls of the reaction centers (P680 for PSII, and P700 for PSI), and an electron is ejected. The first reaction that converts electron energy into chemical energy—that is, the primary photochemical event—is the transfer of an electron from the excited state of a chlorophyll in the reaction center to an acceptor molecule. The electron then passes through a series of electron carriers and eventually reduces P700 (for electrons from PSII) or $NADP^+$ (for electrons from PSI). Immediately after the photochemical event, the reaction center chlorophyll is in an oxidized state (electron deficient, or positively charged), and the nearby electron acceptor molecule is reduced (electron rich, or negatively charged). The system is now in a critical point. The lower-energy orbital of the positively charged oxidized reaction center chlorophyll has a vacancy and can accept an electron. The primary electron acceptor molecule transfers its extra electron to a secondary acceptor and so on down the electron transport chain. The oxidized reaction center of the chlorophyll that had donated an electron is reduced by a secondary donor, which in turn is reduced by a tertiary donor. In plants, the ultimate electron donor is H_2O, and the ultimate electron acceptor is $NADP^+$. The structure of the reaction center appears to be extremely fine-tuned for maximal rates of productive reactions and minimal rates of energy-wasting reactions. Almost all chemical processes, that take part in the light reactions of photosynthesis are carried out by four major protein complexes, all embedded in the thylakoid membrane: PSII, cytochrome b6f, PSI and ATP synthase.

A.1.2. Photosystem II from *Thermosynechococcus elongatus*

Thermosynechococcus elongatus belongs to the family of thermophilic cyanobacteria. Their photosynthetic apparatus is very similar to one found in higher plants, in a sense of its function and structure. Cyanobacteria are in fact prokaryotes that obtain their energy through photosynthesis. The name "cyanobacteria" comes from the colour of the bacteria, cyan. Cyanobacteria are found in almost every conceivable habitat, from oceans to fresh water to bare rock to soil. Cyanobacteria include unicellular and colonial species. Colonies may form filaments, sheets or even hollow balls. Some filamentous colonies show the ability to differentiate into several different cell types: vegetative cells, the normal, photosynthetic cells that are formed under favorable growing conditions; akinetes, the climate-resistant spores that may form when environmental conditions become harsh; and thick-walled heterocysts, which contain the enzyme nitrogenase, vital for nitrogen fixation.

A.1.2.1. Photosynthesis in Cyanobacteria

Photosynthesis in cyanobacteria generally uses water as an electron donor and produces oxygen as a by-product, though some may also use hydrogen sulfide as occurs among other photosynthetic bacteria. Carbon dioxide is reduced to form carbohydrates via the Calvin cycle. The photosynthetic machinery is embedded in thylakoids. The large amounts of oxygen in the atmosphere are considered to have been first created by the activities of ancient cyanobacteria. The water-oxidizing photosynthesis is accomplished by coupling the activity of photosystem II (PSII) and PSI. In anaerobic conditions, they are also able to use only PSI — cyclic photophosphorylation — with electron donors other than water (hydrogen sulfide, thiosulphate, or even molecular hydrogen) just like purple photosynthetic bacteria.

A.1.2.2. Phycobilisomes – Light Harvesting Antennae

Attached to thylakoid membrane, phycobilisomes act as light harvesting antennae for the photosystems. Phycobilisomes are protein complexes (up to 600 polypeptides) anchored to thylakoid membranes. They are made of stacks of chromophorylated proteins (phycobiliproteins; responsible for the blue-green pigmentation of most cyanobacteria) and their associated linkers. Each phycobilisome consists of a core (made of allophycocyanin) from which several outwardly oriented rods made of stacked disks of phycocyanin and (if present) phycoerythrin. The spectral properties of phycobiliproteins are dictated by their prosthetic groups, which are linear tetrapyrroles known as phycobilins, such as phycocyanobilin, phycoerythrobilin, phycobiliviolin etc. Phycobilisomes absorb in the visible range of light. The absorption of light in the 500-650 nm range is particularly advantageous deeper in the water column, where light with longer wavelengths is less transmitted and therefore less available directly to chlorophyll. The geometrical arrangement of a phycobilisome is very elegant and results in 95% efficiency of energy transfer.

A.1.2.3. Evolutionary Relationships with Algae and Higher Plants

Chloroplasts found in eukaryotes (algae and higher plants) likely evolved from an endosymbiotic relation with cyanobacteria. This endosymbiotic theory is supported by various structural and genetic similarities. Primary chloroplasts are found among the green plants, where they contain chlorophyll b, and among the red algae and glaucophytes, where they contain phycobilins. It now appears that these chloroplasts probably had a single origin, in an ancestor of the clade called Primoplantae. Other algae likely took their chloroplasts from these forms by secondary endosymbiosis or ingestion.

A.1.2.4. Structure of Photosystem II from *Thermosynechococcus elongatus*

Crystallographers obtained several medium-resolution structures of cyanobacterial photosystem II (3.8 to 3.2Å) [Zouni et al. 2001; Kamiya and Shen 2003; Ferreira et al. 2004; Biesiadka et al. 2004] that explain the general arrangement of the protein matrix and cofactors. The most complete cyanobacterial photosystem II structure obtained so far is the X-ray structure showing locations of and interactions between 20 protein subunits and 77 cofactors per monomer [Loll et al. 2005]. Further, it contains 11 β-carotenes and 14 integrally bound lipids. The structure also provides information about the Mn_4Ca cluster, where oxidation of water takes place. It uncovers near-atomic details necessary to understand the processes that convert light to chemical energy (Figure A-6). As there is no structure of PSII from higher plants or algae available, the cyanobacterial PSII X-ray structure is used as the most suitable replacement for it.

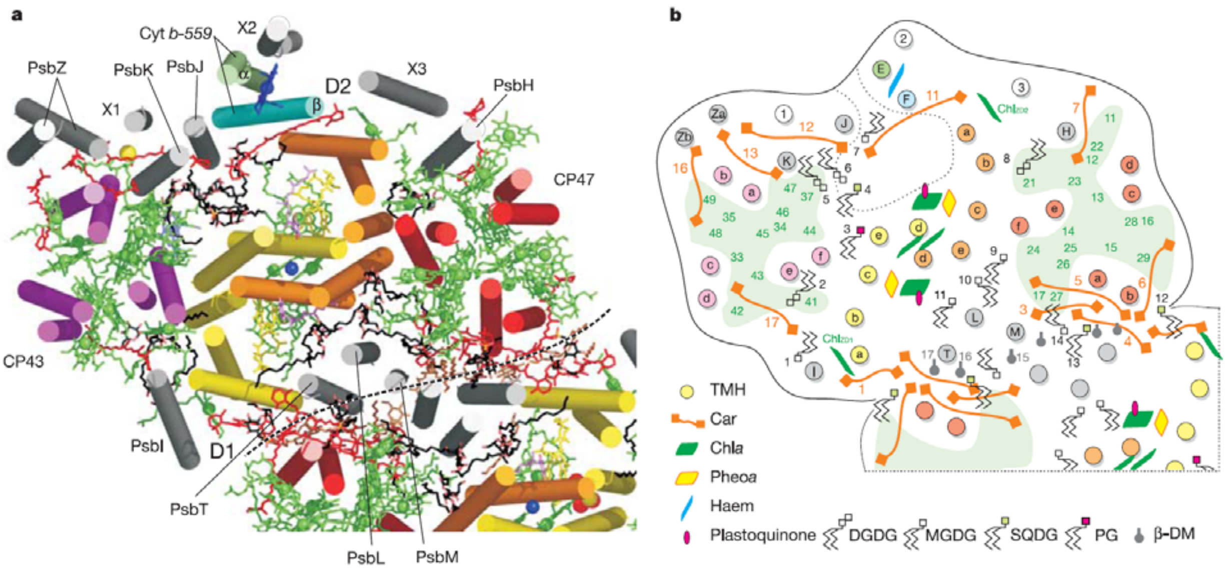

Figure A-6. The PSII monomer from the cytoplasmic side. **a**, Overall view of the PSII monomer. Transmembrane α-helices are represented as cylinders; other protein elements are omitted for clarity. The main subunits are highlighted as follows: reaction centre subunits D1 (yellow) and D2 (orange), antenna subunits CP43 (magenta) and CP47 (red), and the α- and β-chain of cytochrome b-559 (green and cyan, respectively). Low molecular mass subunits are coloured grey. Unassigned TMHs are labelled X1–X3. Cofactors are coloured green (Chl *a*), yellow (Pheo), red (Car), blue (haem), violet (quinone), black (lipids) and brown (detergent and unassigned alkyl chains). The non-haem Fe^{2+} (blue) and putative Ca^{2+} (yellow) ions are shown as spheres. Dashed line indicates the monomer–monomer interface. **b**, Schematic representation of the view in a, with the same colour code. Lipid and detergent molecules with headgroups pointing ‘downwards’ or ‘upwards’ are located at the lumenal or cytoplasmic side, respectively. Green numbers in CP43 and CP47 indicate the positions of antenna Chl *a*. The QB diffusion cavity is indicated by a dotted line. (After Loll et al. 2005.)

A.1.2.5. The Motivation for Theoretical Study

In this section brief information on the subject and idea of the theoretical study of photosystem II (PSII) are given. As mentioned earlier the motivation for the first project presented in the thesis was our previous theoretical study [Vacha et al. 2005], where we provided an explanation of our former experimental results [Vacha et al. 2002] concerned with the reversible bleaching of the absorbance and circular dichroism (CD) spectra upon selective light-induced oxidation of primary electron donor P680. The effects of the light-induced reduction of the primary electron acceptor Pheo-D1 [Vacha et al. 2002] in the presence of artificial electron donor sodium dithionite could be also analyzed by using of similar theoretical approach. It was observed that at high temperature (277 K) the resulted absorbance difference and CD spectrum bleaching were much lower compare to the primary donor oxidation, and that at low temperatures of 77 K, no reversible light-induced change in the CD spectrum was detected. According to the temperature dependence of the light-induced absorbance and CD changes we have suggested that at a room temperature, the reduced Pheo-D1 induces a conformational change in the protein surroundings, and consequently affects the original CD spectrum. These charge-induced processes do not occur at low temperature and, therefore, the reduced form of Pheo-D1 should not affect the CD and absorbance spectra. This hypothesis could be also supported by previous suggestions [Konermann et al. 1997, Dekker and van Grondelle 2000] that the charge-induced processes cause conformational changes of the protein surroundings, which consequently, influence an energy transfer and primary charge separation reactions in the PSII RC [Diner and Rappaport 2002].

Moreover, thanks to the similar theoretical studies using molecular structure-based computational models (Vasil'ev and Bruce 2006; Palencar et al. 2005; Raszewski et al. 2005; Vacha et al. 2005) reported recently, the results obtained in our theoretical study of PSII could be compared and discussed. The methodology used for calculation of optical spectra could be adopted from two principal sources. The point-dipole method (Prokhorenko et al. 2003), which concerns interaction energy between the transition dipole moments, and the point-monopole method (Chang et al. 1977), which describes the interaction energy between transition monopoles. Both approximations are popular for their simplicity and also reliability since they provide optical spectra (absorbance, linear and circular dichroism and triplet-singlet difference absorption) comparable with those obtained from experiments (Vasil'ev and Bruce 2006; Raszewski et al. 2005, Vacha et al. 2005; Barter et al. 2003; Psencik et al. 2003; Jankowiak et al. 2002; Renger and Marcus 2002; Dekker and Grondelle 2000; Pearlstein 1991).

A.1.3. Chlorosomes from Green Sulfur Bacteria

A.1.3.1. Chlorosomes are Light Harvesting Antennae Complexes

Chlorosomes are the biggest and the most efficient light harvesting photosynthetic antennae complexes known in nature. They are found in green sulfur bacteria (*Chlorobiaceae*; e.g. *Chlorobium vibrioforme*, *Chlorobium tepidum*, *Pelodictyon lutoleum* and other), green nonsulfur bacteria, and some green filamentous anoxygenic phototrophs (*Chloroflexaceae*, *Oscillochloridaceae*). They differ from other antenna complexes by their large size and lack of protein matrix supporting the photosynthetic pigments. In fact, chlorosomes are the only known antennae complexes, where the protein framework does not determines pigment orientations and optical properties, and ensures efficient flow of excitation energy to the photosynthetic reaction center.

A.1.3.2. Size and Composition of Chlorosomes

Chlorosomes are ellipsoidal bodies, in green sulfur bacteria their length varies from 100 to 200 nm, width of 50-100 nm and height of 15 - 30 nm [Martinez-Planells et al. 2002], in filamentous anoxygenic phototrophs the chlorosomes are somewhat smaller. Inside the bacteria, chlorosomes are thought to be attached to the reaction centers in the cell membrane via FMO-proteins and a chlorosome baseplate composed of csmA proteins. Chlorosomes from filamentous anoxygenic phototrophs lack the FMO complex (Figure A-7).

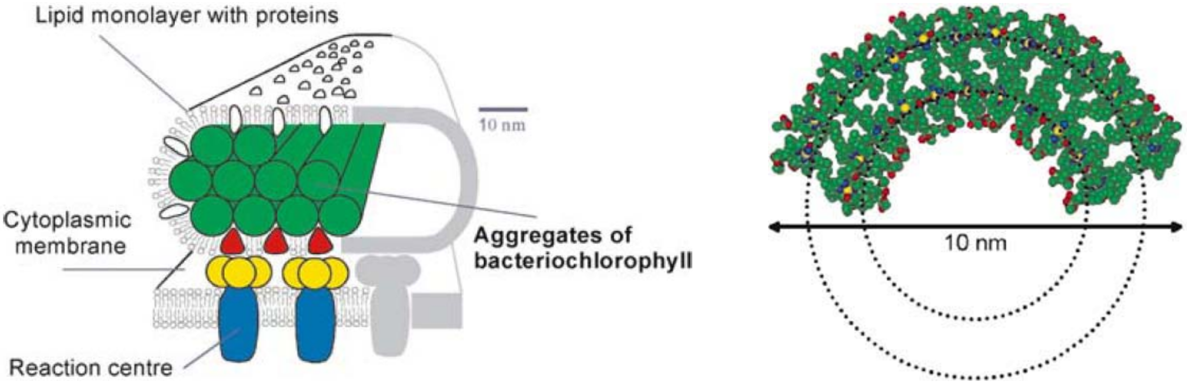

Figure A-7. Schematic view of a model of a chlorosome from *Chlorobium tepidum* sitting on top of the FMO-complex (yellow) which attaches the chlorosomes to the cytoplasmic membrane containing the reaction centres (blue). Green: Rod elements (ca. 10 nm diameter, ca. 400–600 nm length) containing supramolecular aggregates of BChl *c*. The chlorosome is surrounded by a lipid monolayer. This model follows the early electron microscopy picture of [Staehelin et al. 1978; 1980]. (After Balaban et al. 2005.)

The composition of the chlorosomes is mostly bacteriochlorophyll (BChl) with small amounts of carotenoids (Car) and quinones surrounded by a galactolipid enveloping monolayer with ten different proteins (most of the proteins are located in a BChl *a*-containing protein baseplate coupling to the cytoplasmic membrane) attached to it. The aggregates of BChls are organized by pigment-pigment rather than pigment-protein interactions [Blankenship et al. 1995; Frigaard et al. 2003]. A typical chlorosome contains on the order of 10^5 BChls [Montano et al. 2003] (BChl *c*, *d*, *e*, depending on the species) in the form of aggregates. The aggregation modulates the optical properties of the BChls and results in fast energy transfer rates [Psencik et al. 2003], which are a prerequisite for the light harvesting efficiency. The green sulfur bacteria are able to survive at the lowest light conditions of all known photosynthetic organisms [Frigaard et al. 2003]. Current models of the structure of BChl and Car pigments inside the chlorosomes put them in a lamellar organization, where the long farnesol tails of the BChl intermix with carotenoids and each other, forming a structure resembling a lipid multilayer [Psencik et al. 2004].

A.1.3.3. Structure of Chlorosomes

There are two main models representing the structural organization of chlorosomes interior, the rod-like model [Egawa et al. 2007] and lamellar model [Psencik et al. 2004]. The rod-like models, in which BChl pigments are organized into large rods, were proposed on the basis of freeze-fracture electron microscopy (f-f EM) and spectroscopic constraints. The first rod-like model was described by f-f EM study [Staehelin et al. 1978; 1980], in which micrographs of chlorosome interiors were interpreted in terms of rod-like elements with a diameter of 50Å (nonsulfur bacteria) or 100Å (sulfur bacteria). This model became the basis for all other chlorosome models proposed later on [Kakitani et al. 2006, Holzwarth and Schaffner 1994; Blankenship et al. 1995; Van Rossum et al. 2001]. There are two principal groups of models classified according the asymmetric repeating unit:

a) parallel-chain model with BChl monomer as the building block
b) antiparallel double-chain model with an antiparallel BChl dimer as a building block

The antiparallel BChl dimers are also called piggy-back dimers [Nozawa et al. 1994; Wang et al. 1999]. The terms parallel and antiparallel refer to the mutual orientation of the Q_y transition dipoles. The short-range order of BChl molecules was based on the results of NMR and optical spectroscopy [Holzwarth and Schaffner 1994; Nozawa et al. 1994; Balaban et al. 2005; Wang et al. 1999; van Rossum et al. 2001]. See also paper [Egawa et al. 2007] for the newest BChls assembly models. Recently, the first high resolution cryo-electron microscopy (EM) images of intact *Chlorobium tepidum* chlorosomes embedded in vitreous ice were presented [Psencik et al. 2004]. EM was complemented by solution SAXS and WAXS. The data were clearly incompatible with the rod-like model. Both the high-resolution EM images and SAXS (X-ray scattering from chlorosomes) revealed fine internal structure with spacing of ~20Å, which were explained by a simple lamellar organization of pigment molecules (Figure A-8).

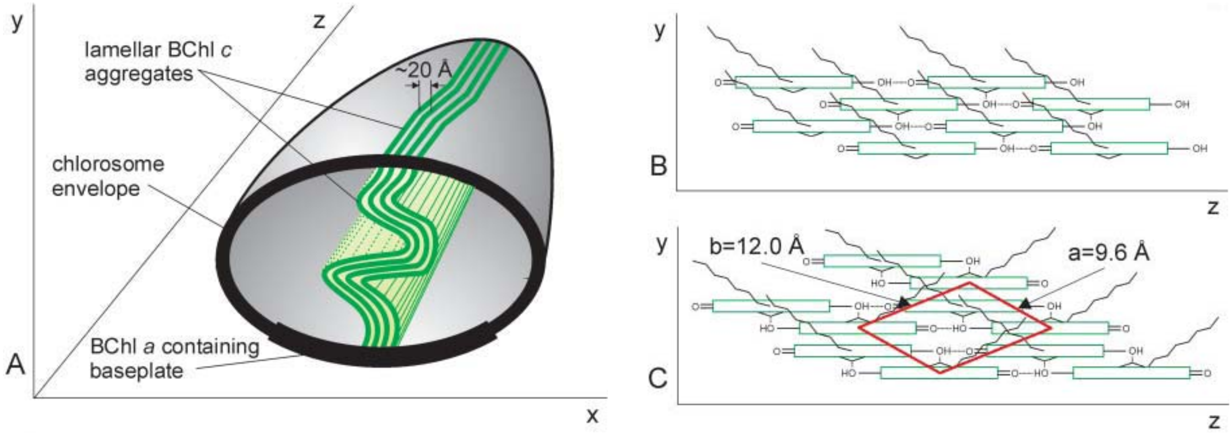

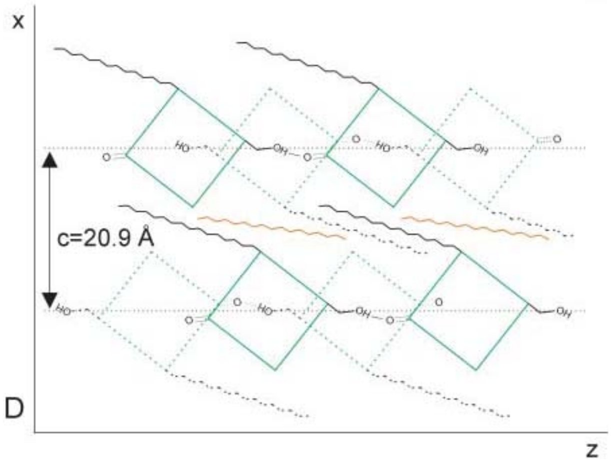

Figure A-8. Schematic model of the BChl aggregates in the chlorosome. (**A**) Arrangement of lamellae inside the chlorosome. Each undulated plane (thick green line) extends in the long axis of the chlorosome (z), and through the height of the chlorosome (y). Planes are arranged into lamellae throughout the chlorosome (x). Only a few lamellae are depicted for clarity. Model of one plane of BChl aggregate with parallel (**B**) or antiparallel (**C**) pigment configuration. Coordinate system as in panel A. The monoclinic unit cell projection and lattice constants are shown in red. (**D**) Top view of chlorin (green) planes (antiparallel configuration) associated via interdigitated esterifying alcohol tails (black). An underlying layer of BChl molecules is shown dotted whereas carotenoids (orange) are interspersed between the alcohol tails. (After Psencik et al. 2004.)

A lamellar model is formed by BChls aggregated into semicrystalline lateral arrays. From diffraction data it was predicted that arrays are built from BChl dimers. The arrays form undulating lamellae, which, in turn, are held together by interdigitated esterifying alcohol tails, carotenoids, and lipids. The lamellar model immediately invoked scientific discussion and is now considered as an alternative to the “old” rod-like models. For nice summary of discussed models see the papers [Egawa et al. 2007; Kakitani et al. 2006; Balaban et al. 2005]. In fact, there have been no crystals of chlorosomes or aggregated BChls obtained so far. Thus, the chlorosome remains the last known light-harvesting complex for which no high-resolution structural information is available. One of the reasons is definitely the size and unusual organization of the chlorosome. Further investigation by theoretical modeling using powerful computer clusters in the near future can finally solve the inner structure of these unique antennae – chlorosomes.

A.2. WrbA FROM *ESCHERICHIA COLI*

A.2.1. Flavin is a Prosthetic Group in Flavoproteins

Flavin is a tricyclic heteronuclear organic ring based on pteridine whose biochemical source is the vitamin riboflavin. The flavin moiety is often attached with an adenosine diphosphate to form flavin adenine dinucleotide (FAD), and in other circumstances, is found as flavin mononucleotide (FMN), a phosphorylated form of riboflavin (Figure A-9).

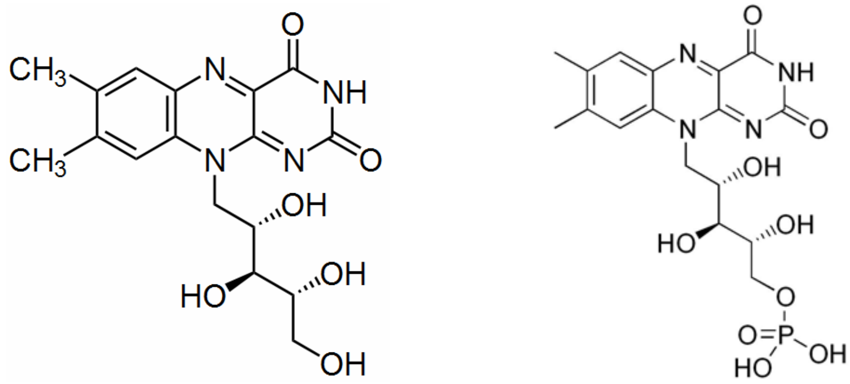

Figure A-9. Chemical structure of riboflavin (left) and flavin mononucleotide (FMN) (right).

It is in one or the other of these forms that flavin is present as a prosthetic group in flavoproteins. FMN is a prosthetic group found in NADH dehydrogenase, *E.coli* nitroreductase and old yellow enzyme. The flavin group is capable of undergoing oxidation-reduction reactions, and can accept either one electron in a two step process or can accept two electrons at once. In the form of $FADH_2$, it is one of the cofactors that can transfer electrons to the electron transfer chain.

A.2.2. WrbA from *Escherichia coli* and *Archaeoglobus fulgidus*

The tryptophan (W) repressor-binding protein (WrbA) from *Escherichia coli* (*E. coli* WrbA) was discovered in 1993, when it was copurified with the tryptophan repressor (TrpR) [Yang and Somerville 1993]. Biochemical characterization of *E.* coli WrbA showed that the protein binds one flavin mononucleotide (FMN) molecule per monomer and is multimeric in solution [Grandori et al. 1998]. These results, combined with sequence analysis and homology-based structural modeling, led to the suggestion that *E.* coli WrbA is the founding member of a new family of multimeric flavodoxin-like proteins. It was predicted that the WrbA family contains an αβ twisted open-sheet fold characteristic of flavodoxins and a conserved insertion after strand β4, forming an additional αβ unit [Grandori and Carey 1994]. The presence of this fold has recently been confirmed in the published crystal structures of the *Deinococcus radiodurans* and *Pseudomonas aeruginosa* WrbA homologues [Gorman and Shapiro 2005]. *E.* coli WrbA is the only purified and biochemically characterized WrbA protein in the literature. It was proposed that *E.* coli WrbA is an accessory element which blocks TrpR-specific transcriptional events that are deleterious to cells entering stationary phase. However, this assumption was later placed in doubt [Grandori et al. 1998]. Thus, the function of WrbA is unknown.

E. coli WrbA is upregulated in the early stages of the stationary phase, indicating that it could play a role in preparing the cell for long-term maintenance under stress conditions such as acids, salts, H_2O_2, diauxie and under affected electron transfer chains or in highly oxidizing environment [Chang et al. 2002; Cheung et al. 2003; Phadtare et al. 2002; Pomposiello et al. 2001; Tucker et al. 2002]. The most comprehensive sequence analysis of *E. coli* WrbA was reported in 1994 by Grandori and Carey [Grandori and Carey 1994]. Since that time, genomic sequencing has identified more than 100 genes annotated as encoding WrbA from metabolically and phylogenetically diverse prokaryotes spanning the *Bacteria* and *Archaea* domains. However, *E. coli* WrbA is the only WrbA that has been biochemically characterized. Recently, it was shown that several biochemically characterized NAD(P)H:quinine oxidoreductases (NQORs) from the *Fungi* and *Viridiplantae* kingdoms have significant sequence identity to WrbA and belong to the same family [Patridge and Ferry 2006]. It was demonstrated that *E. coli* WrbA and *A. fulgidus* WrbA exhibit robust NQO activity, such as reduction of quinones to the hydroquinone state to prevent interaction of the semiquinone with O_2 and production of superoxide. Although quinones usually serve as electron mediators by cycling between the oxidized (hydroquinone) state and the two-electron reduced (hydroquinol) state, quinones can also participate in deleterious redox cycling through direct interactions with single electron acceptors such as O_2, which leads to the accumulation of reactive oxygen species such as superoxide, hydrogen peroxide, and the hydroxyl radical [Adams and Jia. 2005; Cervantes et al. 2002; Finneran et al. 2002, Jaiswal 2000; Jensen et al. 2002; Wrobel 2002; Patridge and Ferry 2006] and references therein. These results were consistent with a role for WrbA in the oxidative stress response of diverse prokaryotes from the *Bacteria* and *Archaea* domains. Although the idea is speculative, *E. coli* WrbA could function in cell signaling by reducing the quinone pool, which would subsequently signal redox sensors such as the ArcA modulon [Patridge and Ferry 2006].

A.2.3. New Insights into *E. coli* WrbA Function

Structure of *E. coli* WrbA bridges bacterial flavodoxins and eukaryotic NAD(P)H: quinone oxidoreductases [Carey et al. 2007]. In NQORs both oxidized and reduced substrates, NADH and NADPH are accepted unspecifically equally, and also a wide range of quinones and other electrophiles. WrbA activity shares these features, but unlike the NQORs, which use FAD as their redox cofactor, WrbA activity is FMN-dependent. WrbA is tetrameric (confirmed by recent 0.26 nm crystal structure of oxidized *E. coli* WrbA (Figure A-10) [Carey et al. 2007]), but unlike multimeric flavodoxins it does not present recognizable domains known to function in subunit assembly.

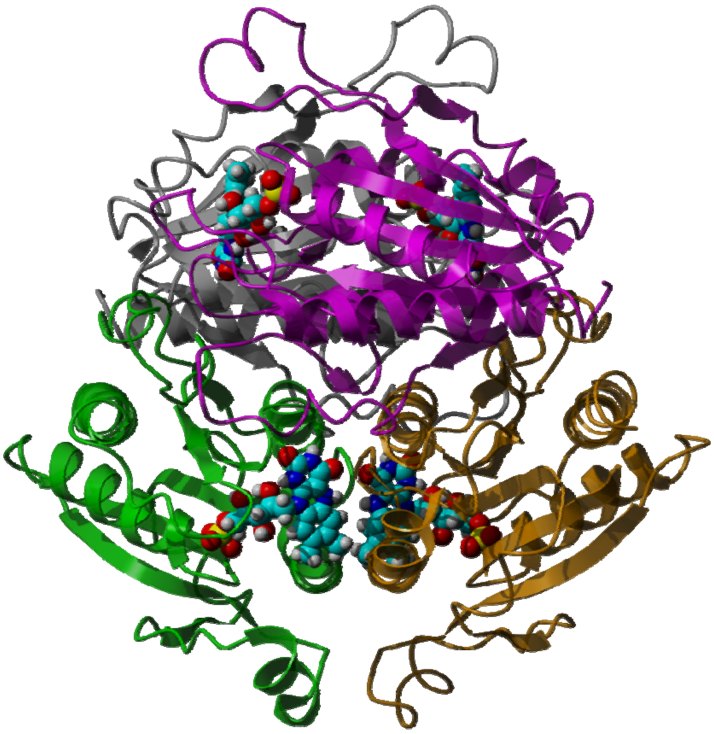

Figure A-10. 0.26 nm crystal structure of *E. coli* WrbA. Ribbon representation of tetramer WrbA (chain A green, chain C orange, chain A' magenta and chain C' gray) FMN in space filling representation (carbon cyan, nitrogen blue, oxygen red and phosphor yellow. FMN is shown as double-reduced form. The original crystal structure of 0.26 nm oxidized *E. coli* WrbA [Carey et al. 2007] was solvated and equilibrated by short geometry optimization in YASARA. Rendered by Pov-Ray.

It was proposed that, the dimer-tetramer equilibrium is stabilized by FMN. Direct comparison of *E. coli* WrbA crystal structure and FAD-dependent rat liver NQO1 (PDB ID 1QRD; [Li et al. 1995]) crystal structure (assigned to be the closest relative of *E.* coli WrbA) revealed important features of cofactor specificity.

B. METHODS

B.1. CLASSICAL MECHANICS – INTRODUCTION TO MOLECULAR DYNAMICS

Why we use molecular dynamics, if quantum mechanics works perfect? To answer this, we shall understand the main principles and differences between these two fundamental approaches. It is obvious, that describing detailed structure of matter at the atomic level is still more and more necessary. If we describe electronic structure of any system by using quantum mechanics, we can in principle also describe all possible interactions in the system. In practice, however, only system counting tens to hundreds of atoms can be treated that way, even when various numerical methods and approximations are used.

Fortunately, only few processes require any quantum mechanical approach, and many of the bio-processes such as protein folding, conformational changes and many other are classical. Of course we cannot describe the detailed processes of bond breaking or formation without it. In fact, it will often prove a much better alternative regardless of the computational cost, since the models are parameterized to reproduce real experimental observations rather than simplified theories. The straightforward and relatively simple way how to treat large biologically relevant systems *in silico*, is thus classical mechanics and molecular dynamics in particular.

B.1.1. Molecular Dynamics – Newton’s laws of motion

Molecular dynamics simulations calculate future positions and velocities of atoms, based on their current positions and velocities [van Gunsteren and Berendsen 1990; Karplus and Petsko 1990]. A simulation first determines the force on each atom F_i as a function of time, equal to the negative gradient of the potential energy

$$\vec{F}_i = -\frac{\partial V}{\partial \vec{r}_i},$$

where V is the potential energy function and $\vec{r}_i$ is a position of atom i. The acceleration $\vec{a}_i$ of each atom is determined by division of the force acting on it by the mass of the atom

$$\vec{a}_i = \frac{\vec{F}_i}{m_i}.$$

The change in velocities $\vec{v}_i$ is equal to the integral of acceleration over time. The change in the position $\vec{r}_i$ is equal to the integral of velocity over time. Kinetic energy E_{kin} is defined in terms of the velocities of the atoms

$$E_{kin} = \frac{1}{2}\sum_{i=1}^{N} m_i \vec{v}_i^2 .$$

The total energy of the system, called the Hamiltonian, is the sum of the kinetic and potential energies

$$H(r,p) = E_{kin}(p) + V(r),$$

where r is the set of Cartesian coordinates and p is the momenta of the atoms.

B.1.2. Force Field

B.1.2.1. General Introductory Remarks

The most crucial task during last decade was (and in some cases still is) to find the form and calculate the potential energy $V(r)$. There are two main criteria that have to be considered, the precision and agreement with experiment, and on the other hand the level of complexity and required computational time. The form of potential energy term which we are using today is a compromise of these two demands. Its final appearance, together with the actual interaction parameters used in the simulation, is called the force field (FF). There are many of different force fields widely spread and used by various research groups [Van Gunsteren et al. 1998; Cornell and Kollman et al. 1995; Jorgensen 1998; Karplus and Brooks et al. 1983], but most of them are closely related. A potential that provides extremely high accuracy in all situations would be very demanding for any computer cluster, so when applying it to a molecular level several approximations are made.

B.1.2.2. Force Field Parameters

As mentioned above, the classical mechanics describes molecule as a collection of atoms that interact with each other by simple analytical functions. This description is called a force field. One component of a force field is the energy arising from compression and stretching a bond.

This component is often approximated as a harmonic oscillator and can be calculated using Hooke's law

$$V_{Spring} = \frac{1}{2} K_r (r - r_0)^2 .$$

The bonding between two atoms is analogous to a spring connecting two masses. Using this analogy the equation above gives the potential energy of the system of masses, V_{Spring}, and the force constant of the spring, K_r. The equilibrium and displaced distances of the atoms in a bond are r_0 and r. Both K_r and r_0 are constants for a specific pair of atoms connected by a certain spring. K_r and r_0 are force field parameters.

The potential energy of a molecular system in a force field is the sum of individual components of the potential. The energies of the individual bonding components (bonds, angles, and dihedrals) are functions of the deviation of a molecule from a hypothetical compound that has bonded interactions at minimum values

$$E_{Total} = term_1 + term_2 + \cdots + term_n .$$

Further, the mathematical functions used to describe individual components of the potential are discussed, and also the circumstances under which the functions become poor approximations.

B.1.2.3. Force Field Components – Terms of the Potential

Bonded Interactions – Bonds, Angles and Dihedrals

The harmonic functions are commonly used to calculate potentials for bonds and bond angles:

$$V_{Bond}(r_{ij}) = \frac{k_{ij}^b}{2} \left(r_{ij} - r_{ij}^0\right)^2 , V_{Angle}(\vartheta_{ijk}) = \frac{k_{ijk}^{\vartheta}}{2} \left(\vartheta_{ijk} - \vartheta_{ijk}^0\right)^2 ,$$

where k_{ij}^b and k_{ijk}^{ϑ} are the force constants and r_{ij}^0 and $r_{ij} / \vartheta_{ijk}^0$ and ϑ_{ijk} are the equilibrium and displaced distances/angles of the atoms in a bond/angle, respectively.

However, a Morse function best approximates a bond potential. One of the obvious differences between the Morse and harmonic potential is that only the Morse potential can describe a dissociating bond (Figure B-1).

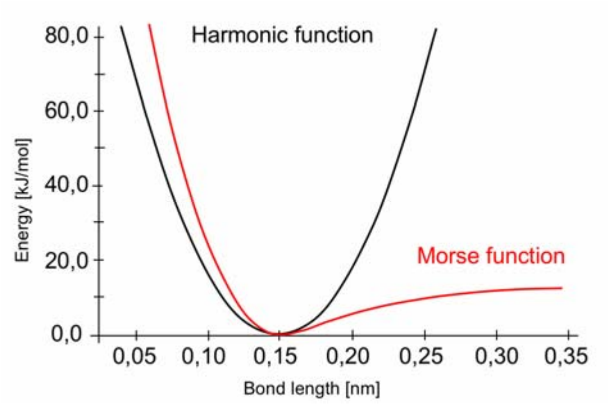

Figure B-1. Comparison of harmonic (black line) and Morse (red line) function shapes.

The Morse function rises more steeply than the harmonic potential at short bonding distances. This difference can be important especially during molecular dynamics simulations, where thermal energy takes a molecule away from a potential minimum. In light of the differences between a Morse and a harmonic potential, why do force fields use the harmonic potential? First, the harmonic potential is faster to compute and easier to parameterize than the Morse function. The two functions are similar at the potential minimum, so they provide similar values for equilibrium structures. As computer resources expand and as simulations of thermal motion become more popular, the Morse function may be used more often.

Dihedrals

In molecular mechanics, the dihedral potential function is often implemented as a truncated Fourier series. This periodic function is appropriate for the dihedral (torsional) potential

$$V_{Dihedral}(\varphi_{ijkl}) = k_{jk}^{\varphi}[1+\cos(n\varphi-\varphi_0)].$$

In this representative dihedral potential, k_{jk}^{φ} is the dihedral force constant, n is the periodicity of the Fourier term, φ_0 is the phase angle, and φ is the dihedral angle.

Example: An example below illustrates an HN–C(O) amide torsion taken from the AMBER FF. The Fourier component with a periodicity of one (n = 1) also has a phase shift of 0 degrees. This component shows a maximum at a dihedral angle of 0 degrees and minima at both –180 and 180 degrees. The potential uses another Fourier component with a periodicity of two (n = 2) (Figure B-2).

The relative sizes of the potential barriers indicate that the V_2 force constant is larger than the V_1 constant. The phase shift is 180 degrees for the Fourier component with a two-fold barrier.

Minima occur at –180, 0, and 180 degrees and maxima at –90 and 90 degrees. Adding the two Fourier terms results in potential with minima at –180, 0, and 180 degrees and maxima at –90 and 90 degrees.

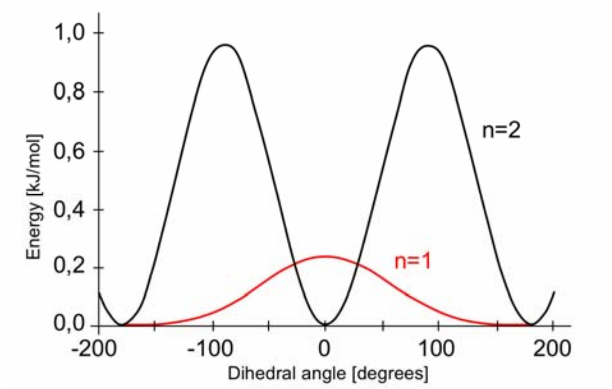

Figure B-2. Two Fourier terms of HN–C(O) amide dihedral potential taken from the AMBER FF.

Non-bonded Interactions

All bonded interactions have a great advantage over the non-bonded interactions, which arise from their local character in space, and the fact that their number will only increase linearly with system size, meaning they are not very costly to calculate. In contrast, there are a lot more of non-bonded interactions between atoms separated by more than three bonds or even located in different molecules. The calculation of these forces is the most demanding and time-consuming part of any molecular dynamics simulation, accounting for roughly 90% of the total processor usage. These non-bonded interactions are usually described with a repulsive term important on short distances (overlap of wave functions, or hard sphere repulsion term), always present attractive dispersion (London) forces, and electrostatic interactions between charged particles. The dispersive and repulsive components are often described by Lennard-Jones potential

$$V_{6-12}(r_{ij}) = \frac{C_{ij}^{(12)}}{r_{ij}^{12}} - \frac{C_{ij}^{(6)}}{r_{ij}^{6}},$$

where $C_{ij}^{(6)}$ and $C_{ij}^{(12)}$ are parameters that depend on the type of atoms involved, determining the amount of attraction and repulsion respectively. The resulting potential is weakly attractive at large distances but strongly repulsive when the atoms start to overlap.

The potential term of electrostatic interaction between two charged atoms has an appearance

$$V_{Coulomb}(r_{ij}) = \frac{q_i q_j e^2}{4\pi\varepsilon_0\varepsilon_r r_{ij}},$$

where q_i and q_j are the atomic charges. The permittivity of vacuum is designated as ε_0 and ε_r is the relative permittivity. The value of relative permittivity should be higher than unity, but in many force fields this is instead corrected implicitly by parameterizing the charges to yield correct equilibrium properties. As an alternative, a permittivity $\varepsilon_r = 2$ is sometimes used to account for the electronic polarization. However, the exact value of ε_r on atomic level is due to its macroscopic character not easy to represent.

B.1.3. Truncation of Non-bonded Interactions – Non-bonded Cutoff

Before a brief concept of cutoff methods is given, the list of all non-bonded interactions and their decay functions shall be presented in advance:

charge – charge	1/r
charge – dipole	$1/r^2$
dipole – dipole	$1/r^3$
dipole – quadrupole	$1/r^4$
charge – induced dipole	$1/r^4$
dipole – induced dipole	$1/r^6$
Lennard – Jones	$1/r^6$

Force field calculations often truncate the non-bonded potential energy of a molecular system at some finite distance. Truncation (non-bonded cutoff) saves computing resources. Also, periodic boxes and boundary conditions require it. However, this approximation is too crude for some calculations. For example, a molecular dynamic simulation with an abruptly truncated potential produces anomalous and nonphysical behavior. One symptom is that the solute (for example, a protein) cools and the solvent (water) heats rapidly. The temperatures of system components then slowly converge until the system appears to be in equilibrium, but it is not. A relatively simple method how to moderate the consequences of the nonphysical behaviors caused by applying a non-bonded cutoff is to use a potential switching function. The mathematical formulas are given according value of r_{ij} and have an appearance

a) $r_{ij} \le r_{ON}$ and $E' = E \ge 1$

b) $r_{ON} \le r_{ij} \le r_{OFF}$ and $E' = E\dfrac{(r_{OFF} - r_{ij})^2 (r_{OFF} + 2r_{ij} - 3r_{ON})}{(r_{OFF} - r_{ON})^3}$

c) $r_{ij} \ge r_{OFF}$ and $E' = E \ge 0$

These functions allow the non-bonded potential energy to turn off smoothly and systematically, removing artifacts caused by a truncated potential. With an appropriate switching function, the potential function is unaffected except in the region of the switch.

Different approach how to treat non-bonded terms of potential function is to apply a shifting potential

$$E' = E\left(1 - \frac{2r_{ij}^2}{r_{OFF}^2} + \frac{r_{ij}^4}{r_{OFF}^4}\right).$$

In an attempt to remedy truncation problems, a shifting potential multiplies the non-bonded electrostatic potential by a function that goes to zero. That is, the potential is shifted to zero at the cutoff r_{OFF}. Unlike the switching function, the shifted potential does not apply to van der Waals interactions.

Particle Mesh Ewald summation

The last but not least approach how to treat interaction energies of periodic systems, particularly electrostatic energies, is to use Particle-Mesh-Ewald (PME) method. The basic principles of the method can be relatively briefly introduced by presenting an example of Coulomb forces with N particles. The electrostatic potential for a system of N charged (atomic charges q_i) particles embedded in a simulation cell of length L and periodic boundary conditions has an appearance

$$V = \frac{1}{2}\sum_{i,j=1}^{N} \sum_{n \in Z^3}^{'} \frac{q_i q_j}{\left|\vec{r}_{ij} + nL\right|},$$

where $\vec{r}_{ij}$ is a vector connecting particle *i* and *j*, n is an integer number of considered images of simulation cell. Clearly, the straightforward summation is very impracticable (Figure B-3; left). Two principal tricks are applied in order to decrease the computational costs.

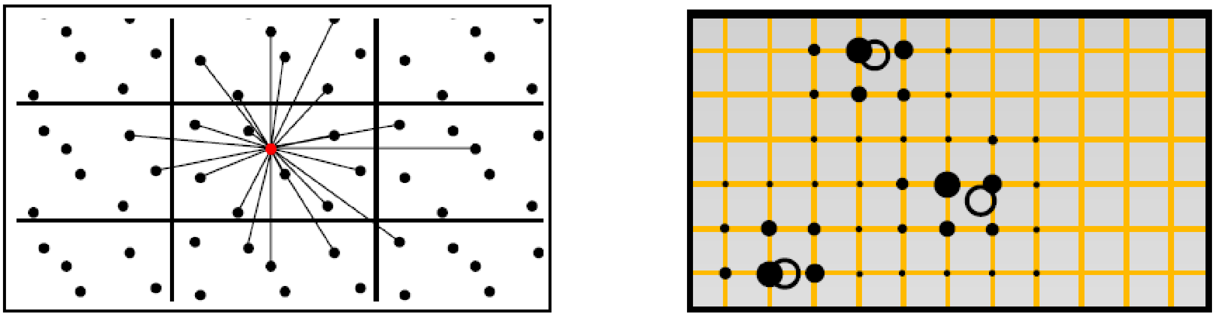

Figure B-3. Schematic representation of periodic simulation cell containing N charged particles, electrostatic interactions between central red particle and surrounding particles are shown (left). Schematic representation of spreading of three point charges onto neighboring grid points defined by PME method (right).

First trick is to decompose the interaction potential into a short-range component summed in real space and a long-range component summed in Fourier space

$$\frac{1}{r}=\frac{f(r)}{r}+\frac{1-f(r)}{r},$$

where the first term states for short-range and the second term for long-range interactions, respectively. Electrostatic potential has a form

$$V=V_{dir}+V_{rec},$$

where the first term describes direct space and the second term Fourier space. The advantage of this approach is the rapid convergence of the Fourier space summation compared to its real space equivalent when the real space interactions are long-range. The second trick is to discretize charges, and to use discrete Fourier transformation (FT). Each charge is spread on 64 = 4x4x4 neighboring grid points, e.g. grid spacing 0.12 nm (Figure B-3; right). Mesh-based charge density is obtained as an approximation to Σ of charges at atom positions. The evaluation of Coulomb forces $\vec{F}_{i,dir}$ is straightforward for short range interactions using Coulomb equation. For long range PME Coulomb forces $\vec{F}_{i,rec}$ three steps are needed.

a) Put charges on grid (Figure B-3; right)

b) FFT charge grid → convolution → FFT back, yields potential V_{rec} at grid points

c) Interpolate grid to derive forces at atom positions $\vec{F}_{i,rec}=-\frac{\partial}{\partial\vec{r}_i}V$

The Ewald summation was developed by Paul Peter Ewald in 1921 [Ewald 1921] to determine the electrostatic energy of ionic crystals as a method of theoretical physics, long before the advent of computers. The scaling of PME method gives $N * \log N$, where N is the number of atoms in the system. For details on PME method see the paper [Darden et al. 1999].

B.1.4. Integration Algorithms

If the atomic positions at a particular time t are $\vec{r}_i(t)$, the velocities $\vec{v}_i(t)$ are the first derivative of the positions with respect to time:

$$\vec{v}_i(t) = \frac{d}{dt}\vec{r}_i(t).$$

B.1.4.1. Leap frog Algorithm

One of the well established integration algorithms is the leap frog algorithm. This algorithm updates the positions of atoms and the velocities for the next time step by this calculation

$$\vec{v}_i\left(t + \frac{1}{2}\Delta t\right) = \vec{v}_i\left(t - \frac{1}{2}\Delta t\right) + \Delta t \vec{a}_i(t).$$

In the first time step (Δt), the velocities advance from time $t = 0$ to $t + 1/2\Delta t$. In doing so, they “leap” over the positions at time t. The current velocities are then calculated using equation

$$\vec{v}_i(t) = \frac{1}{2}\left[\vec{v}_i\left(t + \frac{1}{2}\Delta t\right) + \vec{v}_i\left(t - \frac{1}{2}\Delta t\right).\right]$$

This equation supplies only approximate velocities used to calculate energies at time t. The acceleration is determined and the cycle renewed. In the subsequent steps, the velocities advance from $t - 1/2\Delta t$ to $t + 1/2\Delta t$. The resulting set of positions and velocities is the molecular dynamics trajectory.

During a molecular dynamics simulation, the current positions $\vec{r}_i(t)$ and the mid-step velocities $\vec{v}_i(t - 1/2\Delta t)$ are stored. Since the algorithm provides mid-step velocities, but not velocities $\vec{v}_i(t)$ for the positions at time t, the value of $E_{Total}(t)$ can only be approximated. This results in slightly larger fluctuations in $E_{Total}(t)$ than an algorithm that calculates exact values of $\vec{v}_i(t)$.

B.1.4.2. Verlet Algorithm

The Verlet integrator offers greater stability than the much simpler Euler integration methods, as well as other properties that are important in physical systems such as time-reversibility and area preserving properties. Stability of the technique depends fairly heavily upon either a uniform update rate, or the ability to accurately identify positions at a small time delta into the past. The method was developed by French physicist Loup Verlet in 1967.

Mathematical form

At first it may seem natural to simply calculate trajectories using Euler integration, which is defined by

$$x(t_0+\Delta t)=x(t_0)+v(t_0)\Delta t\,, \qquad v(t_0+\Delta t)=v(t_0)+a(t_0)\Delta t,$$

where t_0 is the current time and Δt is the time step. However, this kind of integration suffers from many problems. The Verlet algorithm reduces the level of errors introduced into the integration by calculating the position at the next time step from the positions at the previous and current time steps, without using the velocity.

$$x(t_0+\Delta t)=x(t_0)+\left(x(t_0)-x(t_0-\Delta t)\right)+a\Delta t^2 = 2x(t_0)-x(t_0-\Delta t)+a\Delta t^2$$

The velocity at each time step is then not calculated until the next time step.

$$v(t_0)=\frac{x(t_0+\Delta t)-x(t_0-\Delta t)}{2\Delta t}$$

This can create technical challenges in molecular dynamics simulations, because kinetic energy and instantaneous temperatures at time t_0 cannot be calculated for a system until the positions are known at time $t_0+\Delta t$.

Derivation

The Verlet integrator can be derived from the Taylor expansion of a molecular dynamics trajectory. Let $x(t)$ be the trajectory of a particle at time t. The Taylor expansion around time t_0 then gives

$$x(t_0+\Delta t)=x(t_0)+\Delta t x'(t_0)+\frac{1}{2}\Delta t^2 x''(t_0)+\frac{1}{6}\Delta t^3 x'''(t_0)+O\left(\Delta t^4\right)$$

and

$$x(t_0 - \Delta t) = x(t_0) - \Delta t x'(t_0) + \frac{1}{2}\Delta t^2 x''(t_0) - \frac{1}{6}\Delta t^3 x'''(t_0) + O(\Delta t^4)$$

Adding these together gives

$$x(t_0 + \Delta t) + x(t_0 - \Delta t) = 2x(t_0) + \Delta t^2 x''(t_0) + O(\Delta t^4)$$

Arranging into the more conventional format:

$$x(t_0 + \Delta t) = 2x(t_0) - x(t_0 - \Delta t) + \Delta t^2 x''(t_0) + O(\Delta t^4),$$

where the term $O(\Delta t^4)$ represents deviations in the fourth-order and higher terms in the Taylor expansion.

This offers the clear advantage that the third-order term from the Taylor expansion cancels out, thus making the Verlet integrator an order more accurate than integration by simple Taylor expansion alone.

Furthermore, by subtracting the two original Taylors series, we obtain the velocity as

$$v(t_0) = \frac{x(t_0 + \Delta t) - x(t_0 - \Delta t)}{2\Delta t} + O(\Delta t^2).$$

The velocity calculation is thus two orders less accurate than the trajectory calculation. However, this error does not accumulate because the velocity is recalculated from the more accurate trajectories at every timestep.

B.1.5. Temperature and Pressure Control

B.1.5.1. Common Ensembles

The objects studied by molecular dynamics behave according laws of statistical mechanics and thermodynamics. In principle, we may say that molecular dynamics provides information about movement of the studied system on the potential energy surface. In view of statistical physics this means that equilibrium molecular dynamics corresponds to the microcanonical ensemble. Four commonly used ensembles are as follows

a) Microcanonical – N, V, E constant quantity; Maximum entropy in equilibrium

b) Canonical – N, V, T constant quantity; Minimum Helmholtz energy in equilibrium

c) Canonical – N, P, T constant quantity; Minimum Gibbs energy in equilibrium

d) Grand canonical - μ, V, T constant quantity; Maximum P * V in equilibrium

However, for the description of most studied systems the picture of the canonical ensemble is needed. The difference between these ensembles is that microcanonical ensemble describes system with constant energy and this ensemble is the direct result of propagating Newtonian equations of motion. The canonical ensemble describes systems with constant temperature and volume or pressure. The problem is that these ensembles are not a solution of the classical equations of motion. There are several techniques that modify molecular dynamics simulation so that systems with constant temperature and pressure can be simulated. The simplest methods use direct resetting of the controlled quantity.

B.1.5.2. Temperature Definition

Most of the macroscopic quantities observed in experiments can not be attributed to the individual atoms, but they are collective properties of a very large number of atoms, for instance temperature and pressure. It is important to be able to control these in a simulation. If we start with a protein and water in a box it should proceed at about 300 K and normal pressure, not 1000 K or thermonuclear pressures, which would cause the biomolecule to fall apart. The temperature T of a system is directly related to the average kinetic energy of the atoms and the number of degrees of freedom N_f. We define a momentary microscopic temperature T as

$$\mathrm{T}(t) = \frac{1}{N_f k_B} \sum_{i=1}^{N} m_i \vec{v}_i(t) \cdot \vec{v}_i(t),$$

where k_B is Boltzmann’s constant. The effective system temperature is an equilibrium average $T = \langle \mathrm{T} \rangle$ of this entity over a sufficiently long time interval. The initial temperature of the system can thus be set by assigning random velocities with a gaussian distribution of the correct width to the atoms. Ideally, that temperature would be maintained through the simulation, but due to e.g. round-off errors in the integration algorithm and the use of force truncation the temperature needs to be controlled when performing longer simulations. This can be accomplished by rescaling the atom velocities every time step with a calculated factor λ (described below).

B.1.5.3. Temperature Control

In a molecular dynamics calculation, you can add a term to adjust the velocities, keeping the molecular system near a desired temperature [Berendsen et al. 1984]. During a constant temperature simulation, velocities are scaled at each time step. This couples the system to a simulated reservoir at T_0, with a temperature relaxation time of τ. The velocities are scaled by a factor λ, where

$$\lambda = \left[1 + \frac{\Delta t}{\tau} \left(\frac{T_0}{T} - 1 \right) \right]^{1/2} .$$

If the coupling parameter (the Bath relaxation constant) τ is too "tight" (<0.1 ps), an isokinetic energy ensemble results rather than an isothermal (microcanonical) ensemble. The trajectory is then neither canonical nor microcanonical. One cannot calculate true time-dependent properties or ensemble averages for this trajectory. It is possible to use small values of τ for these simulations:

a) to obtain a minimum energy structure at 0 K

b) to reach equilibrium temperature quickly before starting the equilibration phase of a simulation.

If the Bath relaxation constant τ is greater than 0.1 ps, the dynamic properties, like time correlation functions and diffusion constants should be calculable. However, it should be kept in mind, this method of temperature regulation does not give all properties of the canonical ensemble. In particular, it is not possible to calculate heat capacity C_V at constant volume.

B.1.5.4. Pressure Control

The exact derivation of mathematical formulas describing pressure control is beyond the scope of the theoretical introduction of this thesis. Therefore, we put here final equation without further explanation. The resulting pressure can be controlled through a coupling method very similar to the temperature, by scaling the coordinates of all particles and the box size every time step with a factor μ in a form

$$\mu = \sqrt[3]{1 + \frac{\Delta t}{\tau_p} \beta (\mathrm{P} - P_0)}.$$

For any reasonable value of the system compressibility β, this will produce exponential pressure relaxation, similar to the weak temperature coupling.

B.1.6. Periodic Boundary conditions – periodic box

Absolute majority of the molecular dynamics simulations use periodic conditions for their simulation cell in order to mimic endless size of the system and to minimize unfavorable edge effect at the solvent-vacuum boundary. Periodic boundary conditions place the molecular system in a periodic-box. Virtual identical images surround the initial box. The most commonly used shapes of the periodic box are cube, truncated octahedron, hexagonal prism and rhombic dodecahedron. The atoms farthest from the center of the original box no longer suffer from interactions with an edge, since the original box now meets an image of itself in all directions. The solute in the original box interacts only with its nearest neighbor solute images. Since the periodic images (black boxes; see picture below) are exact copies of the original box (blue box; see picture below), movements of atoms in the original box are duplicated in the images. When a particle leaves a box, its periodic image enters from the opposite box side and replaces it. This conserves the number of atoms in each box. Choose the non-bonded cutoff carefully when using periodic boundary conditions. The cutoff must be small enough to prevent an atom from interacting simultaneously with another atom and with that atom's virtual image.

Example: The example below shows the round particle in cell {B,B} with two possible non-bonded cutoffs. With the outer cutoff (black), the round particle interacts with both the rectangle and its periodic image. By reducing the non-bonded cutoff into the size of the inner circle (red), the round particle interact with only one {B,B} rectangle. For a rectangular box, the non-bonded cutoff should be less than one-half the smallest box dimension (Figure B-4).

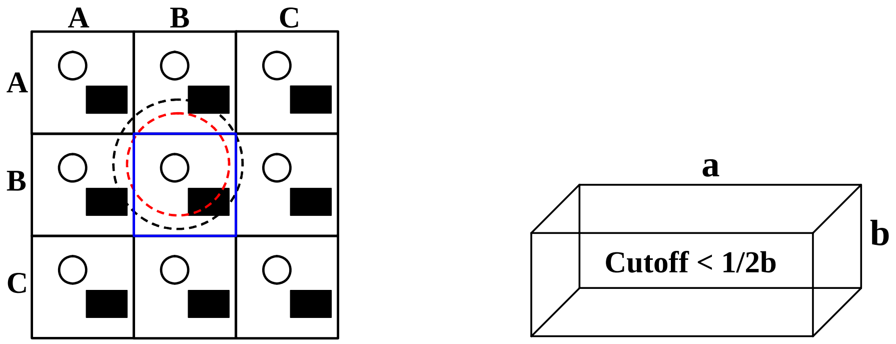

Figure B-4. Schematic representation of two non-bonded cutoffs (left) and their relation to box dimensions (right).

B.1.7. Analysis of Molecular Dynamics Trajectories

B.1.7.1. RMSD and RMSF

The root mean square deviation (RMSD) in bioinformatics usually measures the average distance between the backbones of superimposed proteins. In the study of conformational changes in a protein, one customarily measures the similarity in three-dimensional structure by the RMSD of the Cα atomic coordinates after optimal rigid body superposition. A widely used way to compare the structures of biomolecules is to translate and rotate (simply superpose) one structure with respect to the other to minimize the RMSD. The mathematical formula of RMSD has an appearance

$$RMSD = \sqrt{\frac{1}{N}\sum_{i=1}^{N}\Delta_i^2},$$

where Δ is the distance between N pairs of equivalent atoms (usually Cα carbons and sometimes C, N, O or Cβ). An RMSD value is expressed in length units. The most commonly used unit in structural biology is the Ångström (Å) which is equal to 10^{-10}m. Typically RMSD is used to make a quantitative comparison between the structure of a partially folded protein and the structure of the native state. For example, the CASP protein structure prediction competition uses RMSD as one of its assessments of how well a submitted structure matches the native state. Also some scientists who study protein folding simulations use RMSD as a reaction coordinate to quantify where the protein is between the folded state and the unfolded state.

The root mean square fluctuation (RMSF) is a measure of the deviation between the position of particle i and some reference position. The RMSF is defined as

$$RMSF = \sqrt{\frac{1}{T}\sum_{t_j=1}^{T}\left(x_i\left(t_j\right)-\tilde{x}_i\right)^2},$$

where T is the time over which one wants to average, and $\tilde{x}_i$ is the reference position of particle i. Typically this reference position will be the time-averaged position of the same particle i, ie. $\overline{x}_i$. Note that the difference between RMSD and RMSF is that with the later the average is taken over time, giving a value for each particle i, while with RMSD the average is taken over the particles, giving time specific values.

B.1.7.2. Hydrogen Bonds

In almost all relevant biological systems (protein enzymes, DNA, water, etc) there are hundreds to thousands of hydrogen bonds found. Their importance and variety is with no doubts immense. The detailed analysis of changes in number and quality of hydrogen bonds is one of the most common analysis (especially in theoretical studies using methods of molecular modeling). However, due to limited space of the theoretical part of this thesis, only few examples could be given here.

A hydrogen bond is a special type of attractive interaction (perhaps a variation of a dipole-dipole interaction) that exists between an electronegative atom and a hydrogen atom bonded to another electronegative atom. This type of bond always involves a hydrogen atom, thus the name. Hydrogen bonds can occur between molecules (intermolecularly; enzyme and substrate), or within different parts of a single molecule (intramolecularly; nucleic acids, proteins). The typical hydrogen bond is stronger than van der Waals forces, but weaker than covalent or ionic bonds. Intermolecular hydrogen bonding is responsible for the high boiling point of water (100 °C), while intramolecular hydrogen bonding is responsible for the secondary and partly tertiary structure of proteins and nucleic acids.

From the two electronegative atoms (usually fluorine, oxygen, or nitrogen) forming the hydrogen bond, the one with attached hydrogen atom is a hydrogen bond donor and the second a hydrogen bond acceptor. The hydrogen bond is often described as an electrostatic dipole-dipole interaction. However, it also has some features of covalent bonding: it is directional, relatively strong, produces interatomic distances shorter than sum of van der Waals radii, and usually involves a limited number of interaction partners, which can be interpreted as a kind of valence. These covalent features are more significant when acceptors bind hydrogens from more electronegative donors. Interatomic distances in the $X - H \cdots Y$ system: $X - H$ distance is typically ~ 0.11 nm, whereas $H \cdots Y$ distance is ~ 0.16 to 0.20 nm. Hydrogen bonds can vary in strength from very weak (1-2 kJ mol^{-1}) to extremely strong (40 kJ mol^{-1}), as in the ion HF_2^-. Typical values include: O—H...:N (29 kJ/mol), O—H...:O (21 kJ/mol), N—H...:N (13 kJ/mol), N—H...:O (8 kJ/mol) and HO—H...:OH_3^+ (18 kJ/mol). The length of hydrogen bonds depends on bond strength, temperature, and pressure. The bond strength itself is dependent on temperature, pressure, bond angle (criterion for the hydrogen bond existence is that its angle is smaller than 30 to 40 degrees), and environment (usually characterized by local dielectric constant). The typical length of a hydrogen bond in water is 0.197 nm. It is now commonly assumed that for hydrogen bonding the same effects (exchange, electrostatic, polarization, and dispersion) play a role as for "ordinary" intermolecular forces, with electrostatics plus Pauli (hard sphere) repulsion being dominant for hydrogen bonds.

B.1.8. Molecular Dynamics Limitations – approximations

Considering all advantages and effectiveness of molecular dynamics, one could think of this method as a very powerful and easy-to-use technique. However, as any other method, molecular dynamics has its limits which originate in used approximations and the power of computers in general. First, all interactions are treated purely by classical mechanics. Any chemical reaction, meaning bond break or form, electron transfer, change of partial atomic charge due to interaction with environment, events faster than integration time step of 1.0 fs cannot be followed by classic molecular dynamics. The size of the system, which can be evaluated by molecular dynamics simulations, is of many orders smaller than any other real system.

The accuracy of a simulation is entirely dependent on the accuracy of chosen force field, which always contains several approximations and uncertain parameters. It might seem a good idea to consistently start from quantum mechanics and derive detailed values for individual interaction parameters. Unfortunately, this neglects another important approximation, and that is that all forces are assumed to act between pairs of atoms. Of course one could include three and four particle interactions, but that would be extraordinary expensive. There is, however, one smarter alternative that works surprisingly well, the semi-empirical effective parameters that have been corrected to partially account for the higher order interactions while still being pair-additive. We still neglect all dynamic effects like polarizations in bonds, though.

To speed up the calculation of forces, the non-bonded interactions are further usually truncated beyond a distance of 1 – 2 nm. This is a fair approximation for Lennard-Jones interactions, but not always for electrostatics if there are free charges in the system.

The PME method, applicable to treat long-range electrostatic interactions, can be used more efficient for systems with "smooth" variations in density (due to the restriction of the density field to a mesh), or continuous potential functions. Localized systems or those with large fluctuations in density may be treated more efficiently with the fast multipole method of Greengard and Rokhlin.

Thus, the reliability and importance of molecular dynamics should always be understood by keeping all of these limits and approximations in mind.

B.2. GEOMETRY OPTIMIZATION

Geometry of any molecular system can be optimized (improved in the sense of its energy) by either molecular or quantum mechanical methods. More precisely, the optimized geometry holds the coordinates of a molecular structure that represent a potential energy minimum [Fletcher 1980; Gill et al. 1981]. For a potential energy V and coordinates $\vec{r}_i$ the optimized coordinates satisfy an equation

$$\frac{\partial V}{\partial \vec{r}_i} = 0.$$

A geometry optimization calculation might be performed by one of these goals in mind

a) Characterize a potential energy minimum. A geometry optimization results in a new structure at a minimum. The atomic coordinates and energy of this structure can be examined.

b) Obtain a new stable structure as a starting point for a single point, quantum mechanical calculation, which provides a large set of structural and electronic properties.

c) Prepare a molecule for a molecular dynamics simulation. If the forces on atoms are too large, the integration algorithm may fail during a molecular dynamics calculation.

B.2.1. Geometry Optimizers – algorithms

B.2.1.1. Steepest Descent

A steepest descent method is a first order minimizer (geometry optimizer). It uses the first derivative of the potential energy with respect to the Cartesian coordinates. The method moves down the steepest slope of the interatomic forces on the potential energy surface. The descent is accomplished by adding an increment to the coordinates in the direction of the negative gradient of the potential energy, or the force. The steepest descent method rapidly diminishes large forces on atoms. This is especially useful for eliminating the large non-bonded interactions often found in initial structures. Each step in a steepest descent requires minimal computing time. Its disadvantage is that convergence toward a minimum is very slow.

B.2.1.2. Conjugate Gradient

A conjugate gradient method differs from the steepest descent technique by using both the current gradient and the previous search direction to drive the minimization. A conjugate gradient method is a first order minimizer. The advantage of a conjugate gradient minimizer is that it uses the minimization history to calculate the search direction, and converges faster than the steepest descent technique. It also contains a scaling factor, b, for determining step size. This makes the step sizes optimal when compared to the steepest descent technique. There are two slightly different versions of the conjugate gradient method, Fletcher-Reeves and Polak-Ribiere, which is more refined.

B.2.1.3. Second Order Optimizers

From the long list of the second order optimizers, only two commonly used are briefly presented here. The Newton-Raphson block diagonal method calculates both the first and second derivatives of potential energy with respect to Cartesian coordinates. These derivatives provide information about both the slope and curvature of the potential energy surface. Unlike a full Newton-Raphson method, the block diagonal algorithm calculates the second derivative matrix for one atom at a time, avoiding the second derivatives with respect to two atoms. As is true for the conjugate gradient methods, this algorithm should not be used when the initial interatomic forces are very large (meaning, the molecular structure is far from a minimum). The second method, Eigenvector following, uses a diagonalized Hessian matrix to implicitly give the second derivatives of energy with respect to atomic displacements. The initial guess is computed empirically. This method is available for all semi-empirical methods except Extended Hückel, and for *ab initio* calculations. This algorithm may be used if the structure is far from a minimum.

B.3. QUANTUM CHEMISTRY

As the computational power of computer clusters rapidly increased during last decades, the computational chemistry and particularly quantum chemistry became effective tool for various theoretical studies on small systems. Detailed description of electronic structure provides valuable information, which often cannot be obtained by any experimental techniques. In the following chapter the basic principles and calculation methods of quantum chemistry will be addressed. As the content of this theoretical field is too large, only parts, which were applied in practical part of this thesis will be introduced.

Quantum chemistry is a part of theoretical chemistry, which applies quantum mechanics and quantum field theory to describe fundamental processes in chemistry. The description of the electronic properties of atoms and molecules is the main task of quantum chemistry.

Quantum chemistry mathematically describes the fundamental behavior of matter at the molecular scale. It is, in principle, possible to describe all chemical systems using this theory. In practice, only the simplest chemical systems may realistically be investigated in purely quantum mechanical terms, and approximations must be made for most practical purposes (e.g., Hartree-Fock, post Hartree-Fock or Density functional theory).

B.3.1. Historical Background

Since 1911 when English physicist Ernest Rutherford established first model of an atom, which was further improved by Danish physicist Niels Bohr in 1913, the energy was quantized. Completely new mechanics valid in micro-world was needed. In 1925 and 1926 German physicist Werner Heisenberg and Austrian physicist Erwin Schrödinger published fundamental principles of quantum theory.

Quantum chemistry [Szabo and Ostlund 1996] is an application of quantum mechanics. It describes system of electrons and point nuclei. The most of quantum-chemical calculations deals with non-relativistic stationary time-independent Schrödinger equation, which has the well-known appearance

$$H\Psi = E\Psi,$$

where E is energy, Ψ is wave function, and H is Hamilton operator or Hamiltonian.

B.3.2. Born-Oppenheimer approximation

Overall energy, or Hamiltonian function, of molecular system can be formally presented in the form

$$\hat{H}_t = \hat{H}_{en} + \hat{H}_{\text{int}} + \hat{H}_{ext},$$

where $\hat{H}_t$ is an operator of overall energy of the system, $\hat{H}_{en}$ is an operator of kinetic energy and mutual Coulomb interaction between system particles, $\hat{H}_{\mathrm{int}}$ is an operator of interaction between magnetic moments of system particles (spin-spin and spin-orbital interactions) and $\hat{H}_{ext}$ is an operator of environmental energetic contributions (e.g. external electric or magnetic field). In the most of practical situations and applications of quantum theory we can omit last two terms and write

$$\hat{H}_t = \hat{H}_{en} = \hat{T}_e + \hat{T}_n + \hat{V}_{ee} + \hat{V}_{en} + \hat{V}_{nn}.$$

The more terms in the overall Hamiltonian function the more difficult is to solve Schrödinger equation. One of the possible simplifications is based on the fact that nucleus mass is of three orders higher than that of electron. Due to the fact that mutual forces acting on atom nuclei and electrons in atoms and molecules are equal (equality of action and reaction forces), the resulting accelerations, mean velocities and mean kinetic energies of electrons are significantly bigger than corresponding quantities of atom nuclei. Thus, we can omit term for kinetic energy of nuclei and write simpler form of Hamiltonian function

$$\hat{H}_{en} = \hat{T}_e + \hat{V}_{ee} + \hat{V}_{en} + \hat{V}_{nn}.$$

This kind of approximation is known as Born-Oppenheimer approximation. We can further omit also $\hat{V}_{nn}$ term, because it gives constant value for given arrangement of the atom nuclei. Thus, in BO approximation overall system energy is calculated for given positions of all atom nuclei. The hypersurface of system energy, called Born-Oppenheimer Potential Energy Surface (BOPES), is obtained by considering all possible positions of atom nuclei.

B.3.3. Wave function – Slater Determinant

It is almost impossible to solve Schrödinger equation for the most of the systems due to reciprocally influenced movement of electrons. Therefore, we assume movement of each electron as an independent movement in the averaged electrostatic field formed by other electrons. Wave function describing n electrons has a form of antisymmetrical product of n one-particle functions of Slater determinant [Szabo and Ostlund 1996]. Each one-electron function is defined by three electron coordinates and spin value ± ½. When forming Slater determinant one needs to fulfill Pauli exclusion principle. If spin-orbitals are normalized the Slater determinant has a form

$$\Phi(x_1 \cdots x_N) = \frac{1}{\sqrt{N!}} \begin{vmatrix} \chi_1(x_1) & \cdots & \chi_N(x_1) \\ \vdots & \ddots & \vdots \\ \chi_1(x_N) & \cdots & \chi_N(x_N) \end{vmatrix}.$$

Exact solution of Schrödinger equation can be obtained by expansion into complete basis constructed from Slater determinants

$$|\Psi\rangle = \sum_{n=1}^{\infty} C_n |\Phi_n\rangle.$$

However, endless expansion is not mathematically and computationally suitable. The following sections provide brief information on how to approximate this endless development.

B.3.4. Molecular Orbital – MO-LCAO

Molecular orbitals Ψ_i are usually defined by linear combination of atomic orbitals Φ_μ localized on each atom [Szabo and Ostlund 1996], procedure termed as MO-LCAO. Molecular orbitals are expressed by finite sum (basis function) of relatively small number of one-electron functions, which in general do not have to be orthogonal

$$\Psi_i = \sum_{\mu} C_{i\mu} \Phi_\mu,$$

where Φ_μ are already simple analytical functions forming complete system. Experiences show, that the most suitable basis function is formed by atomic orbitals localized on atom nuclei, due to conserved atomic character of wave function near atom nucleus. Usage of these functions has an advantage in fast convergence of this sum.

B.3.5. Basis Functions

Atomic orbitals obtained by exact solution of Schrödinger equation for hydrogen atom can be directly used as basis functions, which behave correctly for r → 0 and r → ∞. However, the analytical form of these functions is too complicated for practical use. Atomic orbitals could be defined as a series of other known simpler analytic functions similar to hydrogen atom functions [Szabo and Ostlund 1996]. The more basis functions are used the more demanding but also more accurate are the calculations.

B.3.5.1. Slater and Gauss basis functions

Commonly used Slater (STO – Slater Type Orbital) basis function has an appearance

$$R(r) = (2\zeta)^{n+1/2} \frac{1}{\sqrt{(2n)!}} r^{n-1} e^{-\zeta r},$$

where ζ is Slater exponent, which values are normalized. However, in practice it is common to use Gauss (GTO – Gauss Type Orbital) basis functions in a form

$$R(r) = N r^n e^{-a(\vec{r}-\vec{r}_A)^2},$$

where N is normalization factor and $\vec{r}_A$ is an atom nucleus coordinate.

The advantage of Gauss basis functions is the fact, that product of two functions localized on A and B center is again Gauss function. This noticeably increases the speed of calculations, mostly on more centers integrals, which are simplified to one- or two-centers integrals. In spite of evident computational advantage, Gauss functions give good results only for distances not too close or not to far from atom nucleus. Therefore, it is common to use more functions for this type of basis function. One of possible approach is to combine Gauss basis function to approximate one Slater basis function. Basis set 6-31G describes inner atomic orbitals by combination of six Gauss basis functions and each of the outer orbitals by two functions.

B.3.5.2. Polarization and Diffusion functions

It is often not sufficient enough to use only occupied atomic orbitals to define particular basis functions. In order to increase precision of quantum-chemical calculations we need to consider two more types of functions, namely diffuse and polarization functions. Polarization functions are denoted by letters p, d and f, such as (p,d), exactly indicating which and how many functions are added to the basis set or by simpler notation by using an asterisk sign. Two asterisks, **, indicate that polarization functions are also added to light atoms (hydrogen and helium). These are auxiliary functions with one additional node. For example, the only basis function located on a hydrogen atom in a minimal basis set would be a function approximating the 1s atomic orbital. When polarization is added to this basis set, a p-function is also added to the basis set. This allows molecular orbitals involving the hydrogen atoms to be more asymmetric about the hydrogen nucleus. Representation of bonding between atoms is improved. Similarly, d-type functions can be added to a basis set with valence p orbitals, and f-functions to a basis set with d-type orbitals.

Next, the diffuse functions can be added to basis sets. Diffuse functions are very shallow Gaussian basis functions, which more accurately represent the "tail" portion of the atomic orbitals. Application of diffuse functions allows better description of weakly bond electrons, which are more distant from atom nucleus. In general, these functions are crucial for describing anions and excited states of atoms or molecules. The plus sign, +, is used as an abbreviation. Two plus signs indicate that diffuse functions are also added to light atoms (hydrogen and helium). As an example, the basis set 6-31+G* involves diffuse and polarization functions on all atoms except hydrogen atoms.

B.3.6. Quantum-chemical Calculation Methods – Hartree-Fock method

B.3.6.1. Historical Background

The first Hartree-Fock method was developed in 1920s, just after the Schrödinger equation was introduced in 1926. In 1927 D.R. Hartree introduced a procedure, which he called the Self Consistent Field (SCF) method, to calculate approximate wave functions and energies for atoms and ions. Hartree sought to do away with empirical parameters and solve the many-body time-independent Schrödinger equation from fundamental physical principles, i.e. *ab initio*. In 1928 J.C. Slater and J.A. Gaunt independently showed that Hartree's method could be treated by applying theoretical variational principle to an ansatz (trial wave function) as a product of single-particle functions.

In 1930 Slater and V.A. Fock independently pointed out that the Hartree method did not respect the principle of antisymmetry of the wave function. It was then shown that a Slater determinant, a determinant of one-particle orbitals first used by Heisenberg and Dirac in 1926, trivially satisfies the antisymmetric property of the solution and hence is a suitable ansatz for applying the variational principle. The original Hartree method can then be viewed as an approximation to the Hartree-Fock method by neglecting exchange. Fock's original method relied heavily on group theory and was too abstract for contemporary physicists to understand and implement. In 1935 Hartree reformulated the method more suitably for the purposes of calculation.

Ab initio methods

The term "*ab initio*" comes from Latin "from the beginning". The Schrödinger equation is solved without any experimental parameters. Theoretical background of *ab intio* methods were established by Slater (Slater determinant) in 1930. From the theoretical studies we point out crucial work published by Roothaan in 1950 and Pople in 1965. The software package for quantum chemical calculations Gaussian [Gaussian Inc] was firstly introduced by Pople in 1979.

B.3.6.2. Hartree-Fock equations

The term in Hamiltonian representing two-particle electrostatic interaction causes that differential equations for more electron systems can not be solved analytically. Simplification of Schrödinger equation in that case is decomposition of two-particle electrostatic interactions into effective terms describing particular electrons. The easiest anti-symmetrical wave function for N-electrons system in ground state is Slater determinant, which we described above.

Variational principle says, that the best wave function in this functional form is the one which minimizes the formula

$$E_0 = \left\langle \Psi_0 \middle| \hat{H} \middle| \Psi_0 \right\rangle,$$

where $\hat{H}$ is N-electrons system Hamiltonian. Variational parameters in the term for E_0 are spinorbitals χ_i. Minimization of the expression for E_0 gives us Hartree-Fock equations, that determine optimal spinorbitals in Slater determinant. Hartree-Fock equations have a form

$$f(i)\chi_i(x_i) = \varepsilon_i \chi_i(x_i),$$

where f_i is an effective one-electron operator, which can be expressed as

$$f(i) = -\frac{1}{2}\nabla^2 - \sum_{I=1}^{M}\frac{Z_I}{r_{iI}} + \nu^{HF}(i).$$

This operator is called Fock operator. The term $\nu^{HF}(i)$ represents mean value of potential acting on i-th electron due to other electrons. The basic principle of Hartree-Fock method is in approximation of complicated many-particles problem by one-particle problem (we do not consider electrostatic interactions between system particles explicitly, but only their mean average value). The Hartree-Fock potential $\nu^{HF}(i)$ (electrostatic field in which the i-th electron moves) depends on coordinates of other electrons. This fact gives Hartree-Fock equations non-linear character, which could only be solved by various iterations methods. The method used to solve Hartree-Fock equations is called Self-Consistent Field method (SCF). In practice, this method could be briefly described as follows: first we assume primary spinorbitals and calculate mean field v^{HF}. By having the mean field we can calculate new set of spinorbitals from Hartree-Fock equations. This is repeated until we reach the convergence criterion limit.

B.3.6.3. Hartree-Fock simplifications

a) Most of the typically, relativistic effects are completely neglected including spin-orbital interactions. The momentum operator is assumed to be completely non-relativistic.

b) Next, the electrons are moving in electrostatic field generated by static atom nuclei. (Born-Oppenheimer approximation described above).

c) The optimal solution is assumed to be a linear combination of a finite number of basis functions, which are orthogonal. The finite basis set is assumed to be approximately complete.

d) The wave functions are assumed to be describable by a single Slater determinant.

e) The mean field approximation is implied.

B.3.6.4. Hartree-Fock limits

The last simplification (outlined above) is the most important. Neglecting electron correlation can lead to large deviations from experimental results. Various post-Hartree-Fock methods, have been developed to include electron correlation to the multi-electron wave function. One of these approaches, Møller-Plesset perturbation theory, treats correlation as a perturbation of the Fock operator. Different approach is to expand the true multi-electron wave function in terms of a linear combination of Slater determinants, such as multi-configurational SCF, Configuration interaction, Quadratic configuration interaction and other.

An alternative to Hartree-Fock calculations is Density Functional Theory (DFT), which includes exchange and correlation effect. Indeed, it is common to use hybrid functionals such as the popular B3LYP, in which the exchange energy, in this case from Becke's exchange functional, is combined with the exact energy from Hartree-Fock theory.

B.3.7. Semiempirical Methods

Quantum mechanical methods incorporate various mathematical approximations. In general, we can discuss so called *ab intio* methods, by which Schrödinger equation is directly solved and semiempirical methods which will be briefly introduced.

Semiempirical methods use simplified form of exact Hamiltonian. Only electrons from valence sphere are considered in calculations. Empirical parameters used in calculations as input data are adapted in a sense of agreement of calculated data with experimental data. The main reason why semiempirical methods were developed was to decrease computational time and/or include more atoms in the calculations.

First theoretical models used only π-electrons, for example Hückel model in 1931, or PPP method of Pariser, Parr and Pople in 1951. In 1965 Pople created CNDO method, which considered all valence orbitals in calculations. Next, follows Pople’s method INDO with some improvements. The ZINDO method parameterized by Michael Zerner has already an option to calculate visible and UV spectra. In 1975 Michael Dewar introduces MINDO method, later modified and named as MNDO method. In 1985 Michael Dewar includes van der Waals interactions and terms for hydrogen bonds and the resulting method named AM1. Finally, in 1989 Stewart introduces PM3 methods as newly parameterized version of AM1. The reason why only valence electrons are being considered in these methods lies in an assumption, that electrons from inner layers only electrostatically shield the atom nucleus. It is necessary to keep in mind, that semiempirical methods contain set of parameters for individual atom elements and their application can be limited.

B.3.8. Density Functional Theory

The basic theorem of Density Functional Theory (DFT) states that every quantity characterizing the system can be expressed as a functional of electron density [Hohenberg and Kohn 1964]. Electron density is simpler mathematical object than wave function. It is real and measurable quantity depending only on three coordinates. In this theory energy is a function of electron density. The mean value of energy operator $\hat{f}$, which is formed by sum of one-electron spinless operators

$$\hat{f} = \sum_i f_i ,$$

can be expressed as

$$\begin{aligned}
&\int \hat{f}\left|\Psi(\vec{r}_1,\cdots,\vec{r}_N)\right|^2 d\tau = \left\langle \chi[\rho(\vec{r})]\right|\hat{f}\left|\chi[\rho(\vec{r})]\right\rangle = \\
&= \left\langle \chi[\rho(\vec{r})]\right|\hat{U}+\hat{T}+\hat{V}\left|\chi[\rho(\vec{r})]\right\rangle = \\
&= \left\langle \chi[\rho(\vec{r})]\right|\hat{U}+\hat{T}\left|\chi[\rho(\vec{r})]\right\rangle + \left\langle \chi[\rho(\vec{r})]\right|\hat{V}\left|\chi[\rho(\vec{r})]\right\rangle = \\
&= F[\rho(\vec{r})] + \int \chi*[\rho(\vec{r})]\hat{V}\chi[\rho(\vec{r})]d\vec{r} = \\
&= F[\rho(\vec{r})] + \int V\rho(\vec{r})d\vec{r}
\end{aligned}$$

where $\rho(\vec{r})$ are diagonal elements of density matrix of the first order, and $\hat{U}$,$\hat{T}$ and $\hat{V}$ are operators of potential energy, kinetic energy and external potential, respectively. Similarly, we can write for electron operator, which is defined as sum of two-electrons spinless operators

$$\hat{g} = \sum_{i<j} g_{ij},$$

$$\int \hat{g}\left|\Psi(\vec{r}_1,\cdots,\vec{r}_N)\right|^2 d\tau = \int g_{12}\rho(\vec{r}_1,\vec{r}_2)d\vec{r}_1 d\vec{r}_2,$$

where $\rho(\vec{r}_1,\vec{r}_2)$ are diagonal elements of density matrix of the second order. As Hamiltonian can be defined as a sum of one- and two-electrons operators, it is sufficient to know diagonal elements of both density matrixes in order to calculate energy. Such density matrixes have not been found till now. In practice, knowledge of one-electron densities is sufficient to obtain energy of a ground state. DFT method is very effective method applicable for electron structure calculations of more complex systems.

B.3.8.1. DFT functional

DFT functional should be expressed as a function of electron density or its derivative. We differentiate local (function of electron density) and non-local (function of derivative of electron density) DFT functional. The simplest functional is Local Spin Density Approximation LSDA and VWN (Vosko, Wilk, Nusair) correlation potential. Commonly used functional in computational chemistry is Becke3LYP (Becke, Lee, Yang, Parr) hybrid functional.

B.4. OPTICAL SPECTRA CALCULATIONS

B.4.1. Frenkel Electronic Hamiltonian

The optical spectra (absorption spectra) presented in *Results* section of this thesis were simulated by a molecular exciton matrix method [Bayley 1973]. One of the possible approaches is to apply an electronic Hamiltonian for the Frenkel exciton considering only the lowest excited state Qy into account [Pullerits 2000];

$$H = \sum_{i,j} (E + D_i + \Delta_i)\langle i|i\rangle + V_{ij}\langle i|j\rangle,$$

where E is an electronic transition energy of monomer of non-interacting chromophore i, D_i is the solvent shift (origin of spectral heterogeneity) and Δ_i is an origin of inhomogeneous broadening of the pigment i caused by stochastic fluctuations in the protein environment. To account for Δ_i as a random shift from average energy $E + D_i$, Gaussian distribution of transition energies represented by diagonal elements of Frenkel Hamiltonian is commonly used. Let us assume system of N interacting chromophores without charge separation, then the one-exciton Hamiltonian is given by the matrix containing N x N two-chromophore coupling energies. The main diagonal consists of the monomer transition energy of chromophores. The unperturbed site energies of the excited states can be adapted from the linear OD/LD/CD/FL spectra fit based on evolutionary algorithm [Raszewski et al. 2005].

B.4.2. Electrochromic Shifts

The Hamiltonian matrix for the system containing negatively charged (reduced in our case) chromophore can be constructed in the following way. In order to involve the presence of reduced form of the chromophore, electrochromic shifts in site energies [Raszewski et al. 2005; Krawczyk 1991] of the remaining chromophores have to be included. To compute electrochromic shifts interaction energy between atomic partial charges of reduced chromophore and difference dipole moments of the excited and ground states of other chromophores are calculated. In general, the negative charge of reduced chromophore affects transition energies of all other chromophores in the ground state. The electrochromic shift of transition energy ΔE can be calculated as the interaction energy between all atomic partial charges δq_i of reduced chromophore and the vector $\Delta\vec{\mu}$ of the chromophore in the ground state. The vector

$$\Delta\vec{\mu} = \vec{\mu}_e - \vec{\mu}_g,$$

is defined as a difference between permanent dipole moment of the excited and ground state. The magnitude of the vector is typically taken from the experiment (typical value for the molecule of chlorophyll is around 1 Debye). Mathematical equation describing electrochromic shift has an appearance

$$\Delta E = \frac{1}{4\pi\varepsilon_{eff}} \sum_i \delta q_i \Delta\vec{\mu} \frac{\vec{r}_i}{r_i^3},$$

where ε_{eff} is an effective dielectric constant (can not be obtained exactly only approximated) and $\vec{r}_i$ is a vector connecting the center of chromophore in the ground state and all atoms from reduced chromophore. For a further simplicity, the oscillator strength and exciton couplings of reduced chromophore can be neglected.

B.4.3. Transition Dipoles and Transition Monopoles Methods

For calculation of non-diagonal exciton coupling energies V_{ij} transition dipoles [Pearlstein 1991] and transition monopoles methods [Chang 1977] are commonly used. The dipole-dipole interaction energy V_{ij} (in cm^{-1}) between transition dipole moments of chromophore is defined by

$$V_{ij} = \frac{5.04}{\varepsilon}\left[\frac{\vec{\mu}_i \cdot \vec{\mu}_j}{r_{ij}^3} - \frac{3(\vec{r}_{ij} \cdot \vec{\mu}_i)(\vec{r}_{ij} \cdot \vec{\mu}_j)}{r_{ij}^5}\right],$$

where ε is dielectric constant, $\vec{\mu}_i$ is the transition dipole moment (in Debye) and $\vec{r}_{ij}$ is the vector connecting centers of i-th and j-th chromophore (in nm).

The interaction energy within transition monopole approximation [Sauer et al. 1996] is expressed by the sum of the Coulomb interactions of all transition monopoles. The non-diagonal interaction matrix elements are calculated as

$$V_{ila,jlb} = \sum_n \sum_m \frac{q_{inla} q_{jmlb}}{R_{in,jm}},$$

where q_{inla} is transition monopole n associated with the transition l → a on chromophore i, $R_{in,jm}$ is the distance between monopoles in and jm. The values of transition monopole charges for chromophores are calculated by quantum-chemical calculations [Chang 1977].

Eigenvalues and eigenvectors are obtained by diagonalization of Hamiltonian, represented by a matrix H_{ij}. The energies of the chromophore exciton states are given by the eigenvalues of Hamiltonian, whereas the components of the corresponding normalized eigenvectors specify the amplitude of each choromophore's contribution to each exciton state. Resulting steady-state optical spectra arising from these eigenvalues and eigenvectors are calculated as follows [Pearlstein 1991]. The intensity of a spectral band is proportional to the so-called dipole strength, which is a square of transition dipole moment. Dipole strengths of the particular exciton states k are defined as

$$\mu_k^2 = \sum_{i,j}^{n} \left(\vec{\mu}_i \cdot \vec{\mu}_j\right) U_{ik} U_{jk},$$

where U_{ik} and U_{jk} are corresponding eigenvectors. Position vectors $\vec{r}_{ij}$ and the orientation of the dipole moments $\vec{\mu}_i$ are crucial input data usually taken from well equilibrated systems. In the final step the calculated stick spectra are completed with Gaussian forms. Each of the envelopes has a certain FWHM (Full Width at Half Maximum), which roughly corresponds to the homogenous line-width of particular chromophore at specific temperature [Konermann and Holzwarth 1996]. Typically, a few thousands of calculated spectra are averaged to get statistically favorable optical spectrum, which could then be compared with equivalent spectrum obtained by wet experiments.

C. RESULTS AND DISCUSSION

Results from three purely theoretical projects concerning photosystem II (PSII), chlorosomes and flavoprotein WrbA are presented. In spite of differences in structure and function of these complexes, the same methodology was used in general. Results from all projects were divided into four parts namely, FF development, equilibrated molecular models preparation, MD simulations [Allen and Tildesley 1987] and analysis of MD trajectories.

C.1. PHOTOSYSTEM II REACTION CENTER

C.1.1. Force Field Development

Development of force field (FF) parameters for photosynthetic pigments (Figure A-4) involved in the crystal structure of photosystem II from *Thermosynechococcus elongatus* [Ferreira et al. 2004] represented substantial part of the computational work presented here. It is obvious that FF parameters play the crucial role as they provide exact mathematical description for all interactions between all atoms in the molecular systems. Presently, only limited types of molecules such as proteins, nucleic acids, lipids and, although limited, saccharides [MacKerell 2004] have such FF parameters developed. Thus, for all other molecules, all these FF parameters have to be obtained either from wet experiment or by various quantum-chemical calculations. The later approach was chosen also here. For majority of new FF parameters *ab initio* quantum-chemical HF/6-31G* calculations (self-consistent Hartree-Fock method where 6-31G* is a basis set of functions for description of molecular orbitals; [Roothan 1951]) in Gaussian software package [Frisch et al. 1998] were performed. However fast the computers are today, the development of appropriate FF parameters is still very demanding job and only limited number of compounds and molecules are being added each year to the original set of FF parameters such as AMBER FF [Cornell et al. 1995] or CHARMM FF [MacKerell et al. 1998]. Various calculations with different methods have been performed in order to obtain reliable collection of FF parameters for the photosynthetic cofactors of bacterial and higher plants [Kuczera et al. 1990; Folope et al. 1995; Ceccarelli et al. 2003; Tsai and Simpson 2003; Autenrieth et al 2004]. Here we present complete set of FF parameters for photosynthetic pigments such as chlorophyll *a* (Chl *a*), pheophytin *a* (Pheo *a*), plastoquinone 9 (PQ9), *β*-carotene (*β*-Car), heme and oxygen evolving complex (OEC). Part of the results was published earlier [Palencar et al. 2005]. Due to limited space, most of the new FF parameters and also FF parameters adopted from existing sets of AMBER-like FF parameters, originally developed for bacterial photosynthetic pigments [Ceccarelli et al. 2003], are not present in the thesis and are available in an electronic form. The author adopted all these new FF parameters directly to YASARA [Yasara Biosciences, *http://www.yasara.org/index.html*; Krieger et al. 2004] FF files, which are freely available at the joint of Institute of Physical Biology and Institute of Systems Biology and Ecology in Nove Hrady (CZ).

C.1.1.1. New Atom Types

First, new atom types had to be developed for structurally different parts of photosynthetic pigments from those found in bacterial equivalents. For structurally similar or identical parts original atom types developed for bacterial photosynthetic pigments [Ceccarelli et al. 2003] were preferentially used. Our aim was to implement all new and Ceccarelli's FF parameters into AMBER-like FF found in YASARA package, which was further used for equilibrated molecular models preparations and also for all MD simulations and analysis. The original Ceccarelli's atom types were up to 3 characters long, however, in YASARA only two letters are used. The list of all original and new atom types and their three and two letters codes is shown in the Table C-1. See detail description on all atom types in the paper [Ceccarelli et al. 2003].

No.		New atom type		New atom type		New atom type		New atom type
1.	hc	HC	cbb	C8	o2c	o1	OHT	ot
2.	ha0	HA	ccs	C$	c2e	C;	CCT	C?
3.	mgc	mg	cnb	C"	ct1	C4	O2T	ob
4.	nh	Nh	cpb	C%	ct2	C5	CH3	C-
5.	ns	ns	cqb	C&	ct3	C6	CH2	C:
6.	nmh	nm	crb	C9	cqo	C^	CA1	C0
7.	hn	hm	c2k	C+	cq2	C`	Mn	Mn
8.	cab	C7	c2a	C!	cqq	C~	O	OS
9.	csb	C#	o1c	of	HOT	ht	H1	hb

Table C-1. The list of new atom types assigned to the original [Ceccarelli et al. 2003] AMBER-like atom types. Note, that the first letter in the atom type name abbreviates corresponding chemical element (e.g. C for carbon, H for hydrogen, O for oxygen and N for nitrogen).

In the Table C-2 an equivalent atom types for Lennard-Jones (LJ) "12-6" potentials are given. On the basis of structural and chemical equivalence the existing LJ parameters such as van der Waals radius σ (in nm) and potential well depth ε (in kJ/mol) were assigned to new atom types. The values of the σ and ε, given in the second column of the table, are taken from the YASARA's AMBER FF file (amber99.fof).

Atom type	σ [nm] / ε [kJ/mol]	Equivalent atom types for Lennard-Jones “12-6” potentials (two letters codes adapted into YASARA format)
H	0.06 / 0.066	HS hm hb
HA	0.146 / 0.063	HZ
HO	0.0 / 0.0	HW LP ht
C	0.191 / 0.360	C* CA CB CC CN CM CK CQ CW CV CR CD CY CZ C" C# C$ C% C& C7 C8 C9 C+ C! C; C^ C` C~ C?
CT	0.191 / 0.458	C4 C5 C6
N	0.182 / 0.712	NA N2 N* NC NB N3 NT NY Nh ns nm
O	0.166 / 0.879	O2 o1 ob
OH	0.172 / 0.881	ot
OS	0.168 / 0.712	of
S	0.20 / 1.047	SH

Table C-2. Complete list of all equivalent atom types for Lennard-Jones “12-6” potentials implemented into AMBER FF. Note, that uppercase and lowercase letters are recognized as different letters by YASARA (e.g. Nh atom type would be different from nh).

The new united atom types C- and C: developed for octane molecule have Lennard-Jones “12-6” parameters depicted in the Table C-3.

No.	Atom type	σ [nm]	ε [kJ/mol]
1.	C-	0.209	1.103
2.	C:	0.201	0.882
3.	FE	0.065	0.209
4.	mg	0.065	1.047

Table C-3. New atom types developed for octane molecule and for Fe^{3+} and Mg^{2+} ions bonded by coordinate covalent bonds. New atom types C- (represents CH3- group) and C: (represents CH2- group) are united atom types. The atom mass, in g/mol, is 15.035 for C- and 14.027 for C: atom type.

C.1.1.2. New Topology Files for Photosynthetic Pigments

As was mentioned above the subject of interest in our first project presented in this thesis was photosystem II reaction center (PSII RC) from higher plants. The most suitable replacement for missing crystal (or NMR) structure of PSII RC from higher plants is the crystal structure of PSII from *Thermosynechococcus elongatus* [Loll et al. 2005]. In this crystal structure six different types of photosynthetic pigments (or molecules) are located, namely chlorophyll *a* (Chl *a*), pheophytin *a* (Pheo *a*), plastoquinone 9 (PQ9), oxygen evolving complex (OEC), *β*-carotene (*β*-Car) and heme. New FF parameters had to be developed for all these molecules. FF parameters describe all interactions between atoms in the molecular models (see B.1.2. section of this thesis). Some of the existing FF parameters, describing bond interactions such as bond stretching, angle bending and dihedral bending could be adopted from literature [Ceccarelli et al. 2003], but completely new FF parameters had to be developed for Coulomb interactions by *ab initio* quantum-chemical calculations. In the following tables new topology files (without connectivities) for octane, PQ9, Chl *a*, OEC + bicarbonate ion (BC2), heme and *β*-Car molecules are shown (Table C-4, C-5, C-6, C-7, C-8 and C-9). Topology files for neutral and reduced Pheo *a* are listed in a separate section below. In the tables, first column holds names of atoms taken from PDB files (Figure C-29), second column shows subsistent atom types and in the third column newly developed atomic partial charges are given. The charge fitting scheme according to restrained electrostatic potential (RESP) charge fitting method [Bayly et al. 1993] was performed. All atomic partial charges thus have format (RESP) used by AMBER-like FFs [Wang et al. 2000]. It should be noted here, these FF parameters were developed by *ab initio* (HF/6-31G*) calculations in Gaussian 98 [Frisch et al. 1998] and therefore represent required quality for any AMBER-like FF. From the details of development of RESP charges [Bayly et al. 1993], we shall also point out the *ab initio* geometry optimization calculations (optimized geometries of photosynthetic pigments are shown for Pheo *a*, chlorobactene and bacteriochlorophyll *c* in this thesis), which had to be performed before development of RESP charges took place. Molecule full name, tri-letter code (e.g. OCT for octane, CL1 for chlorophyll *a* or HEM for heme) and overall charge are given in the first row of the following tables.

Octane ♦ OCT ♦ 0.0

No.	Atom name	Atom type	RESP atomic charge
1.	CA	C-	0.00
2.	CB	C:	0.00
3.	CC	C:	0.00
4.	CD	C:	0.00
5.	CE	C:	0.00
6.	CF	C:	0.00
7.	CG	C:	0.00
8.	CH	C-	0.00

Table C-4. Topology file (without connectivities) for octane molecule developed for AMBER-like FFs.

Plastoquinone 9 ♦ PL9 ♦ 0.0

No.	Atom name	Atom type	RESP charge	Atom name	Atom type	RESP charge	Atom name	Atom type	RESP charge
1.	C2	C`	-0.52	H21	HC	0.05	C39	C`	0.06
2.	H2	HA	0.25	C22	C5	0.22	C40	C6	-0.13
3.	C3	C`	-0.04	H22	HC	-0.00	H40	HC	0.05
4.	C4	C^	0.58	H22	HC	-0.00	H40	HC	0.05
5.	C5	C`	-0.07	C23	C~	-0.47	H40	HC	0.05
6.	C6	C`	-0.11	H23	HA	0.18	C41	C5	-0.11
7.	C1	C^	0.73	C24	C`	0.06	H41	HC	0.05
8.	C7	C5	0.19	C25	C6	-0.09	H41	HC	0.05
9.	H7	HC	0.02	H25	HC	0.04	C42	C5	0.27
10.	H7	HC	0.02	H25	HC	0.04	H42	HC	-0.01
11.	C8	C~	-0.44	H25	HC	0.04	H42	HC	-0.01
12.	H8	HA	0.17	C26	C5	-0.13	C43	C~	-0.48
13.	C9	C`	0.20	H26	HC	0.05	H43	HA	0.17
14.	C10	C6	-0.28	H26	HC	0.05	C44	C`	0.11
15.	H10	HC	0.09	C27	C5	0.21	C46	C5	-0.13
16.	H10	HC	0.09	H27	HC	0.00	H46	HC	0.05
17.	H10	HC	0.09	H27	HC	0.00	H46	HC	0.05
18.	C11	C5	-0.30	C28	C~	-0.49	C47	C5	0.33

19.	H11	HC	0.09	H28	HA	0.19	H47	HC	-0.03
20.	H11	HC	0.09	C29	C`	0.07	H47	HC	-0.03
21.	C12	C5	0.20	C30	C6	-0.07	C48	C~	-0.62
22.	H12	HC	-0.00	H30	HC	0.03	H48	HA	0.20
23.	H12	HC	-0.00	H30	HC	0.03	C49	C`	0.38
24.	C13	C~	-0.40	H30	HC	0.03	C51	C6	-0.37
25.	H13	HA	0.16	C31	C5	-0.13	H51	HC	0.10
26.	C14	C`	0.08	H31	HC	0.05	H51	HC	0.10
27.	C15	C6	-0.14	H31	HC	0.05	H51	HC	0.10
28.	H15	HC	0.06	C32	C5	0.18	C50	C6	-0.43
29.	H15	HC	0.06	H32	HC	0.02	H50	HC	0.11
30.	H15	HC	0.06	H32	HC	0.02	H50	HC	0.11
31.	C16	C5	-0.15	C33	C~	-0.47	H50	HC	0.11
32.	H16	HC	0.06	H33	HA	0.18	C45	C6	-0.25
33.	H16	HC	0.06	C34	C`	0.06	H45	HC	0.08
34.	C17	C5	0.25	C35	C6	-0.08	H45	HC	0.08
35.	H17	HC	-0.01	H35	HC	0.04	H45	HC	0.08
36.	H17	HC	-0.01	H35	HC	0.04	C52	C6	-0.20
37.	C18	C~	-0.51	H35	HC	0.04	H52	HC	0.08
38.	H18	HA	0.19	C36	C5	-0.12	H52	HC	0.08
39.	C19	C`	0.10	H36	HC	0.05	H52	HC	0.08
40.	C20	C6	-0.14	H36	HC	0.05	C53	C6	-0.22
41.	H20	HC	0.05	C37	C5	0.23	H53	HC	0.09
42.	H20	HC	0.05	H37	HC	-0.00	H53	HC	0.09
43.	H20	HC	0.05	H37	HC	-0.00	H53	HC	0.09
44.	C21	C5	-0.12	C38	C~	-0.48	O1	o1	-0.51
45.	H21	HC	0.05	H38	HA	0.18	O2	o1	-0.53

Table C-5. Topology file (without connectivities) for plastoquinone 9 (PQ9) developed for AMBER-like FFs.

Chlorophyll *a* ♦ CL1 ♦ 0.0									
No.	Atom name	Atom type	RESP charge	Atom name	Atom type	RESP charge	Atom name	Atom type	RESP charge
1.	MG	mg	1.13	C4C	C9	0.10	H6	HC	-0.03
2.	CHA	C#	0.10	CMC	C6	-0.33	H6	HC	-0.03
3.	CHB	C7	-0.66	HMC	HC	0.10	C7	C5	-0.16
4.	HHB	HA	0.19	HMC	HC	0.10	H7	HC	0.03
5.	CHC	C7	-0.29	HMC	HC	0.10	H7	HC	0.03
6.	HHC	HA	0.15	CAC	C5	0.08	C8	C4	0.21
7.	CHD	C7	-0.14	HAC	HC	0.02	H8	HC	-0.01
8.	HHD	HA	0.20	HAC	HC	0.02	C9	C6	-0.41
9.	NA	ns	-0.43	CBC	C6	-0.15	H9	HC	0.10
10.	C1A	C$	-0.13	HBC	HC	0.04	H9	HC	0.10
11.	C2A	C4	0.09	HBC	HC	0.04	H9	HC	0.10
12.	H2A	HC	0.06	HBC	HC	0.04	C10	C5	-0.12
13.	C3A	C4	0.29	ND	nm	-0.48	H10	HC	0.03
14.	H3A	HC	0.00	C1D	C%	0.01	H10	HC	0.03
15.	C4A	C$	0.33	C2D	C8	0.14	C11	C5	0.02
16.	CMA	C6	-0.36	C3D	C8	-0.26	H11	HC	0.01
17.	HMA	HC	0.09	C4D	C&	0.11	H11	HC	0.01
18.	HMA	HC	0.09	CMD	C6	-0.30	C12	C5	-0.18
19.	HMA	HC	0.09	HMD	HC	0.10	H12	HC	0.04
20.	CAA	C5	-0.04	HMD	HC	0.10	H12	HC	0.04
21.	HAA	HC	0.04	HMD	HC	0.10	C13	C4	0.35
22.	HAA	HC	0.04	CAD	C+	0.69	H13	HC	-0.04
23.	CBA	C5	-0.37	OBD	o1	-0.56	C14	C6	-0.42
24.	HBA	HC	0.08	CBD	C4	-0.59	H14	HC	0.10
25.	HBA	HC	0.08	HBD	HC	0.19	H14	HC	0.10
26.	CGA	C!	0.89	CGD	C!	1.04	H14	HC	0.10
27.	O1A	o1	-0.60	O1D	o1	-0.64	C15	C5	-0.21

28.	O2A	of	-0.44	O2D	of	-0.47	H15	HC	0.05
29.	NB	nm	-0.63	CED	C6	0.05	H15	HC	0.05
30.	C1B	C9	0.42	HED	HC	0.07	C16	C5	0.03
31.	C2B	C8	0.09	HED	HC	0.07	H16	HC	0.00
32.	C3B	C8	-0.01	HED	HC	0.07	H16	HC	0.00
33.	C4B	C"	0.19	C1	C5	0.14	C17	C5	-0.17
34.	CMB	C6	-0.33	H1	HC	0.08	H17	HC	0.03
35.	HMB	HC	0.10	H1	HC	0.08	H17	HC	0.03
36.	HMB	HC	0.10	C2	C~	-0.39	C18	C4	0.45
37.	HMB	HC	0.10	H2	HA	0.18	H18	HC	-0.06
38.	CAB	C~	-0.14	C3	C`	0.20	C19	C6	-0.46
39.	HAB	HA	0.15	C4	C6	-0.24	H19	HC	0.10
40.	CBB	C`	-0.39	H4	HC	0.08	H19	HC	0.10
41.	HBB	HA	0.18	H4	HC	0.08	H19	HC	0.10
42.	HBB	HA	0.18	H4	HC	0.08	C20	C6	-0.35
43.	NC	ns	-0.47	C5	C5	-0.29	H20	HC	0.07
44.	C1C	C"	0.20	H5	HC	0.08	H20	HC	0.07
45.	C2C	C8	0.13	H5	HC	0.08	H20	HC	0.07
46.	C3C	C8	-0.21	C6	C5	0.20			

Table C-6. Topology file (without connectivities) for chlorophyll *a* (Chl *a*) developed for AMBER-like FFs.

Note, that atom types used for Chl *a* molecule, as well as for other porphyrin-like pigments, were adopted from structurally similar parts of bacterial photosynthetic pigments [Cecarelli et al. 2003]. New FF parameters had to be developed [Palencar et al. 2005] only for structurally different parts, such as saturated imidazole ring II on chlorine macrocycle ring, vinyl group CH_2=CH- on imidazole ring I, two CO_2-CH_2-CH_2- groups attached to heme, part of phytyl tail, PQ9 head, isoprene units, double-bonds of β-Car, BCT and OEC – BC2 complex.

Oxygen evolving complex + Bicarbonate Ion ♦ OEC + BC2 ♦ 0.0			
No.	Atom name	Atom type	RESP charge
1.	MN1	Mn	0.07
2.	MN2	Mn	1.55
3.	MN3	Mn	1.56
4.	MN4	Mn	0.72
5.	O1	OS	-0.76
6.	O2	OS	-0.83
7.	O3	OS	-0.76
8.	O4	OS	-2.04
9.	CA1	C0	1.63
10.	C	C?	0.71
11.	O1	ob	-0.39
12.	O2	ob	-0.71
13.	O3	ob	-0.76

Table C-7. Topology file (without connectivities) for complex of OEC and BCT developed for AMBER-like FFs.

The most recent crystallographic [Loll et al. 2005; Ferreira et al. 2004] and various biochemical studies confirmed that oxygen evolving complex is formed by manganese cluster, calcium ion Ca^{2+}, chlorine ion Cl^{-1} and bicarbonate ion. Except for putative Cl^{-1} ion, all mention atoms were together considered as one complex (OEC + BC2). Due to medium resolution (0.30 nm) of available PSII crystal structure, the precise geometry and composition of OEC complex is still not known. Here we fixed positions of manganese atoms during *ab initio* geometry optimization calculations in Gaussian 98 to support proposed arrangement of OEC complex found in crystal structure [Loll et al. 2005].

Heme ♦ HEM ♦ 0.0									
No.	Atom name	Atom type	RESP charge	Atom name	Atom type	RESP charge	Atom name	Atom type	RESP charge
1.	FE	FE	0.42	O1A	o1	-0.65	HMC	HC	0.09
2.	CHA	C7	-0.31	O2A	of	-0.69	CAC	C~	-0.10
3.	HHA	HA	0.21	H2A	HO	0.47	HAC	HA	0.14
4.	CHB	C7	-0.11	NB	nm	-0.08	CBC	C`	-0.42
5.	HHB	HA	0.15	C1B	C9	-0.07	HBC	HA	0.18
6.	CHC	C7	0.02	C2B	C8	0.13	HBC	HA	0.18
7.	HHC	HA	0.13	C3B	C8	-0.02	ND	nm	-0.20
8.	CHD	C7	-0.23	C4B	C"	-0.13	C1D	C9	0.00
9.	HHD	HA	0.15	CMB	C6	-0.34	C2D	C8	0.19
10.	NA	nm	-0.17	HMB	HC	0.10	C3D	C8	-0.15
11.	C1A	C"	0.13	HMB	HC	0.10	C4D	C"	0.12
12.	C2A	C8	-0.10	HMB	HC	0.10	CMD	C6	-0.40
13.	C3A	C8	0.15	CAB	C~	-0.10	HMD	HC	0.12
14.	C4A	C9	-0.05	HAB	HA	0.13	HMD	HC	0.12
15.	CMA	C6	-0.35	CBB	C`	-0.42	HMD	HC	0.12
16.	HMA	HC	0.11	HBB	HA	0.18	CAD	C5	0.01
17.	HMA	HC	0.11	HBB	HA	0.18	HAD	HC	0.04
18.	HMA	HC	0.11	NC	nm	-0.13	HAD	HC	0.04
19.	CAA	C5	-0.09	C1C	C"	-0.18	CBD	C5	-0.22
20.	HAA	HC	0.07	C2C	C8	0.14	HBD	HC	0.09
21.	HAA	HC	0.07	C3C	C8	-0.06	HBD	HC	0.09
22.	CBA	C5	-0.15	C4C	C9	0.12	CGD	C!	0.76
23.	HBA	HC	0.08	CMC	C6	-0.28	O1D	o1	-0.60
24.	HBA	HC	0.08	HMC	HC	0.09	O2D	of	-0.64
25.	CGA	C!	0.85	HMC	HC	0.09	H2D	HO	0.47

Table C-8. Topology file (without connectivities) for heme molecule developed for AMBER-like FFs.

Interestingly RESP atomic partial charges of N_A, N_B, N_C and N_D nitrogen atoms of heme at porphyrin head have much lower negative values compare to equivalents from Chl *a* molecule.

β-Carotene ♦ BCR ♦ 0.0									
No.	Atom name	Atom type	RESP charge	Atom name	Atom type	RESP charge	Atom name	Atom type	RESP charge
1.	C1	C4	0.53	C33	C6	-0.37	H29	HC	0.03
2.	C2	C5	-0.17	C34	C6	-0.21	H29	HC	0.03
3.	C3	C5	0.00	C35	C6	-0.21	H31	HC	0.10
4.	C4	C5	-0.13	C36	C6	-0.21	H31	HC	0.10
5.	C5	C`	0.22	C37	C6	-0.21	H31	HC	0.10
6.	C6	C`	-0.38	C38	C6	-0.37	H32	HC	0.08
7.	C7	C~	0.06	C39	C6	-0.35	H32	HC	0.08
8.	C8	C~	-0.30	C40	C6	-0.44	H32	HC	0.08
9.	C9	C`	0.18	H2	HC	0.03	H33	HC	0.10
10.	C10	C~	-0.33	H2	HC	0.03	H33	HC	0.10
11.	C11	C~	-0.01	H3	HC	0.02	H33	HC	0.10
12.	C12	C~	-0.36	H3	HC	0.02	H34	HC	0.07
13.	C13	C`	0.23	H4	HC	0.05	H34	HC	0.07
14.	C14	C~	-0.30	H4	HC	0.05	H34	HC	0.07
15.	C15	C~	-0.13	H7	HA	0.10	H35	HC	0.06
16.	C16	C~	-0.13	H8	HA	0.16	H35	HC	0.06
17.	C17	C~	-0.30	H10	HA	0.16	H35	HC	0.06
18.	C18	C`	0.23	H11	HA	0.15	H36	HC	0.07
19.	C19	C~	-0.36	H12	HA	0.18	H36	HC	0.07
20.	C20	C~	-0.01	H14	HA	0.14	H36	HC	0.07
21.	C21	C~	-0.33	H15	HA	0.18	H37	HC	0.07

22.	C22	C`	0.19	H16	HA	0.18	H37	HC	0.07
23.	C23	C~	-0.31	H17	HA	0.14	H37	HC	0.07
24.	C24	C~	0.06	H19	HA	0.18	H38	HC	0.10
25.	C25	C`	-0.39	H20	HA	0.15	H38	HC	0.10
26.	C26	C`	0.23	H21	HA	0.16	H38	HC	0.10
27.	C27	C5	-0.13	H23	HA	0.16	H39	HC	0.08
28.	C28	C5	0.01	H24	HA	0.10	H39	HC	0.08
29.	C29	C5	-0.17	H27	HC	0.05	H39	HC	0.08
30.	C30	C4	0.53	H27	HC	0.05	H40	HC	0.10
31.	C31	C6	-0.45	H28	HC	0.01	H40	HC	0.10
32.	C32	C6	-0.35	H28	HC	0.01	H40	HC	0.10

Table C-9. Topology file (without connectivities) for β-Carotene (β-Car) developed for AMBER-like FFs.

C.1.1.3. New Topology File for Pheophytin *a* (Pheo-D1)

This section is devoted specially to details on development process of new FF parameters for pheophytin *a* (Pheo *a*) photosynthetic pigment. It will be discussed later on that this particular pigment played crucial role for the light-induced events studied within framework of the first project presented in this thesis. The crucial Pheo *a* will be later on also marked as Pheo-D1 or Pheo *a* 7 from an active branch of PSII RC. Omitting details which will be given later, we shall briefly discuss the reason why two different states (neutral and reduced) of Pheo *a* molecule were needed to be parameterized. It has been shown earlier by Vácha [Vacha et al. 2005; Vacha et al. 2002], that light-induced reduction of Pheo *a* molecule located in the center of reaction center (RC) of photosystem II (PSII) influences circular dichroism (CD) and absorption spectra measured on fully functional samples of PSII RC. It has been proposed that other interactions than excitonic are important and result in a change of conformation of Pheo *a* protein environment and subsequently also in a change of arrangement of PSII RC pigments (Figure C-5) in vicinity to reduced Pheo *a*.

Therefore also changes in atomic partial charges of amino acids in vicinity of Pheo *a* had to be elucidated. Atom coordinates of Pheo *a* pigment as well as all other pigments and amino acids were taken from crystal structure of PSII from *Thermosynechococcus elongatus* [Loll et al. 2005]. However, due to limited precision in atom coordinates determination from crystal structure at 0.30 nm, all geometries of photosynthetic pigments and also side chains of amino acids were optimized by *ab initio* (HF/6-31G*) calculations in Gaussian 98. Comparison of optimized geometries of neutral Pheo *a* and reduced Pheo *a* is shown in the Figure C-1.

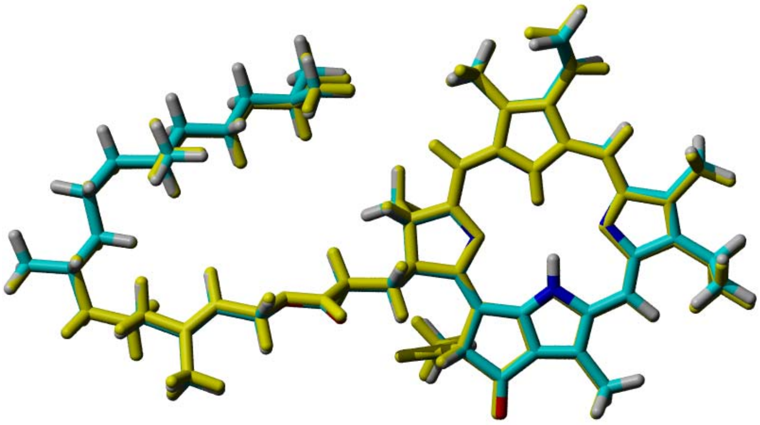

Figure C-1. Comparison of geometries of neutral and reduced Pheo *a* optimized by *ab initio* quantum-chemical calculations (HF/6-31G*) in Gaussian 98. Molecules are shown in stick representation and are superposed on each other according heavy atoms. Neutral Pheo *a* is shown in element colors (carbon in cyan, oxygen in red, nitrogen in blue and hydrogen in gray) and reduced Pheo *a* in yellow. Reduced Pheo *a* pigment is negatively charged due to donation of one electron from the primary donor of PSII RC. RMSD of heavy atoms was 0.009 nm and RMSD of all atoms including hydrogens was 0.013 nm. See the text for more details on abbreviations.

C.1.1.4. Charge Distribution on Reduced Pheo-D1 Environment

In this section we will discuss results from *ab initio* quantum-chemical calculations performed in order to elucidate whether donated electron is distributed over larger system or stayed delocalized on Pheo-D1 molecule. This information was necessary for further development of new FF parameters, and especially for development of RESP atomic partial charges [Wang et al. 2000]. From the literature (and from the well-known characteristics of porphyrin macrocycle group) it is known that electron donated to Pheo-D1 molecule will mainly stay within delocalized π-electrons localized above and below the porphyrin macrocycle head group of Pheo-D1.

Therefore only those amino acids in vicinity to the head group of Pheo-D1 were included in *ab initio* calculations. It should be noted here, that atom coordinates of all amino acids as well as Pheo-D1 were taken from our equilibrated model of PSII RC (details on preparation of Eq-PSII RC model are given in separate section). Together 21 amino acids were chosen from the surroundings of Pheo-D1 and are shown in the Figure C-2.

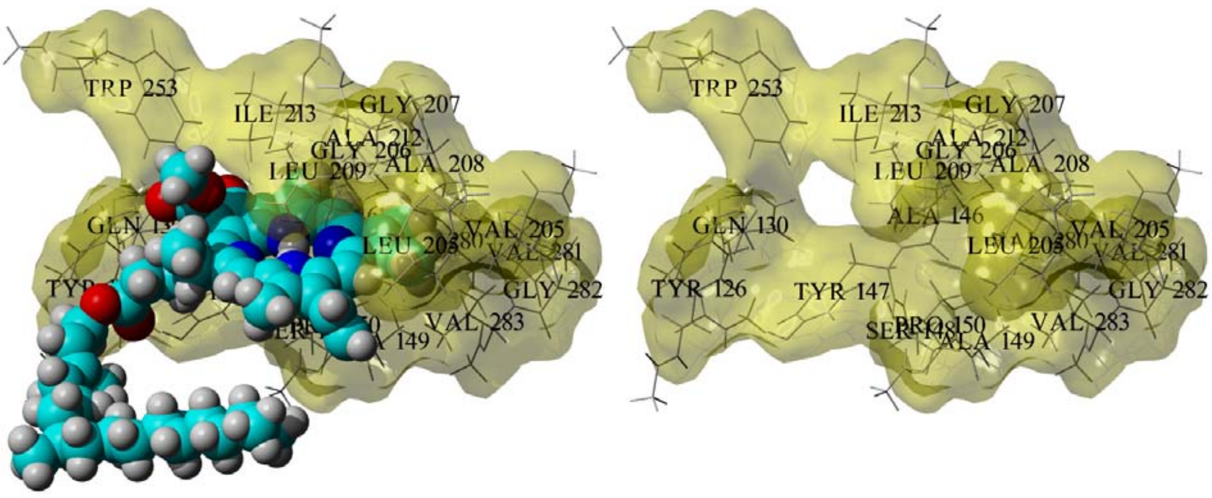

Figure C-2. Molecule of Pheo-D1 shown as space-filling model in element color and 21 amino acids in vicinity of head group of Pheo-D1 shown as transparent yellow molecular surface and gray stick model inside (left). For better readability of amino acids three-letters codes also the view without molecule of Pheo-D1 is shown (right). Geometries were taken from Eq-PSII RC model (for details on Eq-PSII RC model preparation see the text). Rendered in Pov-Ray and prepared in YASARA.

The Figure C-3 shows summarized results from *ab initio* quantum-chemical calculations performed in Gaussian 98. The biggest change in overall charge was observed for proline PRO 150 (+0.038 e$^-$), while charge changes of other amino acids were smaller than ~0.02 e$^-$. From the comparison of changes in overall amino acid charges and changes in overall charge of Pheo-D1 molecule, we may conclude that only 5% of donated electron was delocalized onto Pheo-D1 protein environment, 1% onto atoms of Pheo-D1 phytyl tail and almost 94% onto Pheo-D1 macrocycle head group. Therefore RESP atomic partial charges of Pheo-D1 were further developed for Pheo-D1 molecule alone (for neutral and reduced form).

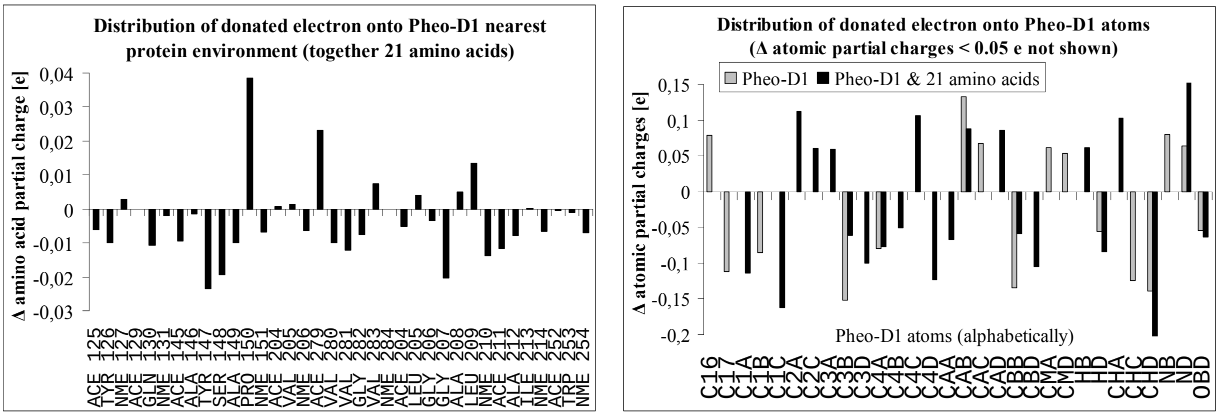

Figure C-3. Distribution of donated electron onto Pheo-D1 protein environment (left) and Pheo-D1 atoms (right). In the graph, residua names and numbers (left) and Pheo-D1 atom names (right) were taken from the crystal structure PDB ID 1S5L [Ferreira et al. 2004]. Abbreviation ACE is used for acetyl N-terminal cap group and NME for C-terminal (-NH-CH3) cap group. All *ab initio* quantum-chemical calculations were performed in Gaussian 98.

In the following tables new topology files (without connectivities) for neutral and reduced Pheo-D1 molecule are given. Reduced Pheo-D1 has negative overall charge due to electron donation by primary electron donor from PSII RC (see the *Primary Photochemistry* section of this thesis for more details).

Pheophytin *a* ♦ PH0 ♦ 0.0

No.	Atom name	Atom type	RESP charge	Atom name	Atom type	RESP charge	Atom name	Atom type	RESP charge
1.	CHA	C#	0.10	C4C	C9	0.13	C6	C5	0.14
2.	CHB	C7	-0.47	CMC	C6	-0.35	H6	HC	-0.01
3.	HHB	HA	0.17	HMC	HC	0.11	H6	HC	-0.01
4.	CHC	C7	-0.27	HMC	HC	0.11	C7	C5	-0.30
5.	HHC	HA	0.16	HMC	HC	0.11	H7	HC	0.07
6.	CHD	C7	-0.16	CAC	C5	0.11	H7	HC	0.07
7.	HHD	HA	0.21	HAC	HC	0.01	C8	C4	0.31
8.	NA	ns	-0.27	HAC	HC	0.01	H8	HC	-0.02
9.	C1A	C$	-0.10	CBC	C6	-0.14	C9	C6	-0.41
10.	C2A	C4	0.10	HBC	HC	0.04	H9	HC	0.09
11.	H2A	HC	0.07	HBC	HC	0.04	H9	HC	0.09
12.	C3A	C4	0.23	HBC	HC	0.04	H9	HC	0.09
13.	H3A	HC	0.01	ND	Nh	-0.04	C10	C5	-0.17
14.	C4A	C$	0.26	HD	hm	0.15	H10	HC	0.05
15.	CMA	C6	-0.57	C1D	C%	-0.09	H10	HC	0.05
16.	HMA	HC	0.15	C2D	C8	0.15	C11	C5	0.09
17.	HMA	HC	0.15	C3D	C8	-0.31	H11	HC	-0.00
18.	HMA	HC	0.15	C4D	C&	0.01	H11	HC	-0.00
19.	CAA	C5	-0.03	CMD	C6	-0.29	C12	C5	-0.27
20.	HAA	HC	0.04	HMD	HC	0.10	H12	HC	0.06
21.	HAA	HC	0.04	HMD	HC	0.10	H12	HC	0.06
22.	CBA	C5	-0.40	HMD	HC	0.10	C13	C4	0.33
23.	HBA	HC	0.10	CAD	C+	0.77	H13	HC	-0.04
24.	HBA	HC	0.10	OBD	o1	-0.58	C14	C6	-0.37
25.	CGA	C!	0.99	CBD	C4	-0.58	H14	HC	0.08
26.	O1A	o1	-0.65	HBD	HC	0.21	H14	HC	0.08
27.	O2A	of	-0.56	CGD	C!	0.88	H14	HC	0.08
28.	NB	Nh	-0.15	O1D	o1	-0.60	C15	C5	-0.15
29.	HB	hm	0.17	O2D	of	-0.40	H15	HC	0.03
30.	C1B	C9	0.1	CED	C6	0.06	H15	HC	0.03
31.	C2B	C8	0.15	HED	HC	0.06	C16	C5	0.09
32.	C3B	C8	0.03	HED	HC	0.06	H16	HC	-0.02
33.	C4B	C"	0.04	HED	HC	0.06	H16	HC	-0.02
34.	CMB	C6	-0.37	C1	C5	0.41	C17	C5	-0.22
35.	HMB	HC	0.12	H1	HC	0.01	H17	HC	0.06
36.	HMB	HC	0.12	H1	HC	0.01	H17	HC	0.06
37.	HMB	HC	0.12	C2	C~	-0.44	C18	C4	0.40
38.	CAB	C~	-0.15	H2	HA	0.17	H18	HC	-0.04
39.	HAB	HA	0.15	C3	C`	0.14	C19	C6	-0.50
40.	CBB	C`	-0.39	C4	C6	-0.27	H19	HC	0.11
41.	HBB	HA	0.19	H4	HC	0.10	H19	HC	0.11
42.	HBB	HA	0.19	H4	HC	0.10	H19	HC	0.11
43.	NC	ns	-0.30	H4	HC	0.10	C20	C6	-0.42
44.	C1C	C"	0.17	C5	C5	-0.14	H20	HC	0.10
45.	C2C	C8	0.18	H5	HC	0.05	H20	HC	0.10
46.	C3C	C8	-0.28	H5	HC	0.05	H20	HC	0.10

Table C-10. Topology file (without connectivities) for neutral Pheo *a* developed for AMBER-like FFs.

Pheophytin *a* ♦ PHO ♦ -1.0									
No.	Atom name	Atom type	RESP charge	Atom name	Atom type	RESP charge	Atom name	Atom type	RESP charge
1.	CHA	C#	0.07	C4C	C9	0.17	C6	C5	0.15
2.	CHB	C7	-0.50	CMC	C6	-0.36	H6	HC	-0.01
3.	HHB	HA	0.15	HMC	HC	0.10	H6	HC	-0.01
4.	CHC	C7	-0.39	HMC	HC	0.10	C7	C5	-0.30
5.	HHC	HA	0.16	HMC	HC	0.10	H7	HC	0.06
6.	CHD	C7	-0.30	CAC	C5	0.17	H7	HC	0.06
7.	HHD	HA	0.22	HAC	HC	-0.02	C8	C4	0.31
8.	NA	ns	-0.29	HAC	HC	-0.02	H8	HC	-0.02
9.	C1A	C$	-0.10	CBC	C6	-0.15	C9	C6	-0.42
10.	C2A	C4	0.14	HBC	HC	0.03	H9	HC	0.09
11.	H2A	HC	0.06	HBC	HC	0.03	H9	HC	0.09
12.	C3A	C4	0.23	HBC	HC	0.03	H9	HC	0.09
13.	H3A	HC	-0.00	ND	Nh	0.03	C10	C5	-0.15
14.	C4A	C$	0.18	HD	hm	0.09	H10	HC	0.04
15.	CMA	C6	-0.50	C1D	C%	-0.06	H10	HC	0.04
16.	HMA	HC	0.12	C2D	C8	0.10	C11	C5	0.09
17.	HMA	HC	0.12	C3D	C8	-0.35	H11	HC	-0.00
18.	HMA	HC	0.12	C4D	C&	-0.02	H11	HC	-0.00
19.	CAA	C5	-0.07	CMD	C6	-0.24	C12	C5	-0.27
20.	HAA	HC	0.06	HMD	HC	0.07	H12	HC	0.05
21.	HAA	HC	0.06	HMD	HC	0.07	H12	HC	0.05
22.	CBA	C5	-0.40	HMD	HC	0.07	C13	C4	0.32
23.	HBA	HC	0.09	CAD	C+	0.79	H13	HC	-0.03
24.	HBA	HC	0.09	OBD	o1	-0.64	C14	C6	-0.37
25.	CGA	C!	1.01	CBD	C4	-0.62	H14	HC	0.08
26.	O1A	o1	-0.66	HBD	HC	0.20	H14	HC	0.08
27.	O2A	of	-0.56	CGD	C!	0.90	H14	HC	0.08
28.	NB	Nh	-0.07	O1D	o1	-0.62	C15	C5	-0.17
29.	HB	hm	0.17	O2D	of	-0.40	H15	HC	0.03
30.	C1B	C9	0.07	CED	C6	0.08	H15	HC	0.03
31.	C2B	C8	0.13	HED	HC	0.05	C16	C5	0.17
32.	C3B	C8	-0.13	HED	HC	0.05	H16	HC	-0.03
33.	C4B	C"	0.05	HED	HC	0.05	H16	HC	-0.03
34.	CMB	C6	-0.32	C1	C5	0.42	C17	C5	-0.33
35.	HMB	HC	0.09	H1	HC	0.00	H17	HC	0.07
36.	HMB	HC	0.09	H1	HC	0.00	H17	HC	0.07
37.	HMB	HC	0.09	C2	C~	-0.42	C18	C4	0.42
38.	CAB	C~	-0.02	H2	HA	0.17	H18	HC	-0.03
39.	HAB	HA	0.12	C3	C`	0.12	C19	C6	-0.48
40.	CBB	C`	-0.52	C4	C6	-0.27	H19	HC	0.11
41.	HBB	HA	0.18	H4	HC	0.09	H19	HC	0.11
42.	HBB	HA	0.18	H4	HC	0.09	H19	HC	0.11
43.	NC	ns	-0.32	H4	HC	0.09	C20	C6	-0.42
44.	C1C	C"	0.13	C5	C5	-0.13	H20	HC	0.10
45.	C2C	C8	0.21	H5	HC	0.04	H20	HC	0.10
46.	C3C	C8	-0.28	H5	HC	0.04	H20	HC	0.10

Table C-11. Topology file (without connectivities) for reduced Pheo *a* developed for AMBER-like FFs.

Note, the difference in tri-letter code for neutral (PH0) and reduced (PHO) form of Pheo-D1. Similarly, performed MD simulations were named according the form of the Pheo-D1 molecule involved in the models.

C.1.1.5. New FF Parameters for Photosynthetic Pigments

In the previous sections new atom types, Lennard-Jones parameters and new topology files developed for photosynthetic pigments located in the RC of PSII were presented. Further also new FF parameters for bond interactions namely, bonds and angles are given. Majority of the FF parameters describing dihedral bending were adopted (with some exceptions) from other sources [Ceccarelli et al. 2003; Autenrieth et al. 2004] and original FFs [Cornell et al. 1995; MacKerell et al. 1998]. The complete list of developed and adopted FF parameters for bonds, angles and dihedrals found in all photosynthetic pigments of PSII RC as well as for all other non-protein molecules such as OEC, *β*-Car, PQ9 and BCT has been adopted into YASARA's FF file (amber99.fof) and is thus freely available in an electronic form. Only small part of this large set of FF parameters is presented in this section, due to extended size of the FF set and limits of this thesis. However, all FF parameters, which had to be developed by *ab initio* quantum-chemical calculations as completely new (due to the fact, that no equivalent FF parameters could be found in the existing FF sets), are listed in the following tables. Atom types given here (Figure C-4) were originally developed for CHARMM FF [MacKerell et al. 1998], but their equivalents for AMBER-like FF could be easily obtained by comparison with Ceccarelli's set [Ceccarelli et al. 2003] and also from the list of *New Atom Types* presented in this thesis. Details on development of new FF parameters for bonds and angles of PSII RC pigments and other non-protein molecules could be found in our paper [Palencar et al. 2005]. All new FF parameters were developed by performing series of (HF/6-31G*) *ab initio* quantum-chemical calculations in Gaussian 98, with exception for those obtained in HyperChem.

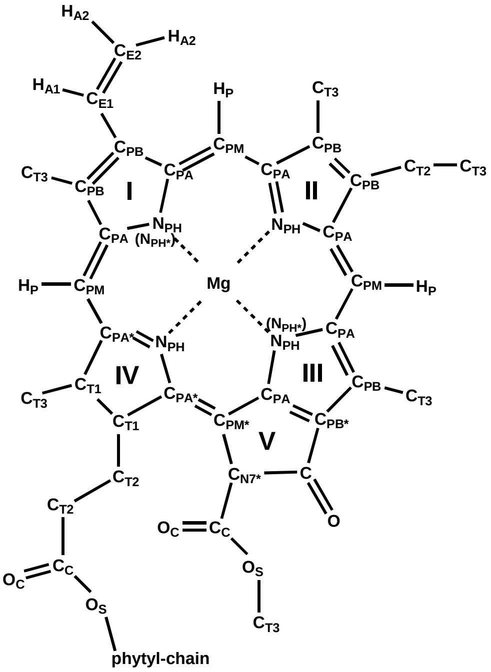

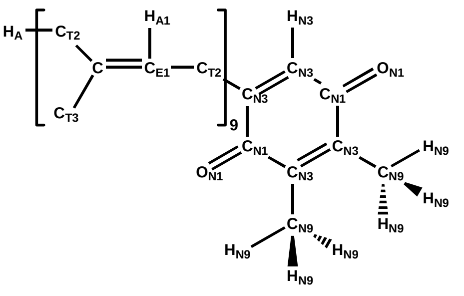

Figure C-4. Chemical structures of two photosynthetic molecules from the PSII RC, chlorophyll *a* (Chl *a*) (left) and plastoquinone 9 (PQ9) (right), including FF atom types. Phytyl chain (consisting of four isoprene units, of which three are saturated) of Chl *a* is not shown for clarity and no labels are given for hydrogen atoms attached to sp^3 carbons, their atom type is H_A. For more details see the paper [Palencar et al. 2005].

Given the similarity between the molecular structure of Chl *a* and pheophytin *a* (Pheo *a*), the same atom types are used for corresponding atoms in both chromophores. Only for the nitrogens on the pyrrole rings of Pheo *a* bound to hydrogens, different atom type was used to account for deviations of angle bendings (N_{PH*} for Pheo *a* instead of N_{PH} for Chl *a*). Five new atom types added to CHARMM27 were named as follows, N_{PH*} (for Pheo *a*), C_{N7*} and three (porphyrin *α*, *β*, and *meso*) C_{PA*}, C_{PB*}, C_{PM*} carbons. The rest of atom types were fitted according to CHARMM27 developing scheme [MacKerell et al. 1998]. New FF parameters for bonds found in Chl *a* and Pheo *a* molecules obtained by *ab initio* quantum-chemical calculations in Gaussian 98 and HyperChem are listed in the Table C-12. Five new atom types named N_{PH*}, C_{N7*}, C_{PM*}, C_{PB*} and C_{PA*} are closely related to original CHARMM27 atom types N_{PH}, C_{N7}, C_{PM}, C_{PB} and C_{PA} originally defined for heme prosthetic group. The rest of atom types of PSII RC pigments were fitted according to CHARMM27 developing scheme [MacKerell et al. 1998]. Bonds from closed ring structures could not be obtained in HyperChem, due to the necessity of ring disruption. Parameters for N_{PH*}—H and N_{PH}—Mg bonds were calculated only in HyperChem due to the convergence criterion problem in Gaussian 98.

Bond	Length(1) [nm]	Force constant [MJ mol^{-1} nm^{-2}]	Length [nm]	Force constant [MJ mol^{-1} nm^{-2}]
C_{E2}—C(2)	0.133	241.2	0.132	242.8
C_{N7*}—C_C	0.150	112.4	0.151	101.9
C_{N7*}—C	–	–	0.154	90.5
C_{N7*}—C_{PM*}	–	–	0.152	99.5
C_{N7*}—H_A	0.108	138.0	0.108	136.3
C_{PB*}—C	–	–	0.147	116.8
C_{PA}—C_{PB*}	–	–	0.136	197.1
C_{PA*}—C_{T1}	–	–	0.152	98.6
C_{PA}—C_{PM*}	–	–	0.146	125.1
C_{PB}—C_{PB*}	–	–	0.143	132.6
N_{PH*}—H	0.099	212.0	–	–
N_{PH}—Mg(3)	0.210	29.5	–	–
O_S—C_C	0.132	196.7	0.133	172.6
O_S—C_{T2}	0.142	141.6	0.143	120.1
C_{N3}—C_{T2}	–	–	0.151	105.9
C_{N3}—C_{N9}	–	–	0.150	106.5

Table C-12. Comparison of new bond FF parameters (equilibrium bond lengths and force constants) of three PSII RC photosynthetic pigments, Chl *a*, Pheo *a* and PQ9 developed by RHF/6-31G* *ab initio* calculations in HyperChem and Gaussian 98. (1) Bond parameters obtained from RHF/6-31G* potential energy surface scan (PES) calculation in HyperChem are listed in the first two columns and those in Gaussian 98 are listed in the last two columns. **(2)** Bond C_{E2}—C is involved in phytyl tail of Chl *a* and Pheo *a* molecules. **(3)** Parameters for N_{PH}—Mg bond were calculated at UHF/6-31G* in HyperChem. For more details see the paper [Palencar et al. 2005].

New FF parameters for angles found in Chl *a* and Pheo *a* molecules obtained by *ab initio* quantum-chemical calculations in Gaussian 98 are listed in the Table C-13. These FF parameters were developed in the same way as those for bonds and thus represent required quality for any AMBER-like FF.

(A)

Angles from chlorin head group of Chl *a* and Pheo *a*			
No.	Angle atom1 - at.2 - at.3	Θ (Theta) [degree]	k_{Θ} (FF constant) [kJ mol^{-1} rad^{-2}]
1.	C_{PM*}—C_{PA*}—N_{PH}	125.8	592.8
2.	C_{T1}—C_{PA*}—C_{PM}	120.7	576.4
3.	C_{T1}—C_{PA*}—C_{PM*}	126.7	561.2
4.	C_{T1}—C_{PA*}—N_{PH}	115.4	987.6
5.	C_{T2}—C_{T1}—C_{PA*}	112.4	301.8
6.	C_{T3}—C_{T1}—C_{PA*}	112.4	301.8
7.	H_{A}—C_{T1}—C_{PA*}	110.0	230.8
8.	C_{PA*}—N_{PH}—Mg	124.5	80.3

(B)

Angles from Phytyl tail of Chl *a* and Pheo *a*			
No.	Angle atom1 - at.2 - at.3	Θ (Theta) [degree]	k_{Θ} (FF constant) [kJ mol^{-1} rad^{-2}]
1.	C—C_{E1}—C_{T2}	125.6	340.3
2.	C—C_{E1}—H_{A1}	119.0	293.7
3.	C_{C}—O_{S}—C_{T2}	117.4	413.7
4.	C_{C}—O_{S}—C_{T3}	116.6	424.9
5.	C_{E1}—C—C_{T2}	124.8	449.4
6.	C_{E1}—C—C_{T3}	120.9	472.3
7.	C_{E1}—C_{T2}—H_{A}	111.2	265.5
8.	C_{T2}—C—C_{T3}	115.4	448.2
9.	H_{A1}—C_{E1}—C_{T2}	110.3	294.0
10.	O_{C}—C_{C}—O_{S}	122.8	712.0
11.	O_{S}—C_{C}—C_{T2}	111.8	488.1
12.	O_{S}—C_{T2}—C_{E1}	106.8	429.9

Table C-13. New angle FF parameters for Chl *a* and Pheo *a* molecules developed by *ab initio* (HF/6-31G*) quantum-chemical calculations performed in Gaussian 98. (A) Angle FF parameters for angles located in the chlorin head group of Chl *a* and Pheo *a* molecules. (B) Angle FF parameters for angles located in the phytyl tail of Chl *a* and Pheo *a* molecules. The developing scheme was identical to the one described in the paper [Palencar et al. 2005], except for the fact, that all *ab initio* quantum-chemical calculations were performed in Gaussian 98.

All QM calculations, concerning molecular geometry optimizations and FF parameters development, were performed using Gaussian 98 [Frisch et al. 1998]. The AMBER-like atomic partial RESP charges [Wang et al. 2000] were obtained by Antechamber, which is an accessory module of the AMBER 7 [Case et al. 2002].

C.1.2. Preparation of Equilibrated PSII RC Model

C.1.2.1. Composition of the PSII RC Model

Initial 3D molecular structure of PSII RC was adopted from experimental crystal structure from *Thermosynechococcus elongatus* at 3.0Å resolution (PDB ID 2AXT) [Loll et al. 2005]. The model involved D1 and D2 proteins, light harvesting proteins CP47 and CP43, a hererodimer of cytochrome b_{559}, and nine small membrane proteins (psbH, psbI, psbJ, psbK, psbL, psbM, psbT, psbX and psbZ). Three membrane extrinsic subunits, PsbO, PsbU and PsbV, interacting with the extended loop regions of D1, D2, CP43 and CP47 are rather far from membrane parts of the PSII RC complex and have not been included in the model. Chlorin cofactors, six Chl *a* molecules and two Pheo *a* molecules, arranged in the heterodimeric D1/D2 subunits with pseudo-C2 symmetry have been numbered as: Chl-*a*-3, Chl-*a*-4, Chl-*a*-5, Chl-*a*-6, Pheo-*a*-7, Pheo-*a*-8, Chl-*a*-9 and Chl-*a*-10 (Figure C-5) according crystal structure PDB ID 1S5L [Ferreira et al. 2004]. Other cofactors, eleven beta-carotenes (*β*-Car), one non-heme iron, $Fe2^+$, one heme of cytochrome b_{559} and the Mn_4–Ca cluster (forming the water oxidation catalytic site), were also included in our model.

C.1.2.2. Correct Protonation and Modeling of Missing Parts of PSII RC Model

The disulphide bond between D1-Cys 212 and D2-Cys 211 was created. Protonation of His, Asp and Glu residues was predicted by pKa prediction subroutine embedded in molecular modeling package YASARA (Yasara Biosciences, *http://www.yasara.org/index.html*; [Krieger et al. 2004]). The carboxyl groups of all Asp and Glu residues were not protonated. Two histidines, CP47-His 157 and CP47-His 201, were protonated at the N_{E2} nitrogen. Twelve histidines, D1-His 92, D1-His 190, D1-His 195, D1-His 337, CP47-His 343, CP43-His 74, CP43-His 91, CP43-His 398, D2-His 61, D2-His 87, D2-His 189 and D2-His 336 were protonated at N_{D1} and N_{E2} nitrogens. In order to obtain appropriate initial geometries, the rest of His residues were protonated at N_{D1} nitrogen. Missing N-terminal and C-terminal residues, parts of phytyl tails and some isoprene units were modeled in YASARA and ModLoop server (http://alto.compbio.ucsf.edu/modloop/modloop.html). Hydrogen atoms of protein part of PSII RC complex were added automatically by modeling package WHAT IF [Vriend 1990] or added manually.

C.1.2.3. Geometry Optimization and Energy Minimization of PSII RC Model

The model of PSII RC was put into the simulation cell with dimensions extended by 1.2 nm from the maximal model dimensions along each axis. Final cell dimensions after energy minimization and geometry optimization were 14.82 nm x 12.46 nm x 11.06 nm. The size of the cell ensured that no self-interaction of PSII RC complex would appear during MD simulation.

In order to simulate the infinite size of the system and to establish the natural-like density of the whole cell the periodic boundaries were used for cell walls. The natural environment of the PSII RC pigment-protein complex, thylakoid membrane, was replaced by assembly of octane molecules [Matyus et al. 2006; Stockner et al. 2004; Aliste et al. 2003; Tieleman et al. 2001] due to the lack of electron density for lipid components and computationally demanding geometry optimization of lipid-protein complexes. The middle part of the cell was filled up with octane while the extrinsic parts of PSII RC complex, located in the center of the cell, were solvated by water (Figure C-6). The cavities around D2-PQ9, OEC and putative water channel were also partially filled with water molecules. First, close contacts between PSII RC pigment-protein complex and octane molecules were let to equilibrate by combination of geometry optimization and further MD optimization.

Fixation of positions of all pigment molecules, extrinsic water molecules and Cα backbone carbons were needed to avoid unfavorable conformational changes. After 500 ps of MD simulation protein subunits and water molecules, forming the walls and enters of the buried PSII RC cavities, were released to move. Octane and water molecules could freely penetrate and fill the cavities. Additional octane molecules gradually entered the system until natural-like density of octane environment was achieved. Next, also extrinsic water molecules were released to move. An equilibrated contact layer between octane and water was observed approximately after 2 ns simulation. At this point all atoms in the simulation cell were released and MD simulation with time step of 1.0 fs(1) was used to complete the geometry optimization. The content of the simulation cell was neutralized by 13 sodium cations (by using automatic procedure for a cell neutralization and pKa prediction in YASARA).

The net charge of the cell after correction of two histidines close to the OEC was -2. Except for the last 1 ns of an equilibrated model of PSII RC (Eq-PSII RC) preparation, where NPT ensemble was used, NVT ensemble was used during the whole energy minimization and geometry optimization process. The process was finished when there was no change in dimensions of the simulation cell and a root-mean-square deviation (RMSD) of positions of

PSII RC pigments (Figure C-5) and Cα carbons was fluctuated around values that were typical for a thermal movement (0.06 - 0.08 nm).

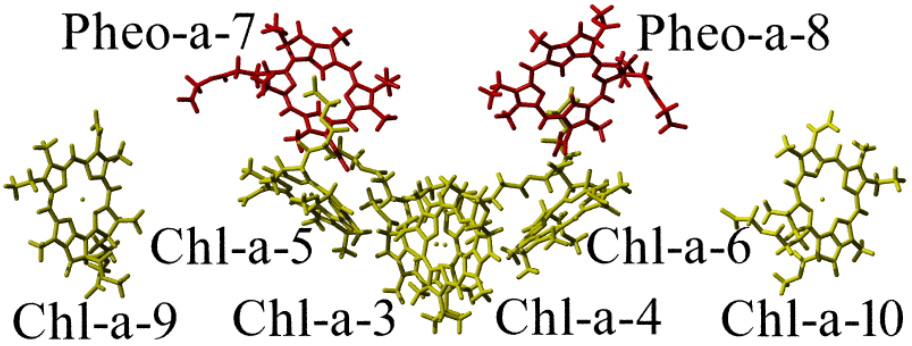

Figure C-5. The nomenclature and spatial organization of PSII RC pigments according crystal structure PDB ID 1S5L [Ferreira et al. 2004]. The pigments numbered with odd values represent active branch and those with even numbers represent inactive branch of PSII RC complex. The special pair chlorophylls are labeled as Chl-*a*-3 and Chl-*a*-4, accessory chlorophylls as Chl-*a*-5 and Chl-*a*-6, two pheophytins as Pheo-*a*-7 and Pheo-*a*-8 and two peripheral chlorophylls as Chl-*a*-9 and Chl-*a*-10. For reduced Pheo-*a*-7 also Pheo-D1 abbreviation is used. Only chlorine head groups of all pigments are shown for clarity. Pigments are oriented along the plane of thylakoid membrane with stromal side heading up.

A total simulation time of Eq-PSII RC model was approximately 5 ns. The application of relatively small octane molecules provides their relatively fast equilibration (generally from 1 to 3 ns) [Stockner et al. 2004], in contrast to complexes containing lipid layers [Tieleman 2006; MacCallum and Tieleman 2006] with a typical equilibration time from 10 to 20 ns.

The final Eq-PSII RC model contained overall 204680 atoms, including 26.582 water molecules, 2.411 octanes and 13 sodium cations. The resulting Eq-PSII RC model embedded in the simulation cell is shown in the Figure C-6. Multiple time step of 1 fs for intramolecular and 2 fs for intermolecular forces was found the most appropriate. Cutoff 0.8 nm was used for Lennard-Jones and electrostatic interactions.

To treat the long-range electrostatic interactions outside the cutoff region the Particle Mesh Ewald method [Essmann et al. 1995] with a grid spacing < 0.1 nm, 4th order B-splines and a tolerance of 10^{-4} for the direct space sum were used. The temperature was adjusted by Berendsen thermostat [Berendsen et al. 1984] based on the time-averaged temperature.

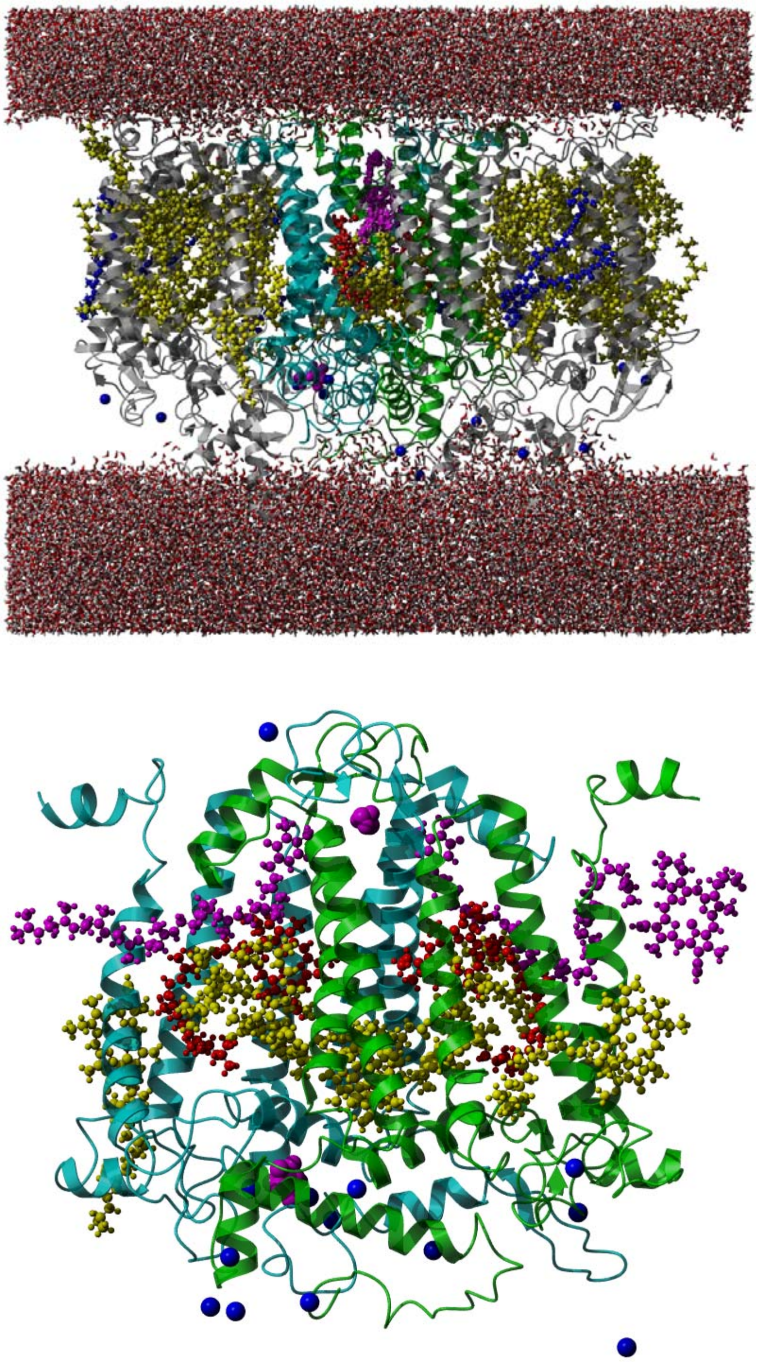

Figure C-6. Equilibrated PSII RC model (Eq-PSII RC) embedded in a periodic simulation cell (upper) and detail on D1 and D2 protein rotated 90 degrees left according vertical axis (lower). View along the thylakoid membrane with a stromal side of PSII RC pigment-protein complex heading up. The water layers are located above and below the centered PSII RC complex, the molecules of water are represented by red (oxygen) and white (hydrogen) sticks. The protein part of PSII RC is shown as ribbon model, the non-protein part of PSII RC as ball-and-stick model. Octane environment that surrounds PSII RC complex and simulation cell are hidden for clarity. Counter ions, which are localized mainly at the lumenal surface of PSII RC complex, are shown as blue balls. Coloring scheme is as follows, D1 protein in cyan, D2 protein in green, other protein subunits in gray, Chl *a* pigments in yellow, Pheo *a* pigment in red, *β*-Cars in blue (hidden in the right picture), PQ9s and Fe^{2+} non-heme iron and heme and OEC in magenta. Pictures were rendered in Pov-Ray as parallel (non-perspective) projection and prepared in YASARA.

C.1.3. Molecular Dynamics Simulations

We have performed six various MD simulations on Eq-PSII RC models simulating our previous experimental conditions [Vacha et al. 2005; Vacha et al. 2002]. To account for wide range of dynamic motions in Eq-PSII RC model, 1 fs time step of 20 ns MD trajectories has been chosen. MD simulations on dark-adapted Eq-PSII RC model with all pigments in neutral form at temperatures 298 K and 77 K have been marked as a Neutral-MD. MD simulations on the light-adapted Eq-PSII RC model, with negative charge on Pheo-D1, have been marked as a Pheo$^-$-MD. Finally, MD simulations of light-adapted Eq-PSII RC model, with slightly different starting conditions from Pheo$^-$-MD, were marked as a collateral-Pheo$^-$-MD simulations. Schematic representation of MD simulations described above, omitting collateral Pheo$^-$-MD simulations, is given in the Figure C-7. We shall stress that neutral form of Pheo-D1 (marked as PH0 in the FF) was involved in so-called dark-adapted Eq-PSII RC models, which were used for Neutral-MD simulations, while reduced, negatively charged, Pheo-D1 (marked as PHO in the FF) was involved in so-called light-adapted Eq-PSII RC models, which served as molecular models for Pheo$^-$-MD simulations. Collateral MD simulations could be also named as parallel MD simulations performed for two main reasons, namely for better statistics supporting obtained results and as a control MD simulations minimizing unfavorable numerical error possibly developed during relatively-long simulation runs.

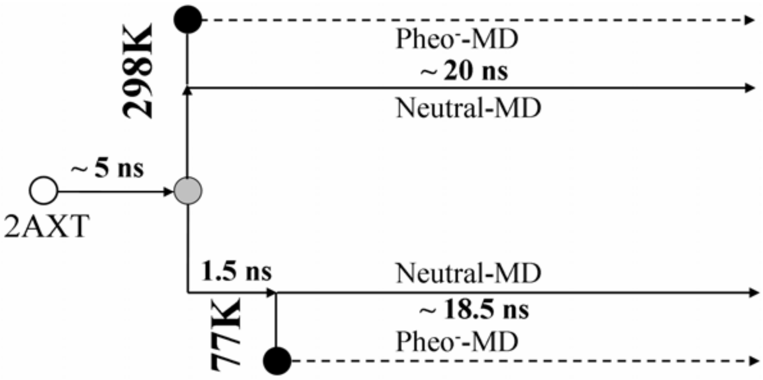

Figure C-7. Schematic representation of Eq-PSII RC model preparation and four parallel MD simulations on the dark-adapted and the light-adapted Eq-PSII RC models. 2AXT corresponds to the X-ray crystal structure of PSII RC [Loll et al. 2005]. Gray circle represents Eq-PSII RC model obtained after ~5 ns of energy minimization and geometry optimization. Two black circles, located at the beginning of 77K-branch and 298K-branch, highlight the point, where Pheo-D1 was reduced. Short 1.5 ns long section prior to 77K-branch illustrates further energy minimization and geometry optimization of Eq-PSII RC model originally prepared at 298 K. For more details on preparation process see the text.

C.1.4. Analysis of Molecular Dynamics Trajectories

C.1.4.1. Changes of PSII RC Pigments Arrangement and Conformational Changes

According to our hypothesis, conformational changes might occur in Pheo$^-$-MD simulations, particularly close to the position of reduced Pheo-D1. These conformational changes have been evaluated by the root-mean-square deviation (RMSD) of Cα carbons positions within D1 and D2 protein subunits. The X-ray crystal structure of PSII (PDB ID 2AXT) was used as a reference structure for all Cα RMSD calculations. Translation and rotation of PSII RC complex in the simulation cell was eliminated during MD simulation by using superposition. In order to get more details on the conformational changes within MD simulations three spherical protein layers of Eq-PSII RC model were selected at different distances from Pheo-D1 head group. The first spherical protein layer within 0.23 nm from Pheo-D1 head group (marked as 0.23 nm-Cα layer) involves D1-Tyr 126, D1-Gln 130, D1-Tyr 147, D1-Val 283, D2-Leu 205, D2-Leu 209 and D2-Ala 212 amino acids. The second protein layer defined within distance range of 0.23 nm – 0.5 nm from Pheo-D1 head group (0.5 nm-Cα layer) involves D1-Ile 143, D1-Ala 146, D1-Ala 149, D1-Pro 150, D1-Val 205, D1-Pro 279, D1-Val 280, D2-Ala 208, D2-Cys 211, D2-Ile 213, D2-Ala 216, D2-Trp 253, D2-Ile 256 and D2-Phe 257. The last protein layer (0.7 nm-Cα layer) contains 24 amino acids of D1 and 13 amino acids of D2 protein subunit. The results of conformational analysis of Neutral-MD and Pheo$^-$-MD simulations at 298 K for selected protein layers are shown in the Figure C-8. As we expected no significant conformational changes were detected at 77 K (data not shown).

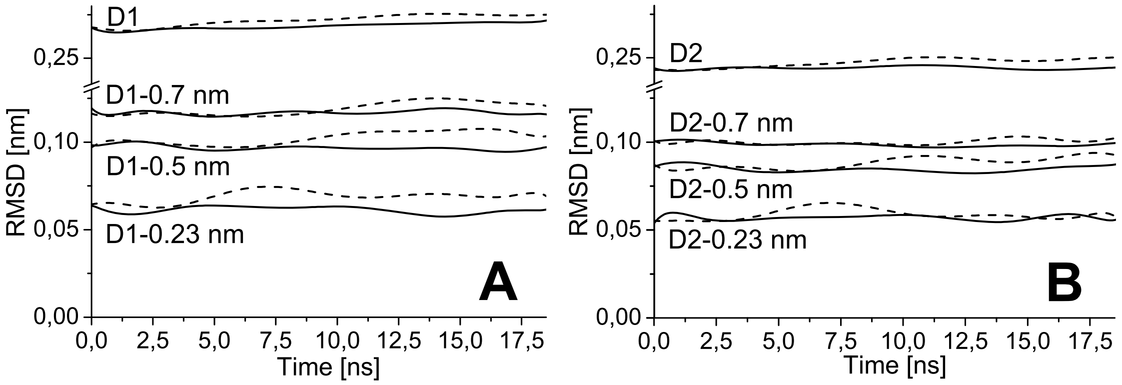

Figure C-8. Conformational analysis of Neutral-MD (solid lines) and Pheo$^-$-MD (dashed lines) simulations at 298 K performed on selected spherical protein layers of Eq-PSII RC model. (A) Root mean square deviations of alpha carbons (Cα RMSD) of the whole D1 protein subunit, Cα RMSD of D1 spherical layers that differ by increasing distance from Pheo-D1 head group (the first layer within 0.00-0.23 nm from Pheo-D1, the second layer within 0.23-0.5 nm, and the third layer within 0.50-0.70 nm). (B) Cα RMSD of D2 (D2 protein subunit), and alpha carbons of protein layers of D2 that differ by increasing distance from Pheo-D1 head group (layers defined analogous to A). For a better readability polynomial fit (of 9th order) was applied to all Cα RMSD. For more details on abbreviations and definition of selected protein layer see the text.

It is evident that the Cα RMSD of the protein is increasing with a distance from Pheo-D1 head group because of more flexible external protein parts, particularly in D1 protein subunit. Small conformational changes detected at 298 K for Neutral-MD result from thermal movements and those are given here as reference data. The shape of Cα RMSD plots obtained from 298 K Pheo$^-$-MD provide reasonable evidence, that equilibrated light-adapted Eq-PSII RC model has slightly changed its conformation within both D1 and D2 subunits particularly in proximity from reduced Pheo-D1.

We have also evaluated spatial orientation and positions of PSII RC pigments (Figure C-5) within MD simulations by a RMSD of N_A (on pyrrole ring I) and N_C (on pyrrole ring III) atom positions in chlorin pigments. The results from N_A-RMSD and N_C-RMSD analysis of a pigment part of light-adapted Eq-PSII RC model, obtained from Pheo$^-$-MD simulation at 298 K and 77 K are shown in the Figure C-9.

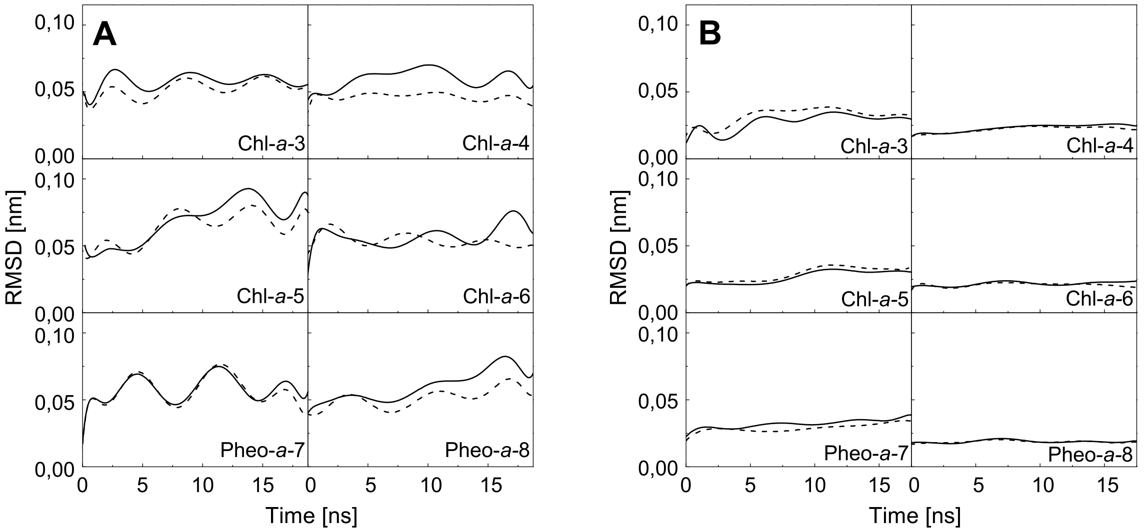

Figure C-9. N_A-RMSD (solid lines) and N_C-RMSD (dashed lines) of PSII RC pigments, obtained from Pheo$^-$-MD at 298 K (A) and at 77 K (B). For better readability polynomial fit (of 9th order) was applied to all N_A-RMSD and N_C-RMSD. In both plots the first column exhibits the results from a conformational analysis of the PSII RC pigments from the active branch and second column from the inactive branch, respectively. The abbreviations and more details are given in the text.

For all N_A-RMSD and N_C-RMSD calculations equilibrated geometry of PSII RC pigments of dark-adapted Eq-PSII RC model was used as a reference structure. Due to the 9th order polynomial fit applied to all RMSD graphs the zero values of all N_A-RMSD and N_C-RMSD at 0 ns could not be seen. The Figure C-9/A shows N_A-RMSD and N_C-RMSD plot at 298 K, and the Figure C-9/B at 77 K. The first column shows the results from the conformational analysis of a particular PSII RC pigments from active branch and second column from inactive branch, respectively. Values of N_A-RMSD and N_C-RMSD fluctuating around 0.05 nm could be assigned to thermal movements typical for these types of atoms at 298 K [Vasilev and Bruce 2006], however, changes in positions of PSII RC pigments have also been detected. Not surprisingly, major changes have been observed for PSII RC pigments from active branch at both temperatures.

Accessory chlorophyll Chl-*a*-5, which is the closest pigment to reduced Pheo-D1, exhibits the biggest change in its position during 298K-Pheo$^-$-MD. No substantial rotations of head groups of PSII RC pigments were observed except for peripheral Chl-*a*-9 (not shown). In the case of 77K-Pheo$^-$ MD, values of N_A-RMSD and N_C-RMSD fluctuating around 0.025 nm are typical for thermal movements of these types of atoms at 77 K. For illustration, Figure C-10 shows detected position change of PSII RC pigments and D1 protein environment surrounding PSII RC pigments of the active branch during 298K-Pheo$^-$-MD.

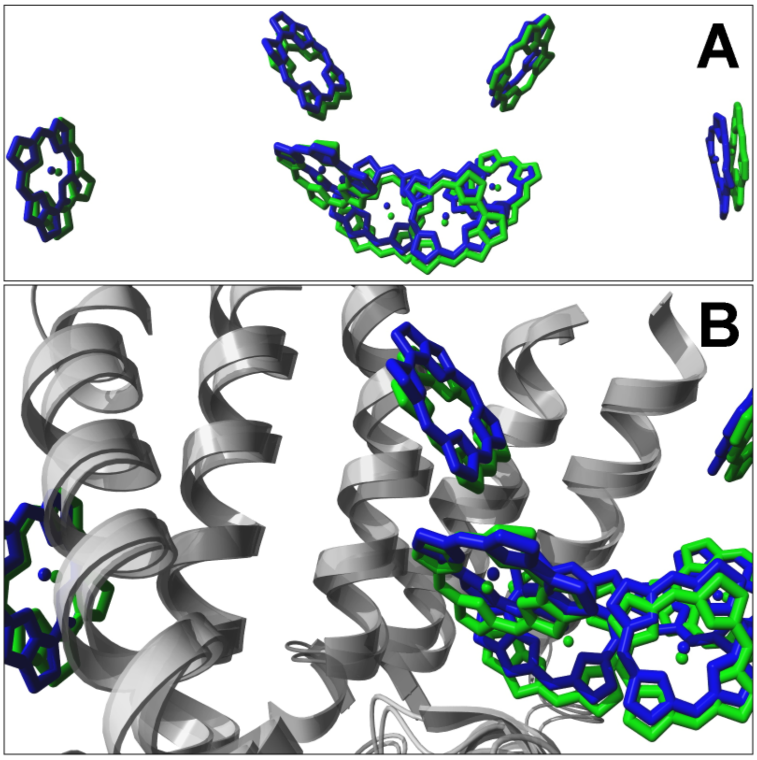

Figure C-10. Conformational change of pigment and protein environment in PSII RC upon Pheo-D1 reduction at 298 K. (A) Changes in positions of PSII RC pigments, (B) detailed insight in the vicinity of the active branch of PSII RC. Dynamic structures of PSII RC pigments colored in green were obtained from 298K-Neutral-MD and those colored in blue from 298K-Pheo$^-$-MD (developed after 8.2 ns simulation). Protein backbone of D1 subunits from both 298K-Neutral-MD and 298K-Pheo$^-$-MD simulations are shown as grey ribbons. Other PSII RC protein subunits are hidden and only chlorine head groups of PSII RC pigments are shown for clarity. The pigments are oriented analogous to Figure C-5.

The complete picture of changes in arrangement of PSII RC pigments detected at both temperatures (77 K and 298 K) as well as after Eq-PSII RC model preparation phase is given in the Figure C-11. Although, the changes in positions of some PSII RC pigments are of the same order for both temperatures and even after Eq-PSII RC model preparation phase, the resulting calculated difference (dark minus light adapted) absorption spectra revealed the significant ones.

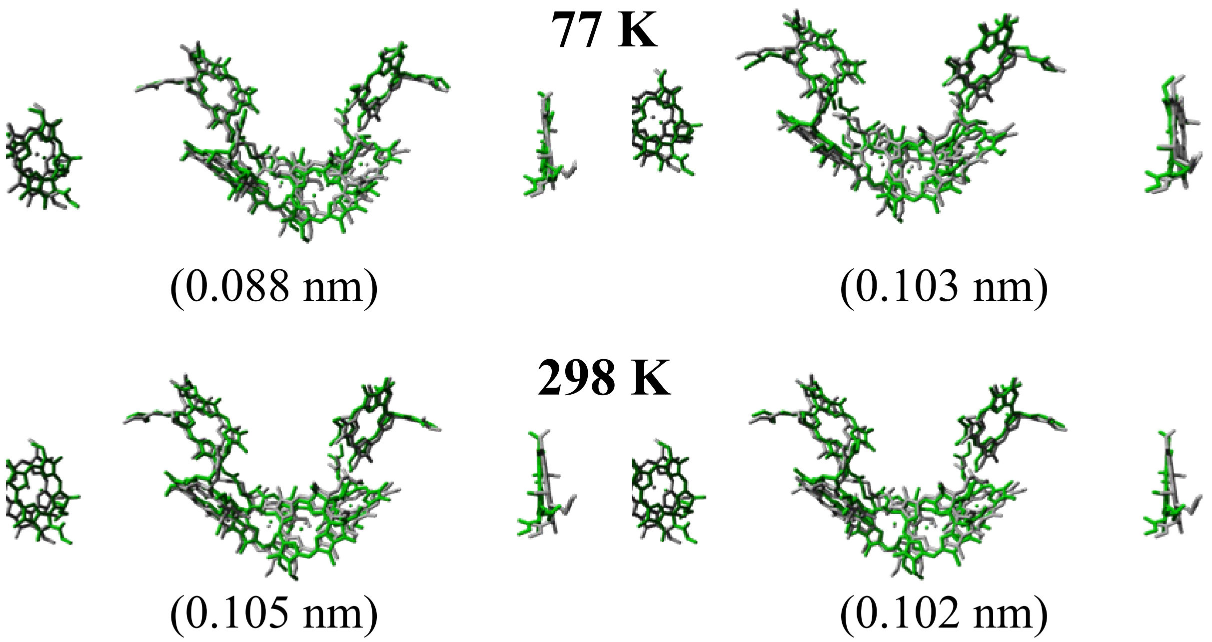

Figure C-11. Conformational change of PSII RC pigments after Eq-PSII RC preparation phase (green) at 77 K (top left) and at 298 K (bottom left) superposed with PSII RC pigments taken from crystal structure PDB ID 2AXT (gray). Conformational change of PSII RC pigments after 8.0 ns of 77K-Pheo$^-$-MD simulation (green) (top right) and after 8.0 ns of 298K-Pheo$^-$-MD simulation (green) (bottom right) superposed with PSII RC pigments from crystal structure PDB ID 2AXT (gray). Only macrocycle head groups of PSII RC pigments are shown for clarity. The pigments are oriented analogous to Figure C-5. The average values of N_A, N_B, N_C and N_D RMSD are given in brackets below each picture.

We have summarized the results presented in the Figure C-9 by calculating weighted average RMSD of PSII RC pigments at 298 K and at 77 K. First, an average value of N_A-RMSD and N_C-RMSD of six PSII RC pigments Chl-*a*-3, Chl-*a*-4, Chl-*a*-5, Chl-*a*-6, Pheoa-*a*-7 and Pheo-*a*-8 was calculated. Next, weighted average RMSD of peripheral chlorophylls Chl-*a*-9 and Chl-*a*-10 were calculated by using factor 0.5 to account for their smaller exciton coupling to the rest of the PSII RC pigments. Considering both average RMSD values final average value of RMSD of PSII RC pigments was obtained. In the case of 298K-Pheo$^-$-MD the biggest position change of PSII RC pigments was observed during the first 3 ns; after 8.2 ns the positions of the PSII RC pigments were stabilized and equilibrated system was established. The biggest position change of PSII RC pigments in the case of 77K-Pheo$^-$-MD was detected during the first 6.3 ns, and equilibrating the system after 11.4 ns. The average 77K-RMSD plot was of much lower magnitude when compared to the average 298K-RMSD plot and thus reduction of Pheo-D1 at 77 K did not affect significantly mutual positions and orientations of PSII RC pigments. 3D position change of PSII RC pigments and conformational change of protein part of PSII RC complex could be observed only in the case of 298K-Pheo$^-$-MD (Figure C-8 – C-11).

For a molecular structure viewing and rendering, protein solvation in periodic cell, MD simulations and MD trajectory analysis, RasMol [Sayle and Milner-White 1995], GROMACS [Lindahl et al. 2001], and YASARA (Yasara Biosciences, *http://www.yasara.org/index.html*;

Krieger et al. 2004) software packages were applied. MD simulations and QM calculations were carried on high-performance parallel computing cluster (Beowulf design).

C.1.4.2. Calculated and Experimental Optical Spectra

Optical spectra of PSII RC are sensitive to changes in mutual positions of transition dipole moments of the pigments. According to several previous studies, the vector of transition dipole moment of Q_y transition for Chl *a* and Pheo *a* pigments has approximately the same orientation as a vector connecting N_A to the N_C atom (Figure C-12).

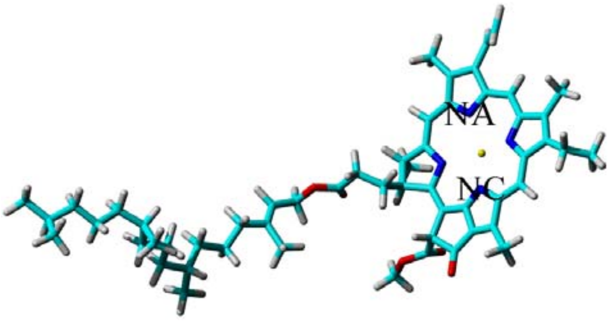

Figure C-12. The orientation of transition dipole moment in porphyrin-like pigments such as Chl *a*, Pheo *a* or BChl *a* is oriented approximately in the orientation of vector connecting $N_A \rightarrow N_C$ atoms.

The molecular coordinates of PSII RC pigments were taken by averaging coordinates extracted from MD snapshots in order to calculate dark-adapted and light-adapted absorption spectra. In the case of 298 K-light-adapted absorption spectrum 8.2 ns snapshot of 298K-Pheo$^-$-MD simulation was applied. For a 77 K-light-adapted absorption spectra 11.4 ns snapshot of 77K-Pheo$^-$-MD was used. In order to minimize thermal fluctuations of coordinates of PSII RC pigments, we have applied short energy minimization to the whole Eq-PSII RC complex.

In order to calculate optical spectra of PSII RC pigments we have developed scripts in MatLab (http://www.mathworks.com/products/matlab/requirements.html) according theory given in the *Methods* section of this thesis. More precisely, the non-diagonal Hamiltonian matrix elements (within transition monopole and dipole approximation), eigenvectors and eigenvalues were all calculated by our scripts developed for MatLab. Due to the presence of reduced Pheo-D1 in the light-adapted PSII RC models simulated by light-adapted Pheo$^-$-MD simulations, the site energies of the remaining PSII RC pigments are affected. Therefore electrochromic shifts in the monomer transition energies (site energies) of PSII RC pigments were calculated (Table C-14).

	298 K		**77 K**	
No.	ESP charges	Mulliken charges	ESP charges	Mulliken charges
1.	12.0	9.4	10.3	10.2
2.	67.6	64.9	70.4	66.3
3.	159.4	157.9	223.8	239.8
4.	-23.7	-22.9	-23.2	-21.9
5.	9.5	8.3	7.4	6.0
6.	21.5	18.3	22.8	23.3
7.	4.7	4.8	4.0	4.2

Table C-14. Electrochromic shifts of the monomer transition energies of PSII RC pigments for light-adapted PSII RC models (in cm^{-1}) simulated at 298 K and 77 K using ESP charges (left columns) and Mulliken charges (right columns). Monomer transition energies of PSII RC pigments for the Q_y transition were taken from recently published data [Raszewski et al. 2005].

Optical spectra presented in this thesis were calculated using transition dipole [Pearlstein 1991] and transition monopole method [Chang 1977] both described in the *Methods* section. The parameters used for the optical spectra calculations are as follows. For the Gaussian distribution of transition energies full-width at half-maximum (FWHM) of 210 cm^{-1} was used following previous finding [Prokhorenko and Holzwarth 2000; Jankowiak et al. 2002; Durrant et al. 1995]. A nondiagonal energetic disorder was omitted due to its negligible effect on the spectra [Pullerits 2000]. For dark-adapted PSII RC system (without charge separation on the pigments) the one-exciton Hamiltonian of eight chlorins was given by the matrix containing the 8 x 8 two-pigment coupling energies. The value of ε_{eff} = 1.5 was used in all calculations according to previous similar studies [Raszewski et al. 2005].

The transition dipole strengths of 23 and 14 $Debye^2$ for Chl *a* and Pheo *a* chromophores were used, respectively [Jankowiak et al. 2002; Durrant et al. 1995]. The calculated light-adapted stick absorption spectra of PSII RC pigments (Table C-15) were completed with Gaussian forms. Each of the envelopes has the FWHM of 150cm^{-1}, which roughly corresponds to the homogenous line-width of Chl *a* at room temperature [Konermann and Holzwarth 1996]. An ensemble averaging over 10.000 RC spectra generated the presented plots of oscillator strength against wavelength for the exciton states of PSII RC [Renger and Marcus 2002].

	298 K			77 K		
	without ES	with electrochromic shifts		without ES	with electrochromic shifts	
		ESP	Mulliken		ESP	Mulliken
No.	Old	charges	charges	Old	charges	charges
1.	654.1 (8.9)	652.6 (8.9)	652.7 (8.9)	654.2 (9.5)	652.5 (9.0)	652.6 (8.7)
2.	680.0 (48.4)	676.5 (51.6)	676.6 (51.9)	680.7 (54.4)	677.6 (52.8)	677.6 (52.2)
3.	676.4 (30.6)	674.5 (29.3)	674.6 (28.7)	676.8 (27.1)	674.7 (23.0)	674.7 (22.5)
4.	674.1 (4.9)	670.9 (6.0)	670.9 (6.0)	674.1 (3.2)	665.9 (24.3)	665.8 (23.5)
5.	668.1 (15.8)	666.0 (24.0)	666.2 (24.0)	668.0 (23.2)	666.4 (10.6)	666.2 (13.1)
6.	667.8 (19.3)	667.9 (14.0)	667.9 (13.3)	666.7 (11.2)	668.3 (6.3)	668.0 (3.4)
7.	667.0 (24.1)	667.7 (18.3)	667.7 (19.2)	667.0 (23.3)	667.8 (26.0)	667.8 (28.4)

Table C-15. Light-adapted stick absorption spectra of PSII RC pigments (in nm), calculated on selected Pheo$^-$-MD snapshots at 298 K and 77 K, with and without inclusion of electrochromic shifts in site energies of PSII RC pigments. Numbers in brackets give intensities of signals (in artificial units a.u.) (ES - abbreviate electrochromic shift; ESP - ElectroStatic Potential; Old - without electrochromic shifts)

The *Pij* quantities are defined as a second power of corresponding eigenvector U_{ij} (obtained by diagonalization of Frenkel Hamiltonian), and represent contribution of the ith pigment to the jth excitonic state (matrix of 8 x 8 *Pij* values for dark-adapted and 7 x 7 *Pij* values for light-adapted absorption spectra) (Table C-16). For light-adapted PSII RC pigments *Pij* values were calculated by considering electrochromic shifts.

Pij values for dark and light-adapted PSII RC pigments at 298 K

Dark-adapted ***Light-adapted: ESP charges*** ***Mulliken charges***

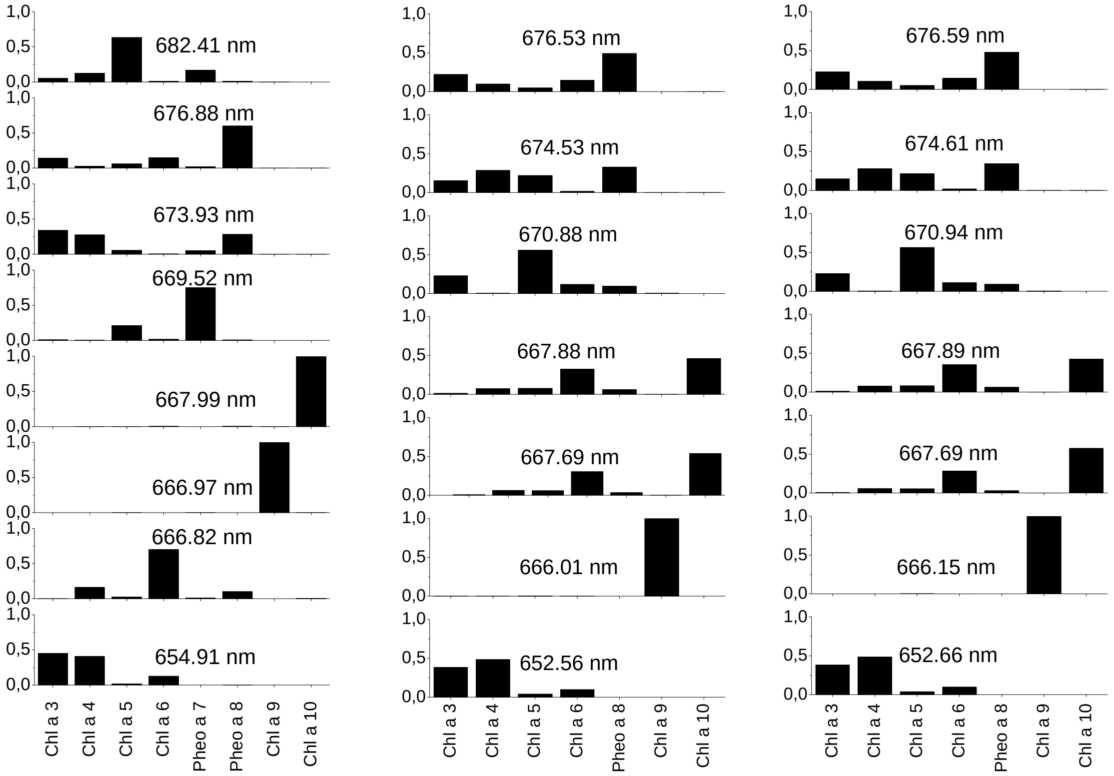

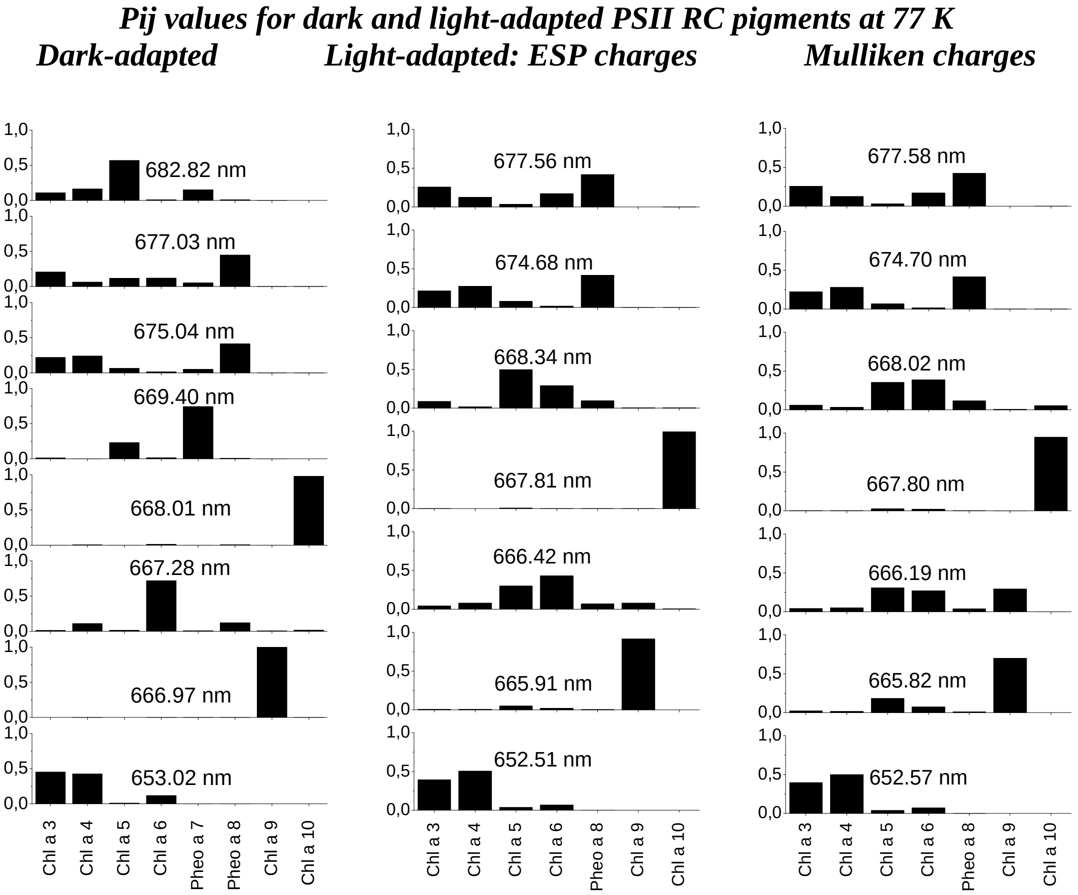

Table C-16. Light and dark-adapted Pij values for PSII RC pigments at 298 K (upper) and 77 K (lower).

Comparison of calculated dark-adapted absorption spectra from Neutral-MD and experimental dark-adapted absorption spectra of PSII RC [Vacha et al. 2005] is shown in the Figure C-13. Clearly, both calculated 298 K-plot and 77 K-plot share the same spectral features with both experimental analogues [Vacha et al. 2005].

The position of maximum peak of calculated 298 K-plot at 675.7 nm is almost identical with position of maximum peak of experimental 273 K-plot at 675.2 nm. The two peaks of calculated 77 K-plot at 671.5 nm and 678.6 nm are also in good accordance with peaks of experimental 77 K-plot at 672.0 nm and 678.5 nm. Small differences in shape of calculated and experimental dark-adapted absorption spectra are in slightly higher intensity of 77 K-graph maximum at 671.5 nm and small blue and red shifts of envelopes of both calculated graphs. We can state that positions and orientations of PSII RC pigments developed during Neutral-MD simulations at 298 K and 77 K were equilibrated and their dark-adapted absorption spectra were almost identical with their experimental analogues.

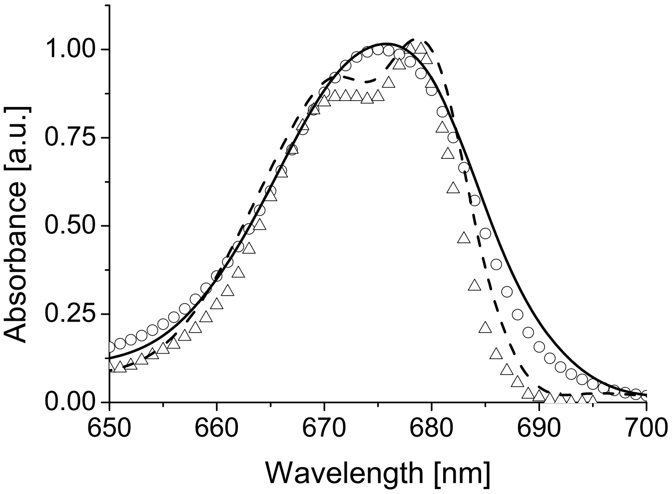

Figure C-13. Comparison of calculated dark-adapted absorption spectra of PSII RC pigments developed by Neutral-MD simulation at 298 K (solid line) and 77 K (dashed line) with experimental dark-adapted absorption spectra of PSII RC measured at 273 K (circles) and 77 K (triangles) [Vacha et al. 2005]. Only spectra calculated with inclusion of inhomogeneous broadening are shown for clarity. All spectra are normalized to their maxima using arbitrary units.

The difference absorption spectra of the PSII RC pigments developed from Neutral-MD and Pheo$^-$-MD at 298 K and 77 K were compared with the experimental difference absorption spectra of PSII RC measured at 277 K and 77 K [Vacha et al. 2002] (Figure C-14). A considerable bleaching of the absorption spectra observed experimentally at 277 K is comparable with our computed difference absorption spectra at 298 K.

The position of absorbance minimum peak of calculated 298 K spectrum at 681.9 nm is almost identical with those of experimental 277 K-graphs at 682.0 nm. Blue shoulder of calculated 298 K-graphs at 667.8 nm is slightly shifted from blue shoulder of experimental 277 K-graphs at 666.9 nm. Two peaks of calculated 77 K-graphs at 662.4 nm and 681.8 nm are in accordance with two peaks of experimental 77 K-graph at 666.7 nm and 682.1 nm, respectively. Differences in shape of calculated and experimental difference absorption spectra could be explained by limits of MD and also point-dipole approximation, which does not consider coupling of Q_y to higher excited states.

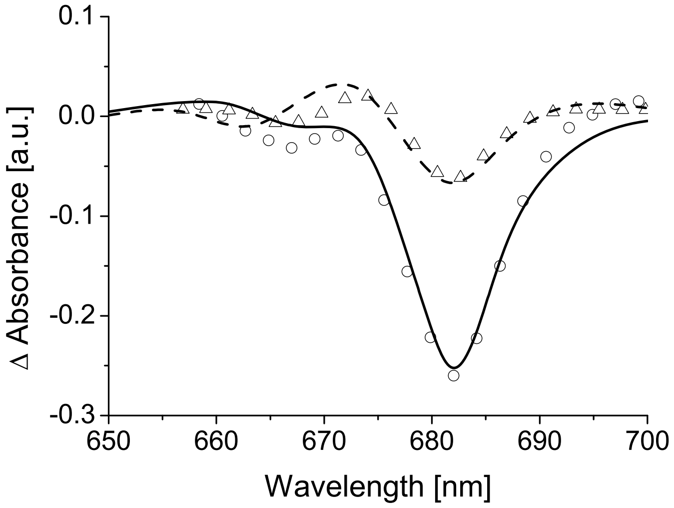

Figure C-14. Comparison of calculated difference (dark-adapted minus light-adapted) absorption spectra of PSII RC pigments (developed from Neutral-MD and Pheo$^-$-MD at 298 K (solid line) and at 77 K (dashed line)) with experimental difference absorption spectra of PSII RC measured at 277 K (circles) and 77 K (triangles) [Vacha et al. 2002]. Only spectra calculated with inclusion of inhomogeneous broadening and electrochromic shifts (applicable for light-adapted spectra) are shown for clarity. All spectra were normalized using arbitrary units, keeping the ratio between minimum peak of 298K-plot and minimum peak of 77K-plot.

C.1.5. Conclusions

Summarizing our results we may conclude, that conformational changes of PSII RC protein part upon reduction of Pheo-D1 were detected only in the case of high temperature dynamics, 298K-Pheo$^-$-MD. Changes in position and orientation of particular PSII RC pigments during 298K-Pheo$^-$-MD were also observed. The significant conformational changes have been detected only for interior parts of D1 protein in proximity to Pheo-D1. Spatial positions of the PSII RC pigments from the active D1 branch have been changed more then their symmetrically located PSII RC pigments from inactive branch within 298K-Pheo$^-$-MD and also 77K-Pheo$^-$-MD simulations.

The resulting absorption difference spectra of PSII RC models equilibrated at temperatures of 77 K and 298 K were highly consistent with our previous experiments in which the light-induced bleaching of PSII RC absorbance spectrum was observable only at 298 K. Since the temperature does not influence the excitonic interaction, the temperature dependence of the absorption spectra bleaching upon Pheo reduction does not support the model of Pheo-D1 excitonically interacting with the other chlorins of the PSII RC.

C.2. CHLOROSOMES

Chlorosomes are the biggest and the most efficient light harvesting antennae found in nature. In spite of intensive research devoted to this topic, only little is known about actual structure and organization of the main components, such as bacterio-chlorophylls (BChl), carotenes, lipids and partially some proteins, forming the inner space of chlorosomes (see also detail description in *Chlorosomes from Green Sulfur Bacteria* section of this thesis and references given therein). The well established rod-like model [Egawa et al. 2007] was put to doubts by recently published results by Pšenčík [Psencik et al. 2004], who proposed so-called lamellar model. We were asked to construct different types of lamellar models, by using experimental structural parameters and study structural self-organization of the main components, bacterio-chlorophyll *c* (BChl *c*; three-letter code BCC in our FF) and carotene chlorobactene (three-letter code CBE in our FF) of the chlorosomes. Well equilibrated models containing BChl *c* pigments and small moiety of chlorobactenes prepared by molecular modeling techniques could further serve as a replacement for missing crystal (or NMR) structure of chlorosome.

C.2.1. Force Field Development

Similarly to the *Photosystem II* project, new FF parameters for molecules that are not yet incorporated in the existing FFs [MacKerell et al. 1998; Jorgensen 1998; Cornell et al. 1995] had to be developed. Here we present only part of new developed AMBER-like FF parameters, particularly for BChl *c* and chlorobactene (the rest of new FF parameters are available in an electronic form). All new FF parameters were developed by *ab initio* (HF/6-31G*) quantum-chemical calculations in Gaussian 98 and implemented into YASARA package [Krieger et al. 2004]. From many other types of BChl *c* we have chosen the R_EM epimer (the most abundant type) for building our models. The symbol R stands for one of two strereoisomerizations, namely R and S, and EM abbreviates ethyl- and methyl- group attached to carbons highlighted in the Figure C-15. Pigment geometries were optimized by *ab intio* (HF/6-31G*) calculations.

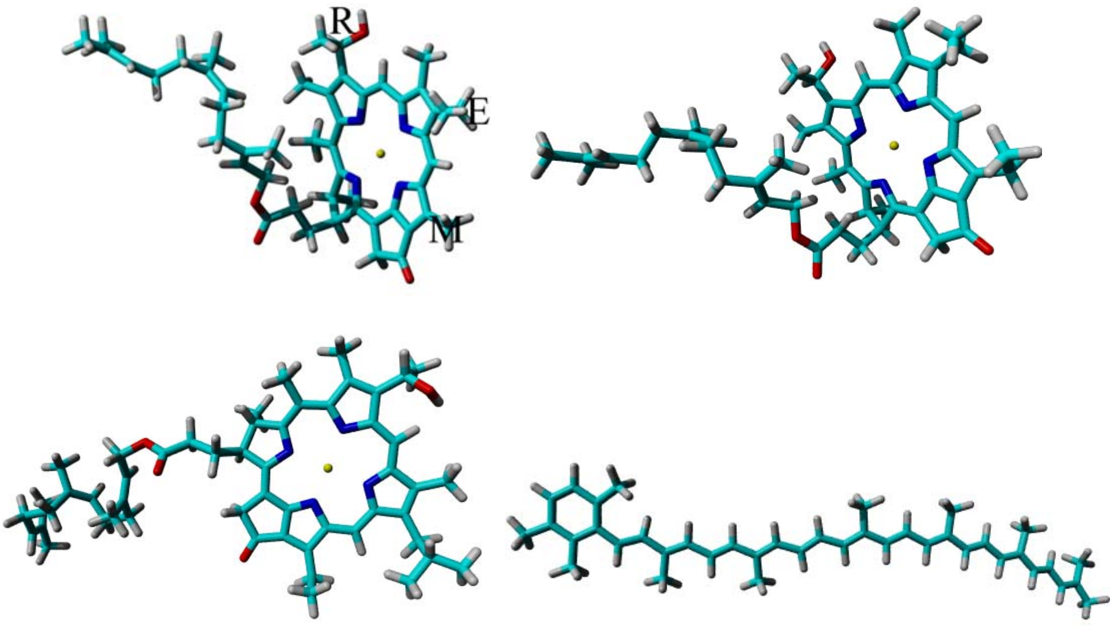

Figure C-15. Three types of BChl *c* molecules, namely BChl *c* R_EM epimer (top left), BChl *c* R_EE epimer (top right), BChl *c* S_IE epimer (bottom left) and chlorobactene (bottom right). Abbreviation R_EM stands for R stereoisomer and ethyl- methyl- epimer (S_IE stands for S stereoisomer and isopropyl- ethyl- epimer). Geometries of depicted pigments were optimized by *ab initio* (HF/6-31G*) calculations in Gaussian 98.

C.2.1.1. New Topology Files for Chlorosome Pigments

In the Table C-17 and Table C-18 topology files for chlorobactene and BChl *c* R_EM epimer, the most abundant pigment of inner part of chlorosomes, are shown respectively. In the tables, first column holds names of atoms (Figure C-29), second column shows subsistent atom types and in the third column newly developed atomic partial charges are given.

ChloroBactene ♦ CBE ♦ 0.0									
No.	Atom name	Atom type	RESP charge	Atom name	Atom type	RESP charge	Atom name	Atom type	RESP charge
1.	C1	cc	0.11	H34	HC	0.06	H27	ha	0.16
2.	C2	cd	0.09	H34	HC	0.06	C28	ce	0.01
3.	C3	cd	-0.25	H34	HC	0.06	H28	ha	0.14
4.	H3	ha	0.18	C12	ce	-0.34	C29	ce	-0.45
5.	C4	cc	-0.29	H12	ha	0.18	H29	ha	0.19
6.	H4	ha	0.17	C13	ce	0.22	C30	c2	0.31
7.	C5	cc	0.21	C14	cf	-0.30	C35	C6	-0.20
8.	C6	cd	-0.27	H14	ha	0.14	H35	HC	0.06
9.	C7	cf	0.14	C15	cf	-0.13	H35	HC	0.06
10.	H7	ha	0.08	H15	ha	0.18	H35	HC	0.06
11.	C8	ce	-0.36	C16	ce	-0.13	C36	C6	-0.20
12.	H8	ha	0.18	H16	ha	0.18	H36	HC	0.06
13.	C9	ce	0.18	C17	ce	-0.30	H36	HC	0.06
14.	C10	cf	-0.31	H17	ha	0.14	H36	HC	0.06
15.	H10	ha	0.16	C18	cf	0.22	C37	C6	-0.22
16.	C11	cf	-0.02	C19	cf	-0.35	H37	HC	0.07

17.	H11	ha	0.15	H19	ha	0.19	H37	HC	0.07
18.	C33	C6	-0.25	C20	ce	-0.02	H37	HC	0.07
19.	H33	HC	0.07	H20	ha	0.15	C38	C6	-0.20
20.	H33	HC	0.07	C21	ce	-0.31	H38	HC	0.06
21.	H33	HC	0.07	H21	ha	0.16	H38	HC	0.06
22.	C31	C6	-0.18	C22	cf	0.19	H38	HC	0.06
23.	H31	HC	0.06	C23	cf	-0.33	C39	C6	-0.37
24.	H31	HC	0.06	H23	ha	0.17	H39	HC	0.10
25.	H31	HC	0.06	C24	ce	-0.02	H39	HC	0.10
26.	C32	C6	-0.28	H24	ha	0.15	H39	HC	0.10
27.	H32	HC	0.09	C25	ce	-0.32	C40	C6	-0.37
28.	H32	HC	0.09	H25	ha	0.16	H40	HC	0.10
29.	H32	HC	0.09	C26	cf	0.17	H40	HC	0.10
30.	C34	C6	-0.19	C27	cf	-0.32	H40	HC	0.10

Table C-17. Topology file (without connectivities) for chlorobactene developed for AMBER-like FFs.

The atom types used for new topology files were adopted from existing set of GAFF AMBER FF atom types (GAFF abbreviates General AMBER Force Field) and original AMBER FF (release 2005) [Case et al. 2005; Cornell et al. 1995] atom types. For structurally similar parts between bacterial photosynthetic pigments [Ceccarelli et al. 2003] and their analogues found in bacterial light harvesting antennae existing FF parameters were also used. RESP atomic partial charges represent required quality for any AMBER-like FF and, thus, could be used elsewhere. Molecule full name, its three-letter code (in our FF) and overall charge is given in the header of the tables. For details on development of RESP atomic partial charges see [Wang et al. 2000; Bayly et al. 1993] and on new FF parameters development AMBER developing scheme [Cornell et al. 1995].

Bacterio-Chlorophyll *c* (R_EM - epimer) ♦ BCC ♦ 0.0									
No.	Atom name	Atom type	RESP charge	Atom name	Atom type	RESP charge	Atom name	Atom type	RESP charge
1.	MG	mg	1.17	CMH	C6	-0.22	C4	C6	-0.44
2.	NC	ns	-0.50	O1B	OH	-0.71	C9	C6	-0.34
3.	ND	nm	-0.48	HBB	HC	0.12	C14	C6	-0.39
4.	NA	ns	-0.55	HBB	HC	0.12	H1	h1	-0.03
5.	NB	nm	-0.61	HMB	HC	0.15	H1	h1	-0.03
6.	C1D	C%	-0.02	HMB	HC	0.15	H2	HA	0.19
7.	C2D	C8	0.19	HMB	HC	0.15	H5	HC	0.09
8.	C3D	C8	-0.30	HMA	HC	0.14	H5	HC	0.09
9.	C4D	C&	0.11	HMA	HC	0.14	H6	HC	0.10
10.	C1A	C$	0.03	HMA	HC	0.14	H6	HC	0.10
11.	C2A	C4	-0.14	HAA	HC	0.07	H7	HA	0.16
12.	C3A	C4	0.33	HAA	HC	0.07	H10	HC	0.02
13.	C4A	C$	0.10	HBA	HC	0.01	H10	HC	0.02
14.	C1B	C9	0.08	HBA	HC	0.01	H11	HC	0.05
15.	C2B	C8	0.23	HMD	HC	0.11	H11	HC	0.05
16.	C3B	C8	-0.09	HMD	HC	0.11	H12	HA	0.20
17.	C4B	C"	0.28	HMD	HC	0.11	H4	HC	0.13
18.	C1C	C"	0.16	HAC	HC	0.02	H4	HC	0.13
19.	C2C	C8	0.17	HBC	HC	0.05	H4	HC	0.13
20.	C3C	C8	-0.23	HBC	HC	0.05	H9	HC	0.10
21.	C4C	C9	0.12	HMC	HC	0.11	H9	HC	0.10
22.	CHD	C7	-0.12	HMC	HC	0.11	H9	HC	0.10
23.	CHC	C7	-0.31	HMC	HC	0.11	H14	HC	0.10

24.	CHB	C7	-0.01	H2A	HC	0.10	H14	HC	0.10
25.	CHA	C#	0.10	H3A	HC	0.01	H14	HC	0.10
26.	CAB	C5	0.28	CBD	C5	-0.37	HMH	HC	0.06
27.	CBB	C5	-0.46	CAD	C+	0.69	HMH	HC	0.06
28.	CMB	C6	-0.53	OBD	o1	-0.58	HMH	HC	0.06
29.	CMA	C6	-0.53	HBD	HC	0.12	H1B	HO	0.45
30.	CAA	C5	-0.16	C1	C5	0.52	HAB	h1	0.06
31.	CBA	C5	-0.03	C2	C~	-0.50	HBB	HC	0.12
32.	CGA	C!	0.84	C3	C`	0.27	HBD	HC	0.12
33.	O1A	o1	-0.61	C5	C5	-0.22	HAC	HC	0.02
34.	O2A	of	-0.54	C6	C5	-0.15	HBC	HC	0.05
35.	CMD	C6	-0.36	C7	C~	-0.26	C15	C6	-0.39
36.	CAC	C5	0.09	C8	C`	-0.01	H15	HC	0.10
37.	CBC	C6	-0.19	C10	C5	0.06	H15	HC	0.10
38.	CMC	C6	-0.40	C11	C5	0.09	H15	HC	0.10
39.	HHD	HA	0.19	C12	C~	-0.58			
40.	HHC	HA	0.22	C13	C`	0.36			

Table C-18. Topology file (without connectivities) for BChl *c* developed for AMBER-like FFs.

C.2.2. Equilibrated Models of Chlorosomes

Chlorosomes are extremely big light harvesting antennae, counting few hundred thousands of BChl molecules which are somehow “self”-organized forming big rods or lamellas attached together by some moiety of carotenes, lipids and proteins (mainly at the baseplate) or even by BChl molecules alone (see *Chlorosomes from Green Sulfur Bacteria* section of this thesis for more details). Due to the enormous size of chlorosomes there are no structures (crystal, NMR and other) available. The only structural data on the organization of the chlorosome are from various BChl aggregates studies by various techniques (NMR, cryo-electron microscopy, transient x-ray diffraction) [Psencik et al. 2004 and references therein]. It is, of course, not possible to build the whole chlorosome as a molecular model for theoretical studies, and only small fraction of the chlorosome can be constructed. Here we present six such truncated models for the inner organization of the chlorosomes prepared by molecular modeling techniques. Our models fulfill the experimental parameters obtained by Pšenčík [Psencik et al. 2004]. It should be noted here, that it is beyond the “limits” of any computational approach to build or calculate the precise organization of even small fractions of chlorosomes by any of the available techniques (*ab initio* or semi-empirical calculations or molecular modeling techniques). Thus, our models consist of “only” 80 molecules of BChl *c* (three models contain also four molecules of chlorobactene). However, from enough-long MD simulations (of an order of tens of nanoseconds) of carefully constructed BChl *c* models we could support some of the experimentally obtained structural parameters [Psencik et al. 2004] by performing various analyses.

C.2.2.1. Construction of Chlorosome Models

Starting structure for building of our chlorosome models was a monomer of BChl *c* molecule. The geometry of the BChl *c* monomer was optimized by high level *ab initio* (HF/6-31G*) quantum-chemical calculations in Gaussian 98. Further, parallel and antiparallel dimers were constructed (see *Chlorosomes from Green Sulfur Bacteria* section). The vertical distance between planes of BChl *c* monomers (more precisely between planes formed by macrocycle head groups of BChl *c* monomers) is thought to vary from 0.32 nm to maximal value of 0.45 nm. This wide range of values had to be evaluated as one of the critical parameter in our models. Therefore, separate models for different vertical distances, namely 0.35 nm, 0.37 nm, 0.40 nm, 0.42 nm and 0.45 nm, of BChl *c* planes had to be prepared. By term “BChl *c* plane” we understand plane of four BChl *c* molecules interacting through proposed hydrogen bonds (Figure C-16). Oxygen atoms O_{BD} and O_{1B} forming proposed hydrogen bonds are highlighted.

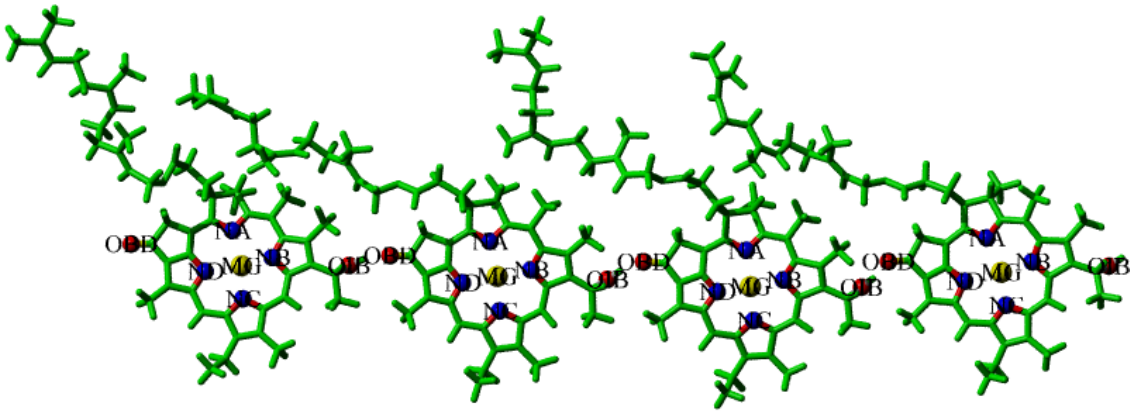

Figure C-16. Molecular model of BChl *c* plane (four molecules of BChl *c* in plane) shown as stick model. Atoms proposed to interact by hydrogen bonds and Coulomb interactions with another BChl *c* planes in lamellar BChl *c* models are shown as ball model in element colors (nitrogen in blue, oxygen in red, magnesium in yellow) with attached atom name labels. The picture was rendered in Pov-Ray and prepared in YASARA. Geometries of BChl *c* pigments shown here represent dynamic structures taken directly from MD simulation snapshot at 298 K, therefore thermal fluctuations are present.

The putative interactions between BChl *c* planes are shown in the Figure C-17. It has been proposed that hydrogen bonds are formed between O_{BD} and O_{1B} oxygens from the same BChl *c* plane (which we call favorable H-bonds) and also between O_{1B} oxygen and one of the nitrogens N_A, N_B, N_C or N_D from neighboring BChl *c* plane (which we call unfavorable H-bonds). Another proposed interaction between BChl *c* planes is Coulomb electrostatic interaction between magnesium atom from one BChl *c* plane and O_{1B} oxygen from neighboring BChl *c* plane.

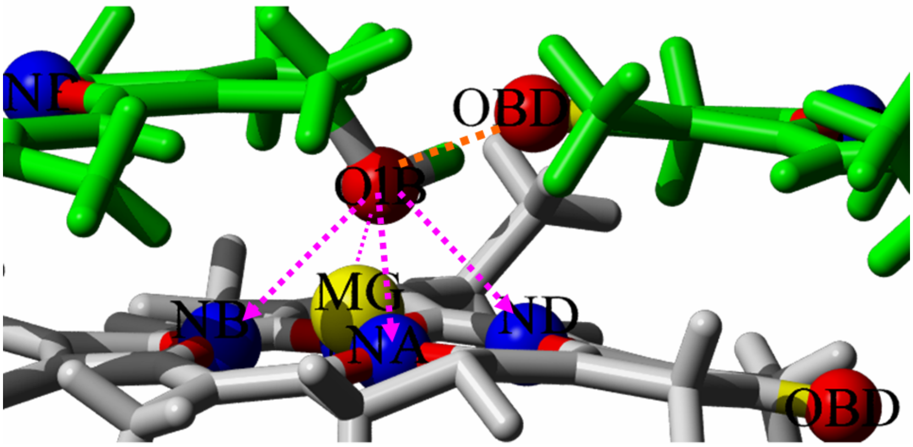

Figure C-17. Detail on putative interactions between BChl *c* molecules (shown as stick models) from one BChl *c* plane (green) and between two BChl *c* planes (green and gray). In the picture "favorable" hydrogen bond between O_{BD} and O_{1B} is shown as orange dashed line while four "unfavorable" hydrogen bonds between O_{BD} and four nitrogen atoms N_A, N_B, N_C or N_D from neighboring BChl *c* plane (gray) are shown as magenta dashed arrows. Proposed Coulomb electrostatic interaction between O_{1B} and Mg is not explicitly marked. The picture was rendered in Pov-Ray and prepared in YASARA. The geometries of the BChl *c* pigments are taken directly from MD simulation snapshot at 298 K, therefore thermal fluctuations are present.

For a better illustration two more pictures of two BChl *c* planes taken from antiparallel BChl *c* models are shown in the Figure C-18.

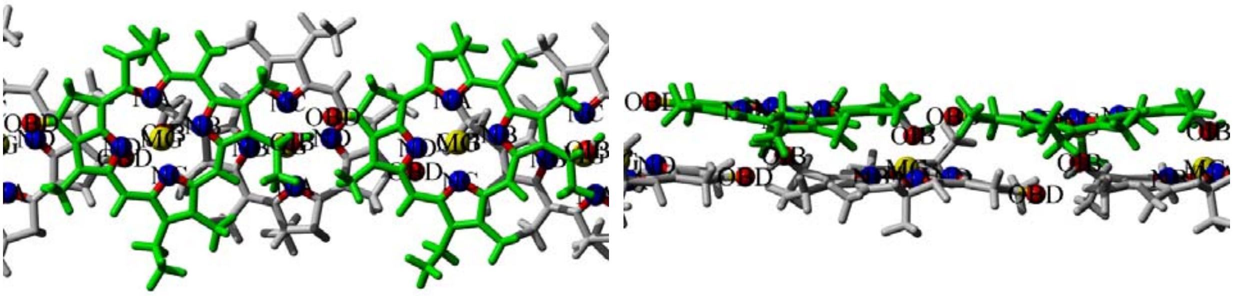

Figure C-18. Top (left) and side (right) detail view on two BChl *c* planes (green and gray), taken from antiparallel BChl *c* model, with vertical distance of BChl *c* planes 0.37 nm. For clarity only two BChl *c* molecules are shown from the upper BChl *c* plane (green) and three from the lower BChl *c* plane (gray). Farnesol tails and a short part of the side chain to which they are attached are also hidden. Geometries of BChl *c* pigments represent dynamic structures obtained from MD simulations.

Considering five values of vertical distance of BChl *c* planes, together ten models were prepared; five models constructed from parallel dimers and five models from antiparallel dimers. After energy minimization and 2 ns of MD simulation in YASARA, analysis of binding energy between BChl c planes was done. Details on preparation of equilibrated BChl *c* models and parameters from MD simulations are given in the following section. The results unambiguously showed that models with vertical distances of BChl *c* planes 0.37 nm and 0.40 nm are the most energetically favorable (Figure C-19).

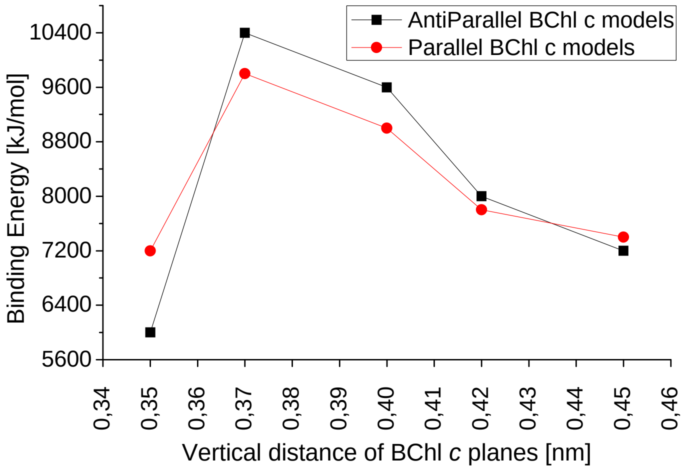

Figure C-19. The binding energy between BChl *c* planes (formed by four BChl *c* molecules in plane) of antiparallel BChl *c* models and parallel BChl *c* models versus vertical distance of BChl *c* planes, obtained by analysis of short (2 ns) MD simulations performed in YASARA. In the graph the more positive value of binding energy the stronger is the interaction between neighboring BChl *c* planes.

For our further studies only models with these particular distances were used. While for determination of the most appropriate value of vertical distance of BChl *c* planes we considered only BChl *c* molecules as the only one building block, for further studies also models including chlorobactene molecules were prepared.

C.2.2.2. Details on Preparation of Equilibrated BChl c Models

In this separated section we will describe details on preparation of eight final equilibrated BChl *c* models, namely four 0.37 nm BChl *c* models and four 0.40 nm BChl *c* models. The same procedure was also applied for preparation of first set (together ten) of BChl *c* models constructed in order to elucidate the most probable vertical distance of BChl *c* models. Therefore from these ten BChl *c* models we could use two for further studies, namely one antiparallel BChl *c* model with vertical distance of BChl *c* planes 0.37 nm (abbreviaton 0.37 nm AntiParallel is used further) and one parallel BChl *c* model with vertical distance of BChl *c* planes 0.40 nm (abbreviaton 0.40 nm Parallel is used further). Another six BChl *c* models had to be prepared in the next step, namely 0.37 nm AntiParallel CBE model (CBE abbreviates presence of four chlorobactene molecules), 0.37 nm Parallel, 0.37 nm Parallel CBE and 0.40 nm AntiParallel CBE, 0.40 nm Parallel and 0.40 nm Parallel CBE model.

As mentioned above for preparation of equilibrated BChl *c* models we used optimized monomers of BChl *c* molecules. Antiparallel and parallel dimers were constructed with respect to proposed Coulomb electrostatic interaction between O_{1B} and Mg (Figure C-17) and vertical distance of BChl *c* planes. BChl *c* dimers were then four times copied and carefully placed to form two planar BChl *c* planes (Figure C-18) fulfilling existence of "favorable" hydrogen bonds between O_{BD} and O_{1B} oxygens (Figure C-17). One lamella was prepared from five copies of thus prepared BChl *c* planes. Second lamella was carefully positioned to minimize possible atom overlaps and to keep distance between lamellae determined at ~ 2.09 nm. All structural parameters (a = 0.96 nm, b = 1.20 nm and c = 2.09 nm) described by Pšenčík [Psencik et al. 2004] were thus fulfilled. Together 80 BChl *c* molecules formed two lamellae of all BChl *c* models (plus four molecules of chlorobactenes in the BChl *c* CBE models).

In the last step, geometry optimization of thus prepared BChl *c* models took place. Each of the eight BChl *c* models was treated separately. For simplification we will describe the equilibration process for 0.37 nm AntiParallel CBE model. The equilibration of other models was done in the same way. The 0.37 nm AntiParallel BChl *c* model was put into periodic simulation cell with dimensions ensuring appropriate formation of all proposed interactions (Figure C-17) also at the cell edges. Possible atom overlaps were eliminated by steepest descent minimization keeping coordinates of four nitrogen atoms N_a, N_B, N_C and N_D fixed in their starting positions. Four chlorobactene molecules were inserted vertically into model filling up relatively free space between two lamellae in close contact with farnesol tails of BChl *c* molecules. Further energy minimization was needed for elimination of atom overlaps. Simulated annealing with starting temperature 100 K and small step 0.1 K decreasing starting temperature was applied. Geometry optimization was performed by MD simulation with small time step 0.5 fs and temperature 298 K. After ~2 ns of energy minimization and geometry optimization (when there was no change in RMSD of heavy atoms from macrocycle head groups of BChl *c* pigments) positions of all nitrogen atom were released and further geometry optimization of the whole model was performed. Temperature was raised to 298 K and MD snapshots were saved after each 10 ps of MD simulation. NVT ensemble was used during the whole energy minimization, geometry optimization process and MD simulations. Time step 1.0 fs for intra-molecular interactions and 2.0 fs for inter-molecular interactions was used (see YASARA documentation for more details). Cutoff 1.0 nm was used for Lennard-Jones and electrostatic interactions. To treat the long-range electrostatic interactions outside the cutoff region the Particle Mesh Ewald method [Essmann et al. 1995] with a grid spacing < 0.1 nm, 4th order B-splines and a tolerance of 10^{-4} for the direct space sum were used. The temperature was adjusted by Berendsen thermostat [Berendsen et al. 1984] based on the time-averaged temperature. Construction of all BChl *c* models, steps for equilibration and MD simulations were performed in YASARA. MD trajectories of 30 ns duration were obtained. For analyses part 5 ns - 30 ns of MD trajectories was used. For illustration comparison of 0.37 nm

AntiParallel CBE model and 0.37 nm Parallel CBE model rendered from randomly selected MD snapshots is shown in the Figure C-20. BChl *c* molecules and chlorobactenes are shown as space filling model, which has an advantage for representation of real free van der Waals volume (in nm^3) in the simulation cell. However, due to relatively high density of the content of the simulation cell, only six BChl *c* planes (instead of ten) in each of the lamella are shown. The parameter free van der Waals volume was also one of the key parameters analyzed from MD trajectories. The bigger is this parameter the higher is the probability that some moiety of carotenes or lipids are together packed with majority of BChl *c* molecules to form stable structures of lamellae (or rods).

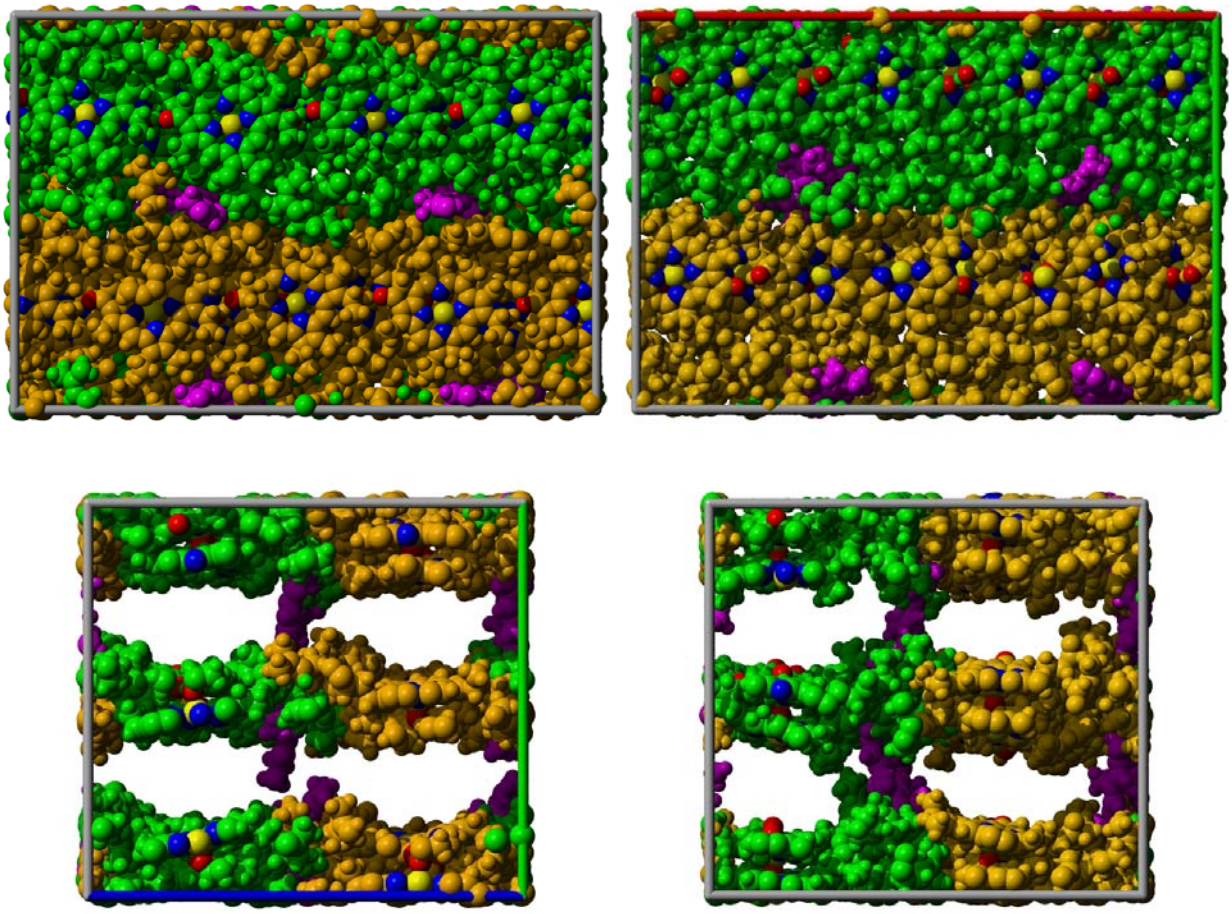

Figure C-20. Comparison of 0.37 nm AntiParallel CBE model (top left - top view; bottom left - side view) and 0.37 nm Parallel CBE model (top right - top view; bottom right - side view) shown as space filling model. For clarity only six BChl *c* planes (from ten BChl *c* planes) are shown in each of the two lamellae (green and orange). Molecules of chlorobactenes are shown in magenta, nitrogen atoms N_A, N_B, N_C and N_D in blue, magnesium atom in yellow and O_{BD} oxygen in red. Pictures were rendered in Pov-Ray from randomly selected MD snapshots.

C.2.3. Analysis of MD Trajectories

In the following section we will present results from five different analyses of MD trajectories obtained by MD simulations in YASARA. During relatively long, 30 ns, time period BChl *c* molecules together with chlorobactenes were able to find the local potential energy minima by proposed “self”-organization. However, we shall point out, that no dramatic changes in their starting arrangement can be expected from MD simulations in a ns time scale. Only equilibration processes of experimentally obtained structural parameters of proposed lamellar organization of BChl *c* pigments could be followed and analyzed. Additionally to the interactions shown in the Figure C-17 also free van der Waals (vdW) volume was tracked during performed MD simulations and results from 5 - 30 ns part (omitting equilibration 5 ns-long phase) are shown in the Figure C-21. Five parameters, namely Free van der Waals Volume, Hydrogen Bonds to Nitrogens N_A, N_B, N_C and N_D (unfavorable H-bonds), Hydrogen Bonds to Oxygen O_{BD} (favorable H-bonds), Coulomb Interactions to Mg and Binding Energy can be discussed. Note that maximal number of favorable H-bonds, unfavorable H-bonds and Coulomb interactions to Mg is 80 (due to 80 BChl *c* molecules in our models).

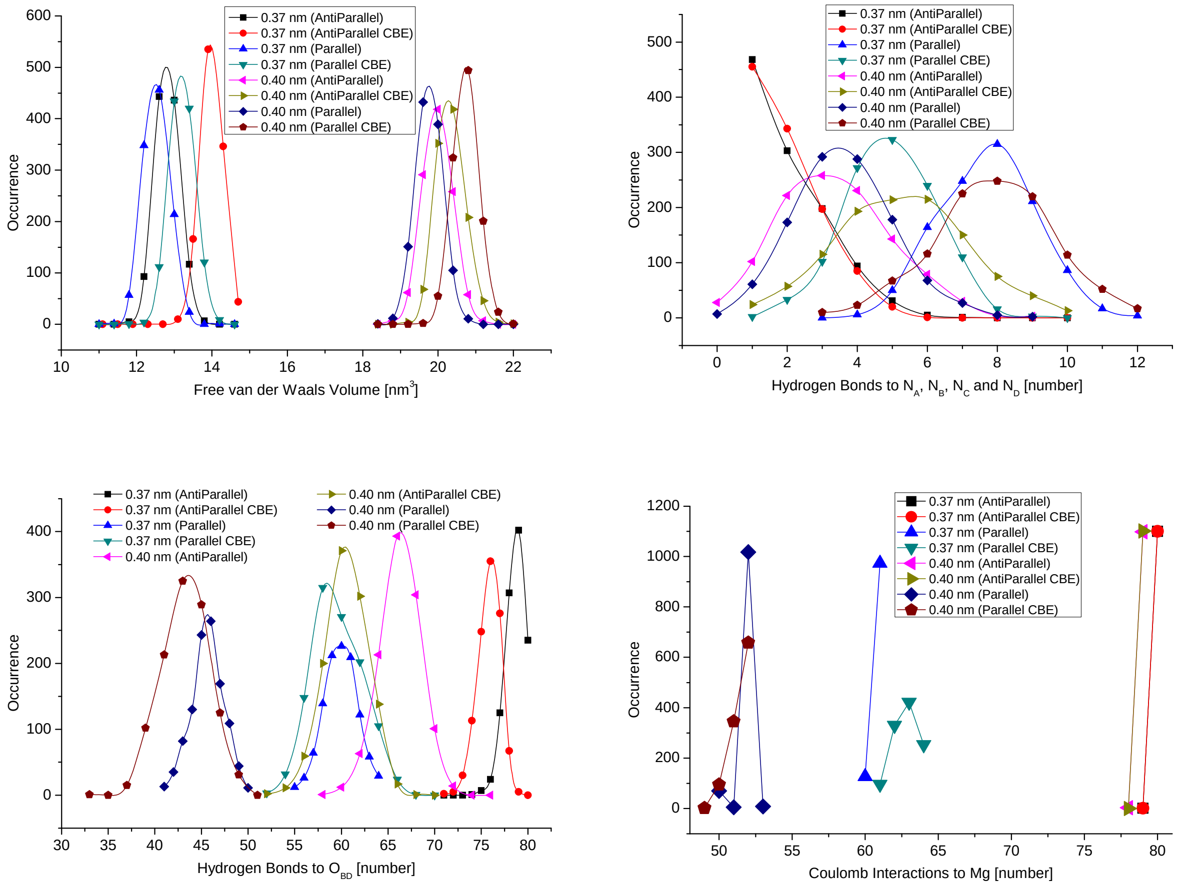

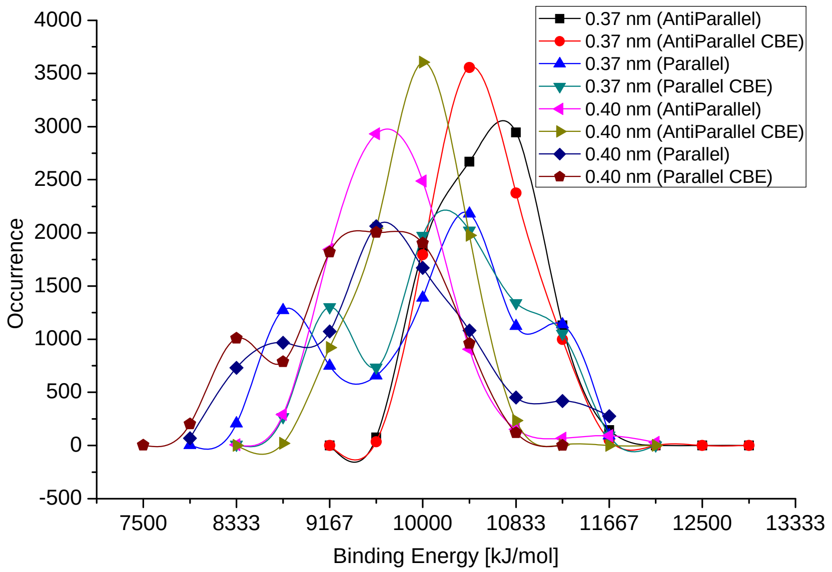

Figure C-21. Histograms for five parameters tracked during MD simulations (at 298 K; performed in YASARA) of eight lamellar BChl *c* models (abbreviations given in the legends) constructed in accordance with experimental structural data published recently [Psencik et al. 2004]. See the text for details.

The results are presented in the form of histograms. The x-axis holds all possible values that have been found in the MD snapshots. However, the range of the values for binding energy and free van der Waals volume is too large, and values had to be clustered into ten groups. The y-axis shows the occurrences for groups (e.g. fourteen groups for binding energy) shown on x-axis. For better readability discrete values (each marked by symbol) of each BChl *c* model were connected by spline line. The binding energy between BChl *c* planes was calculated using advanced analysis tools in YASARA (Figure C-22).

```
# The scene MyComplex must contain receptor and ligand as objects 1 and 2
# The structures must be energy minimized before Ebind calculation
EnergyUnit kJ/mol
LoadSce MyComplex
# Make sure that no water is present, we are using implicit solvent
DelRes HOH
ForceField AMBER99
# Choose a large cell, so that periodic boundaries have no impact on energies
Cell 100,100,100
Boundary periodic
# Calculate potential and solvation energy of the complex
epotcomp=Energy
esolcomp=SolvEnergy
# Add van der Waals solvation energy (empirical formula from
# ‘Computational Medicinal Chemistry for Drug Discovery‘, page 271)
surfacc=Surf Accessible
esolcomp=esolcomp+surfacc*0.005+0.85
# Calculate potential and solvation energy for each of the two
for i=1 to 2
RemoveObj not (i)
epot(i)=Energy
esol(i)=SolvEnergy
```

```
surfacc=Surf Accessible
esol(i)=esol(i)+surfacc*0.005+0.85
AddObj all
# Calculate result: energy of separated compounds - energy of complex
ebind=(epot1+epot2+esol1+esol2)-(epotcomp+esolcomp)
print ‘Binding energy is (ebind)‘
```

Figure C-22. Text of analysis macro developed for YASARA for binding energy calculation. The detail description of the commands used here is given in the manual pages (www.yasara.org) of YASARA.

All other parameters were also calculated by macros developed for YASARA and are freely available in the electronic form.

C.2.3.1. Notes on Obtained Results

From the analysis of free vdW volume two separate conclusions, one for 0.37 nm models and one for 0.40 nm models have to be made. Not surprisingly, values for 0.40 nm models are about 7 nm^3 higher due to bigger vertical distances between BChl *c* planes. The values of free vdW volume for models containing chlorobactene molecules are, of course, the biggest due to presence of chlorobactene molecules that create more free vdW space between BChl *c* lamellae and automatically increase the value of free vdW volume. In the case of 0.37 nm models, evidently more free vdW volume was observed for antiparallel models. In the case of 0.40 nm models no such conclusion could be made. Not negligible free vdW volume was detected during our 30 ns-long MD simulations for all BChl *c* models. Therefore, it seems that models prepared from antiparallel or parallel BChl *c* dimers do not fill up completely the inner space of chlorosomes and could accommodate some minor moiety of other molecules, such as carotenes, lipids or proteins, which is consistent with experimental data [Psencik et al. 2004 and references therein].

Results from analysis of number of unfavorable H-bonds created during our MD simulations positively revealed structural differences between antiparallel and parallel BChl *c* models. While in the case of antiparallel models the highest average number of unfavorable H-bonds was around 5, the average number of unfavorable H-bonds created during MD simulations for all parallel models was between 4 and 8. Interestingly, except for 0.37 nm Parallel models, presence of chlorobactene molecules in the models resulted in notable increase of number of unfavorable H-bonds. However, we may conclude that number of unfavorable H-bonds created during MD simulations was rather small for all BChl *c* models, thus their existence in lamellar models was put to doubts.

There are two major trends in the number of favorable H-bonds created during MD simulations. The presence of chlorobactene molecules in all BChl *c* models resulted in decrease of number of favorable H-bonds. Practically, all antiparallel models exhibited higher number of favorable H-bonds over the parallel models. The longer vertical distance of BChl *c* planes (0.40 nm) negatively influenced the number of favorable H-bonds. The relevance of favorable H-bonds was put to doubts in the case of parallel BChl *c* models, while in the case of antiparallel models their existence was clearly confirmed, with exception for 0.40 nm AntiParallel CBE model. In general, we may conclude that favorable H-bonds were present more or less in all eight lamellar BChl *c* models.

All possible Coulomb electrostatic interactions between central magnesium cation and O_{1B} oxygen from closest BChl *c* plane were created in all antiparallel BChl *c* models, with very small effect of vertical distance of BChl *c* planes and no effect of present chlorobactenes. In the case of parallel models positive effect on number of these interactions were observed for 0.37 nm models over 0.40 nm models. In general, existence of these interactions was clearly confirmed for all lamellar BChl *c* models.

Certainly, the most important parameter obtained from our MD simulations is binding energy between BChl *c* planes. By definition the more positive value the more energetically favorable is the BChl *c* model. This parameter was also used as a main criterion for accepting or rejecting the early prepared ten BChl *c* models (see *Construction of Chlorosome models* section for more details) constructed in order to elucidate the most appropriate vertical distance of BChl *c* models (Figure C-19). Clearly, all antiparallel models were energetically more favorable over parallel BChl *c* models, with exception for 0.40 nm AntiParallel model. Interestingly, for less dense 0.40 nm models positive effect of present chlorobactene molecules on binding energy was detected. The presence of chlorobactenes in vertical direction to the BChl *c* planes in our models had no or slightly positive effect on binding energy. Therefore, we may conclude that chlorobactene should be considered as one of the component of lamellar BChl *c* models, however we cannot exclude the possibility that it might be oriented in different manner. Further research should be addressed to put more light onto all possible orientations of chlorobactene molecules and their effect on binding energy.

C.2.4. Conclusions

We have constructed eight lamellar BChl *c* models in accordance with recently published data [Psencik et al. 2004]. The most energetically favorable vertical distances, 0.37 nm and 0.40 nm, of BChl *c* planes were found. By comparison of five parameters (see *Notes on Obtained Results* section) obtained from analysis of our 30 ns-long MD simulations we were able to describe relevance of slightly different structural parameters of antiparallel and parallel BChl *c* models and their most probable time-averaged values (Figure C-21). Antiparallel BChl *c* models showed much higher relevance over parallel BChl *c* models in the sense of all parameters analyzed here. The proposed positive effect of chlorobactene molecules on the stability of the BChl *c* models was observed as very little or none. Further theoretical studies had to done in order to explain the role of chlorobactenes or different molecules such as lipids and proteins in the inner part of chlorosomes. Finally, we conclude that antiparallel BChl *c* dimers should be considered as the main building block for construction of chlorosome lamellar models proposed by Pšenčík [Psencik et al. 2004].

C.3. FLAVOPROTEIN WrbA

C.3.1. Force Field Development

WrbA is a tetrameric protein with one molecule of flavinmononucleotide (FMN) cofactor per each monomer. During the process called “ping-pong” mechanism FMN molecule changes its oxidation state from fully oxidized state to double-reduced state. New FF parameters had to be developed for both forms of FMN in order to perform MD simulations. In the Table C-19 and Table C-20 new topology files for oxidized FMN cofactor and double-reduced FMN are given, respectively. In the tables, first column holds names of atoms taken from PDB files (Figure C-29), second column shows subsistent atom types and in the third column newly developed atomic partial charges are given. All new FF parameters represent required quality suitable for any AMBER-like FF. Atom types presented here were adopted from GAFF (see AMBER documentation for more details).

Flavin-MonoNucleotide (Oxidized) ♦ FMS ♦ -2.0

No.	Atom name	Atom type	RESP charge	Atom name	Atom type	RESP charge	Atom name	Atom type	RESP charge
1.	N1	nc	-0.78	C8	ca	0.18	C3*	c3	0.02
2.	C2	c	0.99	C8M	c3	-0.18	H3*	h1	0.06
3.	O2	o	-0.68	H8M	hc	0.07	O3*	oh	-0.68
4.	N3	na	-0.78	H8M	hc	0.07	HO3*	ho	0.45
5.	H3	hn	0.38	H8M	hc	0.07	C4*	c3	0.36
6.	C4	c	0.73	C9	ca	-0.40	H4*	h1	-0.04
7.	O4	o	-0.62	H9	ha	0.32	O4*	oh	-0.72
8.	C4A	cd	0.19	C9A	ca	-0.02	HO4*	ho	0.44
9.	N5	nc	-0.56	N10	na	-0.06	C5*	c3	0.14
10.	C5A	ca	0.47	C10	cd	0.44	H5*	h1	-0.02
11.	C6	ca	-0.45	C1*	c3	-0.07	H5*	h1	-0.02
12.	H6	ha	0.20	H1*	h1	0.09	O5*	os	-0.55
13.	C7	ca	0.13	H1*	h1	0.09	P	p5	1.34
14.	C7M	c3	-0.29	C2*	c3	0.26	O1P	o	-0.88
15.	H7M	hc	0.07	H2*	h1	0.19	O2P	o	-0.88
16.	H7M	hc	0.07	O2*	oh	-0.77	O3P	o	-0.88
17.	H7M	hc	0.07	HO2*	ho	0.43			

Table C-19. Topology file (without connectivities) for oxidized FMN developed for AMBER-like FFs. Note, the overall charge -2 due to the presence of phosphate group at the ribose tail of FMN.

Flavin-MonoNucleotide (Double-Reduced) ♦ FMR ♦ -2.0									
No.	Atom name	Atom type	RESP charge	Atom name	Atom type	RESP charge	Atom name	Atom type	RESP charge
1.	O1P	o	-0.83	O2*	oh	-0.77	H7M	hc	0.07
2.	P	p5	1.33	HO2*	ho	0.45	C5A	ca	0.37
3.	O2P	o	-0.83	C1*	c3	-0.31	C6	ca	-0.48
4.	O3P	o	-0.83	H1*	h1	0.13	H6	ha	0.20
5.	O5*	os	-0.59	H1*	h1	0.13	C10	cc	0.20
6.	C5*	c3	0.22	N10	nh	0.07	C4A	cd	-0.11
7.	H5*	h1	0.01	C9A	ca	-0.06	N5	nh	-0.73
8.	H5*	h1	0.01	C9	ca	-0.29	H5	hn	0.39
9.	C4*	c3	0.17	H9	ha	0.26	C4	c	0.73
10.	H4*	h1	0.06	C8	ca	0.05	O4	o	-0.66
11.	O4*	oh	-0.83	C8M	c3	-0.04	N3	na	-0.69
12.	HO4*	ho	0.47	H8M	hc	0.03	H3	hn	0.37
13.	C3*	c3	0.33	H8M	hc	0.03	C2	c	0.79
14.	H3*	h1	-0.06	H8M	hc	0.03	N1	na	-0.42
15.	O3*	oh	-0.93	C7	ca	0.14	H1	hn	0.33
16.	HO3*	ho	0.53	C7M	c3	-0.30	O2	o	-0.65
17.	C2*	c3	0.40	H7M	hc	0.07			
18.	H2*	h1	-0.04	H7M	hc	0.07			

Table C-20. Topology file (without connectivities) for double-reduced FMN developed for AMBER-like FFs.

Atom names were adopted from recently published crystal structure of WrbA and complexes with flavin mononucleotide [Gorman and Shapiro 2005]. The format chosen for labeling of particular atoms is somehow confusing (some atom names contain standard three-letter code plus asterisk sign). Therefore, we present developed RESP atomic partial charges also in the graphical form for heavy atoms of both forms of FMN in the Figure C-23.

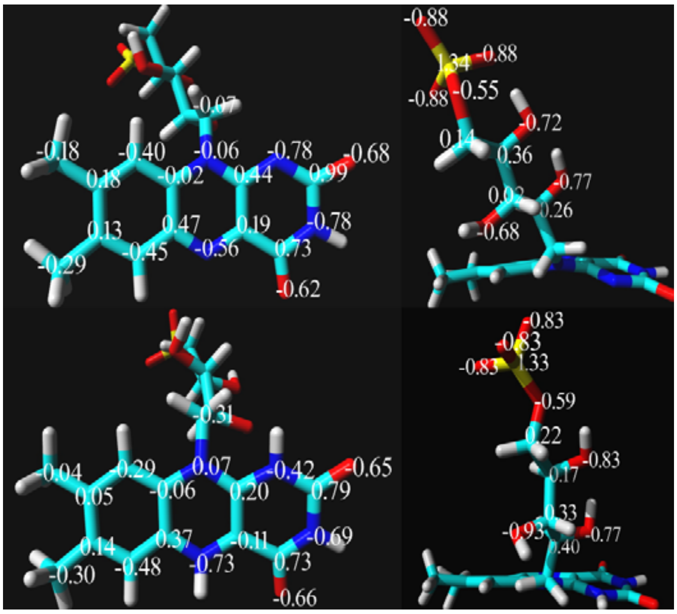

Figure C-23. Graphical representation of new RESP atomic partial charges developed for oxidized (top) and double-reduced (bottom) form of FMN obtained by *ab initio* (HF/6-31G*) quantum-chemical calculations in Gaussian 98. The RESP charges are given only for heavy atoms for clarity. The geometries of FMN molecules shown here are only schematic. The RESP charges for heavy atoms from isoalloxazine ring (left) and ribose tail and phosphate group (right) of both forms of FMN are given.

C.3.1.1. Elucidation of Planarity of FMN Isoalloxazine Ring

It has been shown by crystallography [Gorman and Shapiro 2005] that planarity of isoalloxazine ring of oxidized FMN molecule is notably changed when FMN is double-reduced. The so-called butterfly effect has been proposed to play crucial role in defining binding specificity of active place of WrbA. In this short separate section we discuss the development of new FF parameters for planar (oxidized) and non-planar bended (double-reduced) FMN isoalloxazine ring. All new and adopted FF parameters are freely available in an electronic form and can be also found in YASARA FF file (amber99.fof). Four dihedral angles, dih1, dih2, dih3 and dih4, and two angles, a1 and a2, define the planarity of the isoalloxazine ring (Figure C-24). No analogy for these angles was found in the existing AMBER-like FFs [Cornel et al. 1995], and for all these angles new FF parameters have been developed by high level *ab initio* quantum-chemical calculations in Gaussian 98.

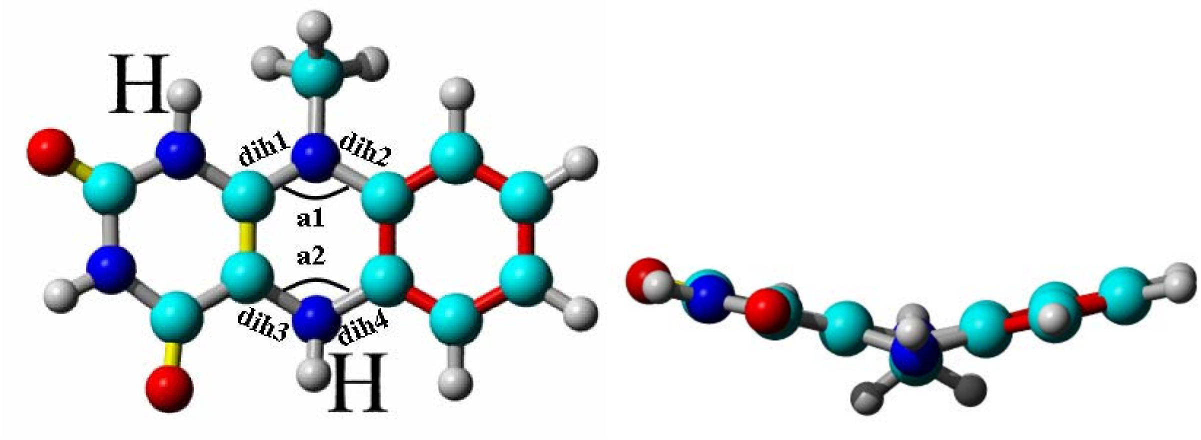

Figure C-24. Isoalloxazine ring of double-reduced flavinmononucleotide (FMN) shown as ball and stick model in element color (nitrogen in blue, carbon in cyan, oxygen in red, hydrogen in gray) with four dihedral angles, dih1, dih2, dih3 and dih4 and two angles, a1 and a2 highlighted. Top view (left) and side view (right). Note strongly non-planar double-reduced (two hydrogen atoms marked) form of isoalloxazine ring (right). Single bonds are in gray, double in yellow, aromatic in red. Geometry of the isoalloxazine ring shown here was optimized by *ab initio* (HF/6-31G*) quantum-chemical calculations in Gaussian 98.

Optimized geometries of oxidized and double-reduced form of FMN obtained by *ab initio* (HF/6-31G*) quantum-chemical calculations in Gaussian 98 are shown in the Figure C-25.

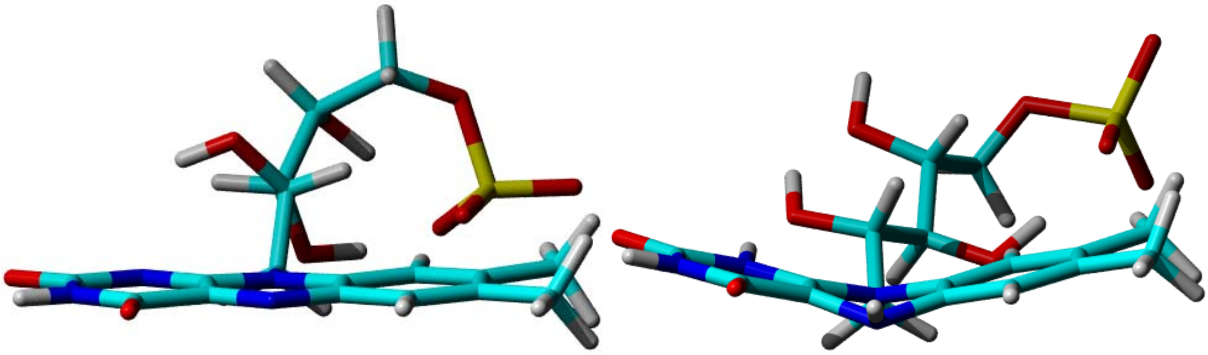

Figure C-25. Comparison of planarity of oxidized (left) and double-reduced (right) FMN shown as stick model in element color (nitrogen in blue, carbon in cyan, oxygen in red, hydrogen in gray, phosphorus in yellow). Geometries were obtained by *ab initio* (HF/6-31G*) quantum-chemical calculations in Gaussian 98.

C.3.2. Equilibrated WrbA Models

Six equilibrated WrbA models were constructed and prepared in YASARA. The abbreviations used for three models of WrbA tetrames are as follows; Tetramer (No FMN) for WrbA tetramer without FMN, Tetramer (FMS) for WrbA tetramer with oxidized FMN and Tetramer (FMR) for WrbA tetramer with double-reduced FMN. The abbreviations used for three models of WrbA monomers are as follows; Monomer (No FMN) for WrbA monomer without FMN, Monomer (FMS) for WrbA monomer with oxidized FMN and Monomer (FMR) for WrbA monomer with double-reduced FMN. All models were equilibrated by standard procedures described in detail in *Photosystem II* or *Chlorosomes* section of this thesis. Initial 3D molecular structure of tetrameric WrbA was transferred from experimental crystal structure from *E. coli* at 2.6 Å resolution [Carey et al. 2007] and adopted. The initial structure of WrbA was solvated in the simulation cell filled with water. The protonation of His, Asp and Glu residues was set by pKa prediction subroutine embedded in molecular modeling package YASARA [Yasara Biosciences, *http://www.yasara.org/index.html*; Krieger et al. 2004]. After cell neutralization the overall charge was zero. Optimization of the starting geometry of WrbA tetramer was performed by steepest descent minimization, followed by simulated annealing (at 100 K) and MD simulations with small time step 0.5 fs at 298 K. The equilibration process of WrbA models was finished when no changes in Cα RMSD were observed (approximately after 5 ns). The NPT ensemble was used during equilibration processes and also during subsequent MD simulations. Details from the MD simulations are as follows. For all MD simulations periodic conditions of simulation cell were applied. Time step of 1.0 fs for intramolecular and 2.0 fs for intermolecular forces was used. AMBER99 (release 2005) [Case et al. 2005] FF with new FF parameters developed for FMN was used. MD snapshots were saved after each 10 ps of MD simulation. Pressure control was applied (see documentation of YASARA). Cutoff 1.0 nm was used for Lennard-Jones and electrostatic interactions. To treat the long-range electrostatic interactions outside the cutoff region the Particle Mesh Ewald method [Essmann et al. 1995] was used. The temperature was adjusted by Berendsen thermostat [Berendsen et al. 1984] based on the time-averaged temperature.

The equilibrated Tetramer (FMR) and Monomer (FMR) models are shown in the Figure C-26. WrbA tetramer consist of two copies of identical WrbA dimers. Each WrbA dimer is formed by two protein chains, chain A and chain C and two FMN molecules. The protein chains of the second WrbA dimer are marked as chain A' and chain C' [Carey et al. 2007].

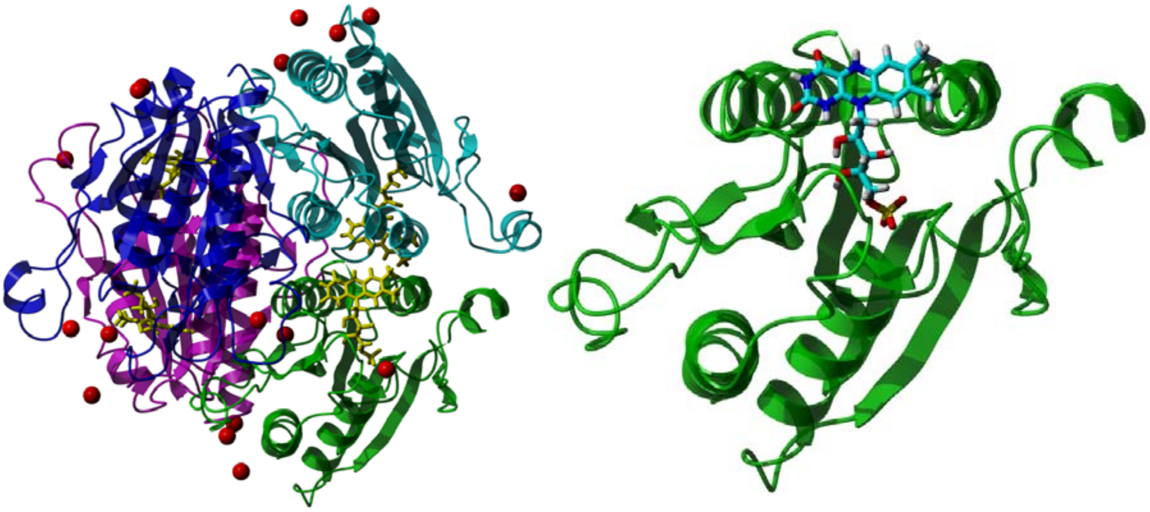

Figure C-26. Equilibrated models of WrbA tetramer (left) and WrbA monomer (right) in ribbon representation with double-reduced FMN molecules shown as stick model. Coloring scheme of WrbA tetramer (left) is as follows; chain A in green, chain C in cyan, chain A' in blue and chain C' in magenta, four double-reduced FMN molecules in yellow, sodium ions in red. Molecules of water and simulation cell are hidden for clarity. Molecule of double-reduced FMN of WrbA monomer (right) is shown in element color (nitrogen in blue, carbon in cyan, oxygen in red, hydrogen in gray, phosphorus in yellow). Pictures were rendered in Pov-Ray and prepared in YASARA.

C.3.3. RMSF (Preliminary Results from MD Simulations)

We have performed MD simulations of six WrbA models, three WrbA tetramers and three WrbA monomers. The structural and functional role of WrbA tetramerization is still under debate. By comparison of amino acids RMSF values of WrbA tetramers and WrbA monomers, we can discuss particular amino acids responsible for WrbA tetramer packing. Additionally, by comparing RMSF values calculated for WrbA models with oxidized FMN molecules and WrbA models with double-reduced FMN molecules, changes in flexibility of the amino acids forming the pocket for binding of FMN cofactor can be detected. These changes have been proposed [Carey et al. 2007] to play crucial role in the ping-pong mechanism. It has been proposed that external loop of each WrbA chain, Pro 44 - Gly 51, changes its conformation during change of oxidation state of FMN molecule during ping-pong mechanism. Further, also amino acids responsible for FMN molecule binding can be observed from calculation of RMSF values for all WrbA models. The RMSF values of three models of WrbA monomers and three models of WrbA tetramers calculated from 5 - 18 ns part of MD simulations are shown in the Figure C-27. In the case of WrbA tetramer models residua numbers from 1 to 197 represent chain A, residua numbers from 198 to 394 chain C, residua numbers from 395 to 591 chain A’ and finally residua numbers from 592 to 788 chain C’.

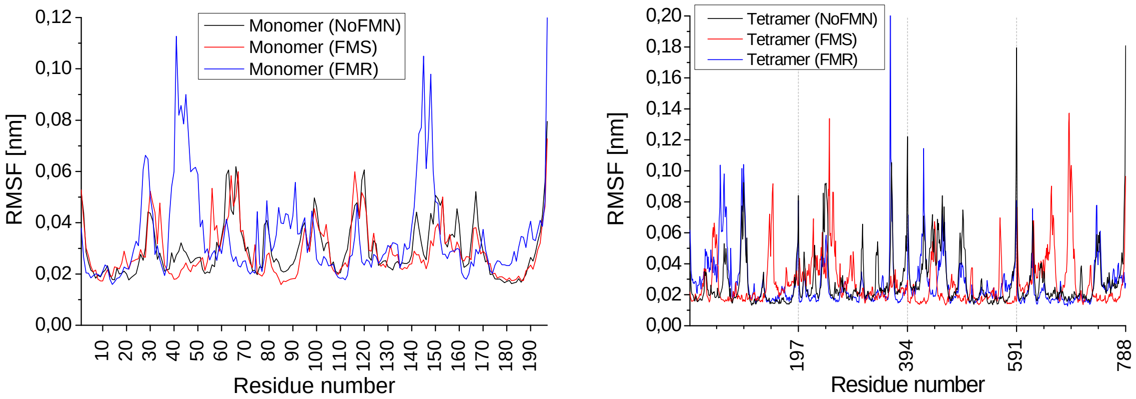

Figure C-27. RMSF values of three models of WrbA monomers (left) and three models of WrbA tetramers (right) calculated from 5 - 18 ns part of MD simulations. Details on abbreviation are given in the text. All WrbA models were prepared from 0.26 nm crystal structure of *E. coli* WrbA published recently [Carey et al. 2007] and MD simulations were performed in YASARA.

For better readability of the RMSF values of WrbA tetramer models, RMSF values are shown for all chains (A, C, A' and C') of WrbA tetramers in separate graphs in the Figure C-28.

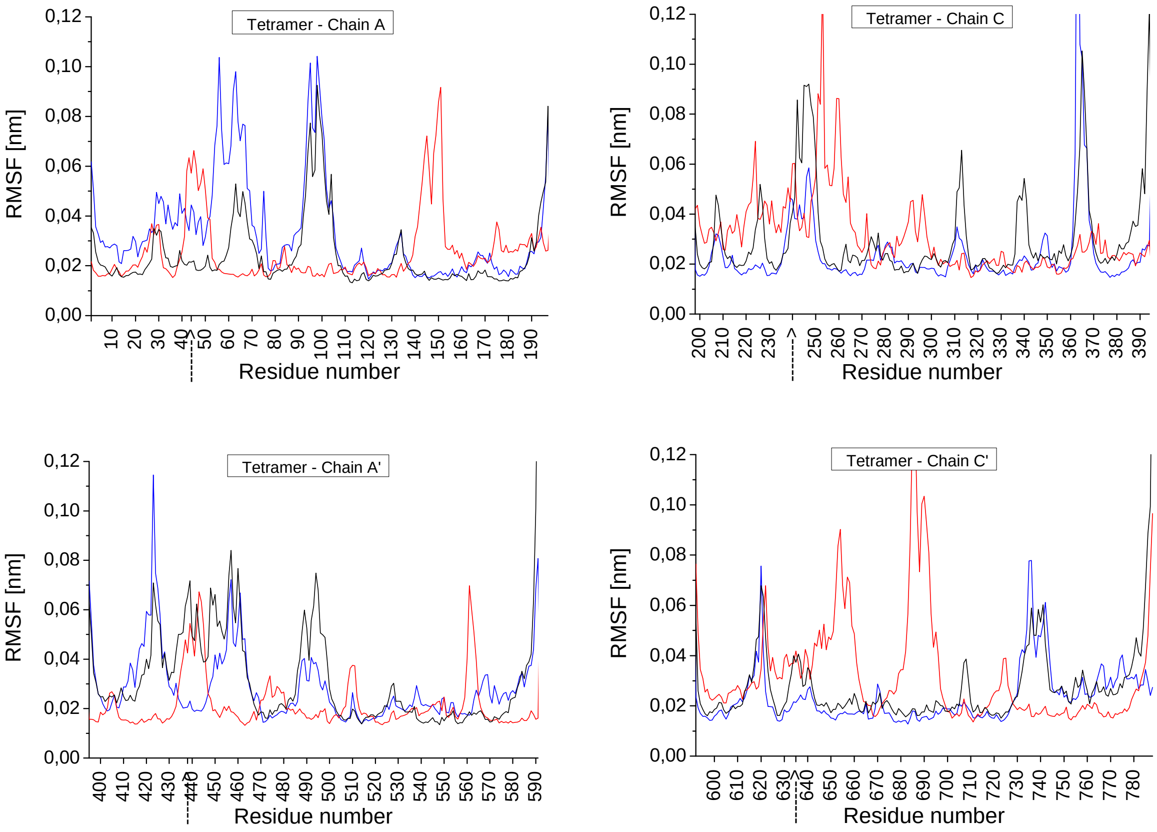

Figure C-28. RMSF values of three WrbA tetramer models divided into separate graphs for each of four chains (A, C, A' and C').calculated from 5 - 18 ns part of MD simulations performed in YASARA. Maxima of some RMSF values were cut for clarity (see Figure C-26 for full data). The "→" symbol highlights the position of Pro44.

CONCLUSIONS

Photosystem II

We have built complete equilibrated molecular model of photosystem II (PSII), which can be used as a starting structure for any other theoretical molecular modeling studies in the future. Complete set of new force field (FF) parameters for all photosynthetic pigments and other non-protein molecules of PSII have been developed by high level *ab initio* quantum-chemical calculations. Except for the FF parameters adopted from the existing FF sets, all represent required quality for any AMBER-like FF. The complete list of all FF parameters, also for molecules not presented in this thesis, is freely available at Institute of Physical Biology (Nove Hrady, CZ), in an electronic form adopted into YASARA FF file (amber99.fof). Six molecular dynamics (MD) simulations of “big” molecular model of photosytem II embedded in a simulation cell counting more than 200 000 atoms in overall duration of ~ 120 ns have been performed. The calculated MD trajectories have been analyzed by developed analysis macros. Subsequently, optical spectra of PSII reaction center (RC) have been calculated by using standard transition dipole-dipole approximation and also by more advanced transition point-monopole method. The calculated optical spectra of PSII RC were in very good accordance with the experimental analogues. The relevance of our molecular models of PSII was clearly confirmed. The temperature-dependent changes in experimental, and also in our calculated, difference absorption spectra were explained by theoretical molecular modeling approach. We may support experimental findings, proposed by our experimental group, that Pheo-D1 does not excitonically interact with the other chlorins of the PSII RC.

Moreover we would like to mention that, to our knowledge, only two similar theoretical studies, combining quantum-chemical calculations, molecular modeling techniques and advanced optical spectra calculations, performed on such large membrane pigment-protein complex such as photosystem II, have been published so far.

Chlorosomes

Due to “enormous” size of chlorosomes the only structures of chlorosomes are available from various theoretical studies. We have built the first theoretical molecular models of chlorosomes constructed as lamellar models in accordance with recently published data. All models were constructed by combination of quantum chemical calculations and subsequent molecular modeling techniques. In the first step, all missing FF parameters for bacterio-chlorophyll *c*

(BChl *c*) and chlorobactene were developed by high level *ab initio* quantum-chemical calculations and adopted into AMBER-like FF (amber99.fof). From the trial set of shorter (5 ns-long) MD simulations of ten equilibrated lamellar BChl *c* models we were able to found one of the key structural parameter defining the distance between BChl *c* planes. This parameter can be found in the literature (mostly from NMR studies) ranging from 0.30 nm to 0.45 nm. Our results clearly demonstrated that the actual value of this parameter is between 0.37 nm and 0.40 nm. Next, five additional parameters have been elucidated from the set of 30ns-long MD simulations of eight equilibrated lamellar BChl *c* models with and without inclusion of chlorobactene molecules. Differences between antiparallel and parallel lamellar models were discussed. The proposed positive effect of the chlorobactene molecules present in a half of our models on the overall model stability were not confirmed. Finally, we conclude that antiparallel BChl *c* dimers should be considered as the main building block for construction of chlorosome lamellar models proposed by our experimental group.

Flavoprotein WrbA

The final goal of the computational study of flavoprotein WrbA is to find and describe the actual function of the WrbA, which is still not known. We have prepared equilibrated molecular models of WrbA with oxidized flavin-mononucleotide (FMN), double-reduced FMN and without FMN by using the crystal structure of *E. coli* WrbA, recently published by our experimental group. We have developed new FF parameters for oxidized and double-reduced FMN molecules at the quality required by any AMBER-like FF and adopted them into YASARA FF file (amber99.fof). Preliminary results from six ~ 20 ns-long MD simulations, three on WrbA tetramers and three on WrbA monomers have been presented. The proposed “ping-pong” mechanism and structural-functional relationships with other flavoproteins will be investigated.

REFERENCES

Adams MA and Jia Z (2005) Structural and biochemical evidence for an enzymatic quinone redox cycle in *Escherichia coli*: identification of a novel quinol monooxygenase. J Biol Chem 280:8358–8363

Aliste MP, MacCallum JL and Tieleman DP (2003) Molecular dynamics simulations of Pentapeptides at Interfaces: Salt Bridge and Cation-pi Interactions. Biochemistry 42(30):8976-8987

Allen MP and Tildesley DJ (1987) Computer simulation of liquids. Clarendon Press, Oxford

Autenrieth F, Tajkhorshid E, Baudry J and Luthey-Schulten Z (2004) Classical force field parameters for the heme prosthetic group of cytochrome *c*. J Comput Chem 25:1613–1622

Avers CJ (1985) Molecular cell biology. Addison-Wesley, Reading, MA

Balaban TS, Tamiaki H and Holzwarth (2005) Chlorins programmed for self-assembly. Top Curr Chem 258:1–38

Barber J, Nield N, Morris EP and Hankamer B (1999) Subunit positioning in photosystem II revisited. Trends Biochem Sci 24:43–45

Bayley PM (1973) The analysis of circular dichroism of biomolecules. Prog Biophys 27:3–76

Bayly CI, Cieplak P, Cornell WD and Kollman PA (1993) A well-behaved electrostatic potential based method using charge restraints for deriving atomic charges: The RESP model. J Phys Chem 97(40):10269-10280

Becker WM (1986) The world of the cell. Benjamin Cummings Inc, Menlo Park, CA

Berendsen HJC, Postma JPM, vanGunsteren WF, DiNola A and Haak JR (1984) Molecular dynamics with coupling to an external bath. J Chem Phys 81(8):3684-3690

Biesiadka J, Loll B, Kern J, Irrgang KD and Zouni A (2004) Crystal structure of cyanobacterial photosystem II at 3.2 angstrom resolution: a closer look at the Mn-cluster. Phys Chem Chem Phys 6(20):4733-4736

Blankenship RE and Prince RC (1985) Excited-state redox potentials and the Z scheme of photosynthesis. Trends Biochem Sci 10:382–383

Blankenship RE, Olson JM and Miller M (1995) Antenna complexes from green photosynthetic bacteria. In anoxygenic photosynthetic bacteria. Blankenship RE, Madigan MT and Bauer CE, editors. Kluwer Academic Publisher, Dordrecht, The Netherlands pp399–435

Brooks BR, Bruccoleri RE, Olafson BD, States DJ, Swaminathan D and Karplus M (1983) CHARMM: A program for macromolecular energy, minimization and dynamics calculations. J Com Chem 4:187–217

Carey J, Brynda J, Wolfova J, Grandori R, Gustavsson T, Ettrich R and Kuta Smatanova I (2007) WrbA bridges bacterial flavodoxins and eukaryotic NAD(P)H:quinone oxidoreductases. Protein Science 16:1-5

Case DA, Cheatham TE 3rd, Darden T, Gohlke H, Luo R, Merz KM Jr, Onufriev A, Simmerling C, Wang B and Woods RJ (2005) The Amber biomolecular simulation programs. J Comput Chem 26(16):1668-1688

Case DA, Pearlman DA, Caldwell JW, Cheatham TE 3rd, Wang J, Ross WS, Simmerling CL, Darden TA, Merz KM, Stanton RV, Cheng AL, Vincent JJ, Crowley M, Tsui V, Gohlke H, Radmer RJ, Duan Y, Pitera J, Massova I, Seibel GL, Singh UC, Weiner PK and Kollman PA (2002) AMBER 7, University of California, San Francisco

Ceccarelli M, Procacci P and Marchi M (2003) An ab initio force field for the cofactors of bacterial photosynthesis. J Comput Chem 24(2):129-142

Cervantes FJ, De Bok FA, Duong-Dac T, Stams AJ, Lettinga G and Field JA (2002) Reduction of humic substances by halorespiring, sulphatereducing and methanogenic microorganisms. Environ Microbiol 4:51–57

Chang DE, Smalley DJ and Conway D (2002) Gene expression profiling of *Escherichia coli* growth transitions: an expanded stringent response model. Mol Microbiol 45:289–306

Chang JC (1977) Monopole effects on electronic excitation interactions between large molecules. I. Application to energy transfer in chlorophylls. J Chem Phys 67(9):3901–3909

Cheung KJ, Badarinarayana V, Selinger DW, Janse D and Church GM (2003) A microarray-based antibiotic screen identifies a regulatory role for supercoiling in the osmotic stress response of *Escherichia coli*. Genome Res 13:206–215

Cornell WD, Cieplak P, Bayly CI, Gould IR, Merz KM, Ferguson DM, Spellmeyer DC, Fox T, Caldwell JW and Kollman PA (1995) A 2nd generation force-field for the simulation of proteins, nucleic acids, and organic-molecules. J Amer Chem Soc 117(19):5179-5197

Darden T, Perera L, Li L and Pedersen L (1999) New tricks for modelers from the crystallography toolkit: the particle mesh Ewald algorithm and its use in nucleic acid simulations. Structure 7:R55-R60.

Deisenhofer J and Michel H (1989) The photosynthetic reaction center from the purple bacterium *Rhodopseudomonas viridis*. Science 245:1463–1473

Dekker JP and Van Grondelle R (2000) Primary charge separation in Photosystem II. Photosynth Res 63(3):195-208

Diner BA and Rappaport F (2002) Structure, dynamiscs and energetics of the primary photochemistry of Photosystem II of oxygenic photosynthesis. Annu Rev Plant Biol 53:551-580

Durrant JR, Klug DR, Kwa SL, van Grondelle R, Porter G and Dekker JP (1995) A multimer model for P680, the primary electron donor of Photosystem II. Proc Natl Acad Sci USA 92(11):4798-4802

Egawa A, Fujiwara T, Mizoguchi T, Kakitani Y, Koyama Y and Akutsu H (2007) Structure of the light-harvesting bacteriochlorophyll *c* assembly in chlorosomes from *Chlorobium limicola* determined by solid-state NMR. PNAS 104(3):790-795

Essmann U, Perera L, Berkowitz ML, Darden T, Lee H and Pedersen LG (1995) A smooth particle mesh Ewald method. J Chem Phys 103(19):8577-8593

Ewald P (1921) Die Berechnung optischer und elektrostatischer Gitterpotentiale. Ann Phys 64:253-287

Ferreira KN, Iverson TM, Maghlaoui K, Barber J and Iwata S (2004) Architecture of the photosynthetic oxygen-evolving center. Science 303(5665):1831-1838

Finneran KT, Forbush HM, Van Praagh CV and Lovley DR (2002) *Desulfitobacterium metallireducens* sp. nov., an anaerobic bacterium that couples growth to the reduction of metals and humic acids as well as chlorinated compounds. Int J Syst Evol Microbiol 52:1929–1935

Fletcher R (1980) Practical methods of optimization. John Wiley & Sons, New York

Foloppe N, Ferrand M, Breton J and Smith JC (1995) Structural model of the photosynthetic reaction center of *Rhodobacter capsulatus*. Proteins Struct Funct Genet 22:226–244

Frigaard NU, Chew AGM, Li H, Maresca JA and Bryant DA (2003) *Chlorobium tepidum*: insights into the structure, physiology and metabolism of a green sulfur bacterium derived from a complete genome sequence. Photosynth Res 78:93–117

Frisch MJ, Trucks GW, Schlegel HB, Scuseria GE, Robb MA, Cheeseman JR, Zakrzewski VG, Montgomery JA, Stratmann RE, Burant JC, Dapprich S, Millam JM, Daniels AD, Kudin KN, Strain MC, Farkas O, Tomasi J, Barone V, Cossi M, Cammi R, Mennucci B, Pomelli C, Adamo C, Clifford S, Ochterski J, Petersson GA, Ayala PY, Cui Q, Morokuma K, Malick DK, Rabuck AD, Raghavachari K, Foresman JB, Cioslowski J, Ortiz JV, Stefanov BB, Liu G, Liashenko A, Piskorz P, Komaromi I, Gomperts R, Martin RL, Fox DJ, Keith T, Al-Laham MA, Peng CY, Nanayakkara A, Gonzalez C, Challacombe M, Gill PMW, Johnson BG, Chen W, Wong MW, Andres JL, Head-Gordon M, Replogle ES and Pople JA (1998) Gausian 98. Gaussian Inc., Pittsburgh, PA

Garab G (1996) Advances in Photosynthesis, Biophysical Techniques in Photosynthesis. In: Amesz J and Hoff AJ (ed) Kluwer Academic Publishing, pp 11-40, Dordrecht

Gill PE, Murray W and Wright MH (1981) Practical optimization. Academic Press, Inc., New York

Gorman J and Shapiro L (2005) Crystal structures of the tryptophan repressor binding protein WrbA and complexes with flavin mononucleotide. Protein Sci 14:3004–3012

Grandori R and Carey J (1994) Six new candidate members of the α/β twisted open-sheet family detected by sequence similarity to flavodoxin. Protein Sci 3:2185–2193

Grandori R, Khalifah P, Boice JA, Fairman R, Giovanielli K and Carey J (1998) Biochemical characterization of WrbA, founding member of a new family of multimeric flavodoxin-like proteins. J Biol Chem 273:20960–20966

Green BR and Durnford DG (1996) The chlorophyllcarotenoid proteins of oxygenic photosynthesis. Annu Rev Plant Physiol Plant Mol Biol 47:685–714

Green BR and Parson WW (2003) Light-Harvesting Antennas in Photosynthesis. 1st edition, Kluwer Academic Publisher, Dordrecht, The Netherlands pp229–345

Grossman AR, Bhaya D, Apt KE and Kehoe DM (1995) Light-harvesting complexes in oxygenic photosynthesis: Diversity, control, and evolution. Annu Rev Genet 29:231–288

Hoganson CW and Babcock GT (1997) A metalloradical mechanism for the generation of oxygen from water in photosynthesis. Science 277:1953–1956

Hohenberg P and Kohn W (1964) Inhomogeneous electron gas. Phys Rev 136:B864–B871

Holzwarth AR and Schaffner K (1994) On the structure of bacteriochlorophyll molecular aggregates in the chlorosomes of green bacteria. A molecular modelling study. Photosynth Res 41:225–233

Jaiswal AK (2000) Regulation of genes encoding NAD(P)H: quinine oxidoreductases. Free Radic Biol Med 29:254–262

Jankowiak R, Hayes JM and Small GJ (2002) An excitonic pentamer model for the core Q(y) states of the isolated photosystem II reaction center. J Phys Cem B 106(34):8803-8814

Jensen KA, Ryan ZC, Van den Wymelenberg A, Cullen D and Hammel KE (2002) An NADH: quinone oxidoreductase active during biodegradation by the brown-rot basidiomycete *Gloeophyllum trabeum*. Appl Environ Microbiol 68:2699–2703

Jorgensen WL (1998) OPLS Force Fields. In Encyclopedia of computational chemistry, Schleyer R (ed.) Wiley, New York 3:1986–1989

Kakitani Y, Nagae H, Mizoguchi T, Egawa A, Akiba K, Fujiwara T, Akutsu H and Koyama Y (2006) Assembly of a mixture of isomeric BChl *c* from *Chlorobium limicola* as determined by intermolecular 13C-13C dipolar correlations: coexistence of dimer-based and pseudo-monomer-based stackings. Biochemistry 45(24):7574–85

Karplus M, Petsko GA (1990) Molecular dynamics simulations in biology. Nature 347:631–639

Konermann L and Holzwarth AR (1996) Analysis of the absorption spectrum of photosystem II reaction centers: temperature dependence, pigment assignment, and inhomogeneous broadening. Biochemistry 35(3):829–842

Konermann L, Gatzen G and Holzwarth AR (1997) Primary Processes and Structure of the Photosystem II Reaction Center. 5. Modeling of the Fluorescence Kinetics of the D1-D2-cyt-b559 Complex at 77 K. J Phys Chem B 101:2933-2944

Krawczyk S (1991) Electrochromism of chlorophyll-a monomer and special-pair dimer. Biochim Biophys Acta 1056(1):64-70

Krieger E, Darden T, Nabuurs SB, Finkelstein A and Vriend G (2004) Making optimal use of empirical energy functions: Force-field parameterization in crystal space. Proteins 57(4):678–683

Kuczera K, Kuriyan J and Karplus M (1990) Temperature dependence of the structure and dynamics of myoglobin: A simulation approach. J Mol Biol 213:351–373

Li R, Bianchet MA, Talalay P and Amzel LM (1995) The three-dimensional structure of NAD(P)H: quinone reductase, a flavoprotein involved in cancer chemoprotection and chemotherapy: mechanism of the two-electron reduction. Proc Natl Acad Sci USA (92):8846–8850

Lindahl E, Hess B and van der Spoel (2001) GROMACS: A package for molecular simulation and trajectory analysis. J Mol Mod 7:306-317

Loll B, Kern J, Saenger W, Zouni A and Biesiadka J (2005) Towards complete cofactor arrangement in the 3.0A resolution structure of photosystem II. Nature 438(7070):1040-1044

MacCallum JL and Tieleman DP (2006) Computer Simulation of the Distribution of Hexane in a Lipid Bilayer: Spatially Resolved Free Energy, Entropy, and Enthalpy Profiles. J Am Chem Soc 128(1):125-130

MacKerell AD (2004) Empirical force fields for biological macromolecules: overview and issues. J Comput Chem 25:1584–1604

MacKerell AD, Bashford D, Bellott M, Dunbrack RL, Evanseck JD, Field MJ, Fischer S, Gao J, Guo H, Ha S, Joseph-McCarthy D, Kuchnir L, Kuczera K, Lau FTK, Mattos C, Michnick S, Ngo T, Nguyen DT, Prodhom B, Reiher WE, Roux B, Schlenkrich M, Smith JC, Stote R, Straub J, Watanabe M, Wiorkiewicz-Kuczera J, Yin D and Karplus M (1998) All-atom empirical potential for molecular modeling and dynamics studies of proteins. J Phys Chem B (102):3586-3616

Martinez-Planells A, Arellano JB, Borrego CM, López-Iglesias C, Gich F and Garcia-Gil J (2002) Determination of the topography and biometry of chlorosomes by atomic force microscopy. Photosynthesis Research 71(1-2):83-90

Matyus E, Monticelli L, Kover KE, Xu Z, Blasko K, Fidy J and Tieleman DP (2006) Structural investigation of syringomycin-E using molecular dynamics simulation and NMR. Eur Biophys J 35(6):459-467

Montano GA, Bowen BP, LaBelle JT, Woodbury NW, Pizziconi VB and Blankenship R (2003) Characterization of *Chlorobium tepidum* chloromes: A calculation of bacteriochlorophyll *c* per chlorosome and oligomer modeling. Biophys J 85:2560–2565

Nozawa T, Ohtomo K, Suzuki M, Nakagawa H, Shikama Y, Konami H and Wang ZY (1994) Structures of chlorosomes and aggregated BChl *c* in *Chlorobium tepidum* from solid state high resolution CP/MAS ^{13}C NMR. Photosynth Res 41:211–233

Palencar P, Vacha F and Kuty M (2005) Force field development on pigments of photosystem 2 reaction centre. Photosynthetica 43(3):417-420

Patridge EV and Ferry JG (2006) WrbA from *Escherichia coli* and *Archaeoglobus fulgidus* is an NAD(P)H: quinone oxidoreductase. J Bacteriol 188(10):3498–506

Pearlstein RM (1991) Theoretical interpretation of antenna spectra. In: Scheer H (ed) Chlorophylls, pp1047-1078. CRC Press, Bocca Raton, FL

Phadtare S, Kato I and Inouye M (2002) DNA microarray analysis of the expression profile of *Escherichia coli* in response to treatment with 4,5-dihydroxy-2-cyclopenten-1-one. J Bacteriol 184:6725–6729

Pomposiello PJ, Bennik MH and Demple B (2001) Genome-wide transcriptional profiling of the *Escherichia coli* responses to superoxide stress and sodium salicylate. J Bacteriol 183:3890–3902

Prokhorenko VI and Holzwarth AR (2000) Primary processes and structure of the photosystem II reaction center: a photon echo study. J Phys Chem B 104(48):11563-11578

Psencik J, Ikonen TP, Laurinmäki P, Merckel MC, Butcher SJ, Serimaa RE and Tuma R (2004) Lamellar organization of pigments in chlorosomes, the light harvesting complexes of green photosynthetic bacteria. Biophys J 87(2):1165–72

Psencik J, Ma YZ, Arellano JB, Hala J and Gillbro T (2003) Excitation energy transfer dynamics and excited-state structure in chlorosomes of *Chlorobium phaeobacteroides*. Biophys J 84:1161–1179

Pullerits T (2000) Exciton states and relaxation in molecular aggregates: numerical study of photosynthetic light harvesting. J Chin Chem Soc 47(4A):773–784

Raszewski G, Saenger W and Renger T (2005) Theory of optical spectra of photosystem II reaction centers: location of the triplet state and the identity of the primary electron donor. Biophys J 88(2):986–998

Renger T and Marcus RA (2002) Photophysical properties of PS-2 reaction centers and a discrepancy in exciton relaxation times. J Phys Chem B 106(7):1809-1819

Roothan CCJ (1951) New developments in molecular orbital theory. Rev Mod Phys 23:69–73

Sauer K, Cogdell RJ, Prince SM, Freer A, Isaacs NW and Scheer H (1996) Structure-based calculations of the optical spectra of the LH2 bacteriochlorophyll-protein complex from *Rhodopseudomonas acidophila*. Photochem Photobiol 64(3):564–576

Sayle RA and Milner-White EJ (1995) RASMOL: biomolecular graphics for all. Trends Biochem Sci 20(9):374

Schubert WD, Klukas O, Saenger W, Witt HT, Fromme P and Krauss N (1998) A common ancestor for oxygenic and anoxygenic photosynthetic systems: a comparison based on the structural model of photosystem I. J Mol Biol 280(2):297-314

Staehelin LA, Golecki JR and Drews G (1980) Supramolecular organization of chlorosome (*Chlorobium* vesicles) and of their membrane attachment site in *Chlorobium limicola*. Biochim Biophys Acta 589:30–45

Staehelin LA, Golecki JR, Fuller RC and Drews G (1978) Visualization of the supramolecular architecture of chlorosome (*Chlorobium* type vesicles) in freeze-fractured cells of *Chloroflexus aurantiacus*. Arch Microbiol 119:269–277

Steffen MA, Lao KQ and Boxer SG (1994) Dielectric asymmetry in the photosynthetic reaction center. Science 264(5160):810-816

Stockner T, Ash WL, MacCallum JL and Tieleman DP (2004) Direct simulation of transmembrane helix association: role of asparagines. Biophys J 87(3):1650-1656

Szabo A and Ostlund NS (1996) Modern quantum chemistry. Macmillan, New York

Taiz L and Zeiger E (2006) Plant Physiology. 4th edition, Sinauer Associates Inc, Sunderland MA, pp764

Tieleman DP (2006) Computer simulations of transport through membranes: passive diffusion, pores, channels and transporters. Clin Exp Pharmacol Physiol 33(10):893-903

Tieleman DP, Berendsen HJ and Sansom MS (2001) Voltage-dependent insertion of alamethicin at phospholipid/water and octane/water interfaces. Biophys J 80(1):331-346

Tsai HH and Simpson MC (2003) HBFF-SVD force field treatment of Ni(II) porphine: Important long range cross terms. J Phys Chem A107:526–541

Tucker DL, Tucker N and Conway T (2002) Gene expression profiling of the pH response in *Escherichia coli*. J Bacteriol 184:6551–6558

Vacha F, Durchan M and Siffel P (2002) Excitonic interactions in the reaction centre of Photosystem II studied by using circular dichroism. Biochim Biophys Acta 1554:147-152

Vacha F, Joseph DM, Durrant JR, Telfer A, Klug DR, Porter G and Barber J (1995) Photochemistry and spectroscopy of a five-chlorophyll reaction center of Photosystem II isolated by using a Cu affinity column. Proc Natl Acad Sci USA 92(7):2929-2933

Vacha F, Psencik J, Kuty M, Durchan M and Siffel P(2005) Evidence for localization of accumulated chlorophyll cation on the D1-accessory chlorophyll in the reaction centre of Photosystem II. Photosynth Res 84:297-302

Van Gunsteren WF, Berendsen HJC (1990) Computer simulation of molecular dynamics – methodology, applications, and perspectives in chemistry. Angewandte Chemie, International Edition in English 29:992–1023

Van Gunsteren WF, Daura X and Mark AE (1998) GROMOS force field. In: Encyclopaedia of Computational Chemistry 2, pp1211-1216 CRC Press, FL

Van Rossum BJ, Steensgaard DB, Mulder FM, Boender GJ, Schaffner K, Holzwarth AR and De Groot HM (2001) A refined model of the chlorosomal antennae of the green bacterium *Chlorobium tepidum* from proton chemical shift constraints obtained with high-field 2-D and 3-D MAS NMR dipolar correlation spectroscopy. Biochemistry 40:1587–1595

Vasilev S and Bruce D (2006) A protein dynamics study of Photosystem II: the effects of protein conformation on reaction center function. Biophys J 90(9):3062-3073

Vriend G (1990) WHAT IF: a molecular modeling and drug design program. J Mol Graph 8(1):52-56

Wang JM, Cieplak P and Kollman PA (2000) How well does a restrained electrostatic potential (RESP) model perform in calculating conformational energies of organic and biological molecules? J Comp Chem 21(12):1049-1074

Wang ZY, Umetsu M, Kobayashi M and Nozawa T (1999) Complete assignment of H^1 NMR spectra and structural analysis of intact bacteriochlorophyll *c* dimer in solution. J Phys Chem B 103:3742–3753

Warshel A and Parson WW (1987) Spectroscopic properties of photosynthetic reaction centers. I. Theory. J Am Chem Soc 109:6143-6152

Wrobel RL (2002) Heterologous expression and biochemical characterization of an NAD(P)H: quinone oxidoreductase from the hemiparasitic plant *Triphysaria versicolor*. Plant Physiol Biochem 40:265–272

Yang W, Ni L and Somerville R (1993) A stationary-phase protein of *Escherichia coli* that affects the mode of association between the *trp* repressor protein and operator-bearing DNA. Proc Natl Acad Sci USA 90:5796–5800

Zouni A, Witt H-T, Kern J, Fromme P, Krauss N, Saenger W and Orth P (2001) Crystal structure of photosystem II from *Synechococcus elongatus* at 3.8 Å resolution. Nature 409:739–743

APPENDIX

PIGMENTS - ATOM NAMES

The Figure C-29 represent dynamic molecular structures of non-protein molecules, mostly pigment molecules, for which new topology files (without connectivities) were developed and are shown in chapter *Results and Discussion*. Atom names and numbers are given for all heavy atoms (hydrogen atoms are hidden for clarity) in accordance with the above mentioned topology files with respect to the PDB original atom (www.pdb.org) names. In the figures the orders of bonds are clearly distinguished by different colors. Single bonds are represented by white sticks, aromatic bonds by red sticks, and double bonds are shown as yellow sticks.

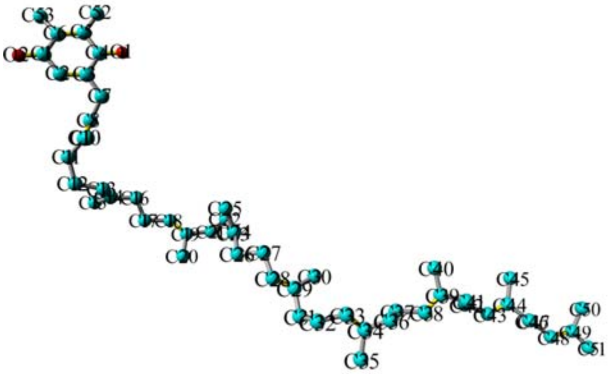

Plastoquinone 9 – **PQ9**

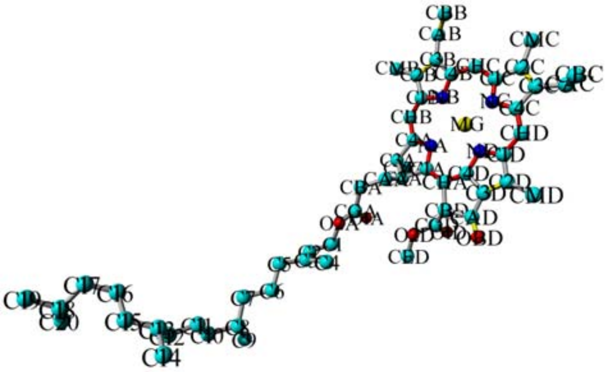

Chlorophyll *a* – **Chl *a***

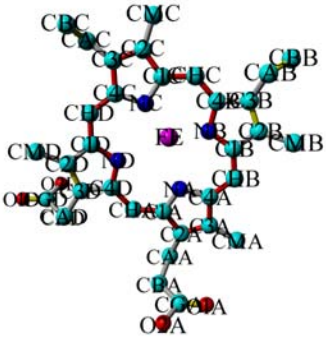

Heme – **Heme**

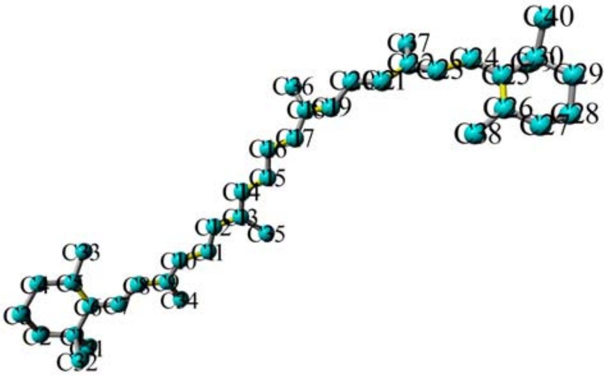

β-carotene – ***β*-Car**

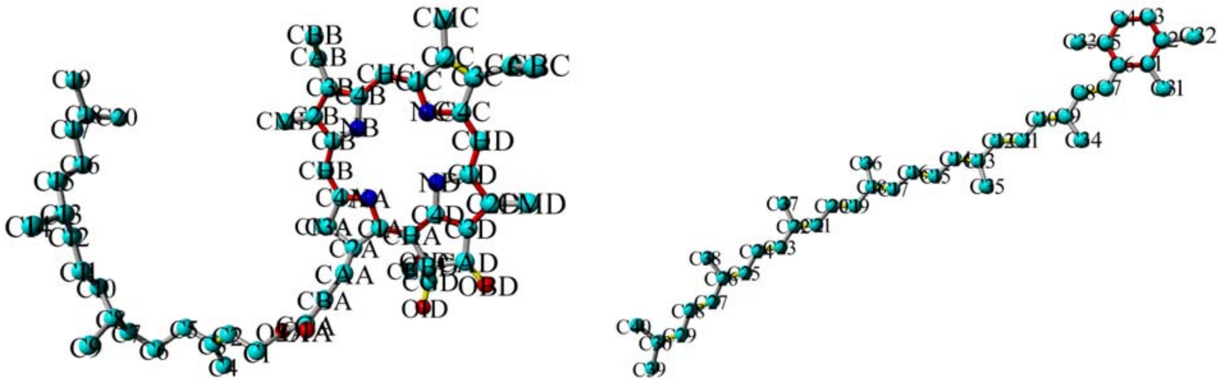

Pheophytin *a* **– Pheo *a***

Chlorobactene **– CBE**

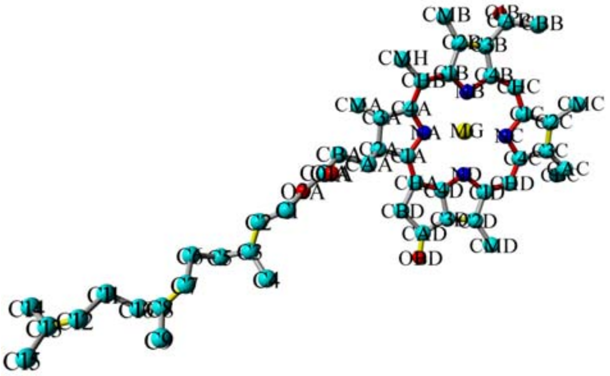

Bacteriochlorophyll *c* (R_EM) **– BChl *c***

Figure C-29. Molecular structures of non-protein molecules shown as ball and stick model in element color (nitrogen in blue, carbon in cyan, oxygen in red, hydrogen in gray) with atom name labels given for all heavy atoms (hydrogen atoms are hidden for clarity). Single bonds are in gray, double in yellow and aromatic in red. The picture was rendered in Pov-Ray and prepared in YASARA. Geometries of all molecules represent dynamic structures taken directly from MD simulation snapshots at 298 K, therefore thermal fluctuations are present.

PUBLICATIONS

The results presented in the thesis were published in the following papers:

1. Palencar P, Vacha F and Kuty M (2005) Force field development on pigments of photosystem 2 reaction centre. Photosynthetica 43(3):417-420
2. Palencar P, Psencik J, Prudnikova T, Vacha F and Kuty M (2007) The effects of light induced reduction of the Photosystem II reaction center, a theoretical study. Submitted to Photosynth Res 15 pp
3. Prudnikova T, Kuty M, Gavira JA, Palencar P, Vacha F, Rezacova P, Garcia-Ruiz JM and Kuta Smatanova I (2007) Crystallization and structure-functional study of photosystem II from higher plants. Materials Structure 14(1):5-7
4. Kuta Smatanova I, Wolfova J, Brynda J, Lapkouski M, Ettrich RH, Palencar P, Kuty M, Mesters JR, Grandori R and Carey J. Crystal structure of *E. coli* WrbA in complex with FMN. In preparation for J Cryst Growth
5. Palencar P, Kuty M, Doglia SM, Kuta Smatanova I, Wolfova J, Grandori R, Carey J and Ettrich RH. Influence of FMN binding on oligomerisation and stabilization of *E. coli* WrbA investigated by molecular dynamics simulations. In preparation

Lectures and poster presentations at conferences and congresses:

1. Palencar P, Vacha F and Kuty M (2005) Structure and dynamics of the photosystem II reaction center pigment-protein complex. FEBS J 272:452 30th FEBS Congress - 9th IUBMB Conference, Budapest, Hungary – poster
2. Palencar P, Vacha F and Kuty M (2005) Konformacni studium pigment-proteinoveho komplexu reakcniho centra fotosystemu II. Chem Listy 99:376 V. Mezioborove setkani mladych biologu, biochemniku a chemiku, Zdarske vrchy, Czech Republic – poster
3. Palencar P, Vacha F and Kuty M (2005) The role of pigments of photosystem II reaction center, a computational study. SSB4, Nove Hrady, Czech Republic – lecture
4. Palencar P, Kuty M and Vacha F (2006) Refined structural model of photosystem II from *Thermosynechococcus elongatus*, structural changes in reaction center. Acta Cryst A62:30 23rd European Crystallographic Meeting, Leuven, Belgium – lecture and poster
5. Kuty M, Palencar P and Vacha F (2005) Force field parameters for the PS II reaction center. Acta Cryst A61:C167 XX Congress of IUCr, Florence, Italy – poster

6. Palencar P, Vacha F and Kuty M (2006) Crystal structure of photosystem II from *Thermosynechococcus elongatus* refined by computational methods. Materials Structure 13(3):144 Colloquium 2006, Grenoble, France – poster
7. Kuty M, Palencar P and Psencik J (2006) Photosynthetic reaction centre and chlorosomal pigments. A computational study. Materials Structure 13(1):25 SSB5, Nove Hrady – poster
8. Palencar P, Vacha F and Kuty M (2006) Crystal structure of photosystem II from *Thermosynechococcus elongatus* refined and studied by molecular dynamics. Materials Structure 13(1):11 SSB5, Nove Hrady, Czech Republic – lecture
9. Kulik N, Palencar P, Kuty M, Kren V, Bezouska K and Ettrich R (2007) Molecular dynamics: Molecular docking simulation of substrates and inhibitors of beta-n-acetylhexosaminidase of *Aspergillus Oryzae*. Materials Structure 14(1):39 SSB6, Nove Hrady, Czech Republic – poster
10. Palencar P and Kuty M (2007) Excitonic interactions of photosystem II reaction center studied by molecular modeling techniques. Materials Structure 14(1):42 SSB6, Nove Hrady, Czech Republic – poster
11. Prudnikova T, Kuty M, Gavira JA, Palencar P, Vacha F, Rezacova P, Garcia-Ruiz JM and Kuta Smatanova I (2007) Structural and functional studies of higher plants photosystem II. Struktura 2007, Dvur Kralove, Czech Republic – lecture

PHOTOSYNTHETICA 43 (3): 417-420, 2005

BRIEF COMMUNICATION

Force field development on pigments of photosystem 2 reaction centre

P. PALENČÁR[*], F. VÁCHA[*,***,+], and M. KUTÝ[*,**]

Institute of Physical Biology, University of South Bohemia, Zámek 136, 37333 Nové Hrady, Czech Republic[*]
Institute of Landscape Ecology, Academy of Sciences of the Czech Republic,
Zámek 136, 37333 Nové Hrady, Czech Republic[**]
Institute of Plant Molecular Biology, Academy of Sciences of the Czech Republic,
Branišovská 31, 370 05 České Budějovice, Czech Republic[***]

Abstract

We developed new parameters for molecular dynamics (MD) simulations, namely partial atomic charges, equilibrium bond-lengths, angles, dihedrals, atom types, and force constants of chlorophyll *a* (Chl) and plastoquinone (PQ), and both reduced and neutral form of primary acceptor (PHO) molecule. These parameters are essential for MD simulations that can interpret various structure functional relationships during primary processes of charge separation and stabilization in photosystem 2 reaction centres.

Additional key words: chlorophyll; photosystem 2; plastoquinone.

Photosystem 2 (PS2) is a pigment-protein complex located in thylakoid membrane of cyanobacteria, algae, and higher plants. It performs series of light driven reactions, which result in a separation of charge and subsequently in a reduction of an electron-transport chain and water oxidation. Primary site of the energy conversion is located in so-called reaction centre (RC).

Recently, changes in excitonic interactions of PS2 RC pigments upon light-induced oxidation of primary donor (P680) or reduction of primary acceptor PHO were analyzed using absorption and circular dichroism (CD) spectra (Vácha *et al.* 2002). In contrast to the oxidation of primary donor, the light-induced change in the CD spectrum upon primary acceptor reduction was temperature-dependent. This suggests a hypothesis that at a room temperature the reduced PHO induces conformational changes of the RC protein environment, which affects the excitonic interaction of the RC chlorophylls (Chls).

Molecular modelling method such as MD (Allen and Tildesley 1987) coupled with quantum chemistry is a powerful tool for understanding and interpreting the upper mentioned optical spectra experiments (Vácha *et al.* 2005). Having chemically well defined three-dimensional (3D) molecular structure (Ferreira *et al.* 2004) and so-called force field (FF) parameters (MacKerell 2004), conformational study of the PS2 RC can be performed consequently by using MD technique.

Various calculations with different methods have been performed in order to obtain reliable collection of FF parameters for the cofactors of bacterial and higher plant RCs (Brooks *et al.* 1983, Kuczera *et al.* 1990, Foloppe *et al.* 1995, Ceccarelli *et al.* 2003, Tsai and Simpson 2003, Autenrieth *et al.* 2004). Currently, the most extensive bio-molecular FFs are the CHARMM22 (Chemistry at HARvard Molecular Mechanics, version *22*) (MacKerell *et al.* 1998) and CHARMM27. These include proteins, nucleic acids, lipids and, although limited, saccharides (MacKerell 2004). For the MD simulations on PS2 RC the present CHARMM22 and CHARM27 FF parameters are not fully applicable. Therefore, in this work we have focused on developing new CHARMM FF parameters, namely partial atomic charges, equilibrium bond-lengths, angles, dihedrals, atom types, and force constants of the PS2 RC pigments (Chl), plastoquinone (PQ), and both reduced and neutral forms of PHO molecule.

Received 14 February 2005, *accepted* 11 April 2005.

[+] Corresponding author; fax: +420 387 772 371, e-mail: vacha@jcu.cz

Acknowledgement: This research was supported by the Ministry of Education, Youth and Sports of the Czech Republic (MSM6007665808, GACR206/02/D177) and by the Academy of Sciences of the Czech Republic (Institutional research concept AVOZ60870520 and AV0Z50510513).

Submitted to PHOTOSYNTHESIS RESEARCH 15 pp, 2007

Regular paper

The effects of light induced reduction of the Photosystem II reaction center, a theoretical study

Peter Palencar[1,2], Jakub Psencik[1,3], Tatyana Prudnikova[1], Frantisek Vacha[1,4], Michal Kuty[1,2*]

[1]Institute of Physical Biology, University of South Bohemia, Zamek 136, 37333 Nove Hrady, Czech Republic; [2]Institute of Systems Biology and Ecology, Academy of Sciences of the Czech Republic, Zamek 136, 37333 Nove Hrady, Czech Republic; [3]Department of Chemical Physics and Optics, Faculty of Mathematics and Physics, Charles University, 121 16 Prague, Czech Republic; [4]Biological centre, Academy of Sciences of the Czech Republic, Branisovska 31, 370 05 Ceske Budejovice, Czech Republic;

**Author for correspondence (e-mail: kuty@ufb.jcu.cz and vacha@jcu.cz, tel: +420-777729592; fax: +420-386361279)*

Keywords: absorption spectra, chlorophyll, pheophytin, photosystem II, conformational analysis, exciton interactions, molecular dynamics, pigment-protein complex, reaction center

Abstract

Characteristic absorbance and circular dichroism (CD) spectral bleaching of the Photosystem II reaction centre (PSII RC) is observed when the primary electron acceptor, active pheophytin *a* (Pheo-D1), is selectively reduced using anaerobic illumination in the presence of artificial electron donor. With respect to the temperature dependence of the light-induced absorbance and CD bleaching we suggested that Pheo-D1 does not participate in the Qy exciton multimer. The combination of molecular dynamics (MD) simulations and optical spectra calculations is one of the relevant methods that could be used to explain experimental results concerning the light-induced processes in PSII RC. A set of MD simulations performed under 298 K over 20 ns revealed small conformational changes of a protein environment in proximity of reduced Pheo-D1 and also displacement of D1-branch chlorines from their original positions. These charge-induced processes were not observed at low temperature (77 K) MD simulations. The resulting theoretical absorption difference (light minus dark) spectra of equilibrated PSII RC models were highly consistent with our previous experiments in which significant light-induced bleaching of PSII RC absorbance spectrum was observable at 298K.

Abbreviations: PSII – photosystem 2; RC – reaction center; Eq-PSII RC – equilibrated photosystem 2; D1 – PSII protein subunit A, *psbA* gene product; D2 – PSII protein subunit D, *psbD* gene product; Chl-*a* – chlorophyll *a*; Pheo *a* – pheophytin *a*; *β*-Car – *β*-carotene; PQ9 – plastoquinone 9; BCT – bicarbonate ion; OEC – oxygen evolving complex; PSII RC pigments – Chl-*a*-3, Chl-*a*-4, Chl-*a*-5, Chl-*a*-6, Pheo-*a*-7, Pheo-*a*-8, Chl-*a*-9 and Chl-*a*-10; MM – molecular modeling; QM – quantum mechanics; HF – Hartree-Fock; RESP – restrained electrostatic potential; MD – molecular dynamics; Neutral-MD – MD of PSII RC with neutral pigments; Pheo^{-}-MD – MD of PSII RC with reduced Pheo-D1; FF – force field; RMSD – root-mean-square deviation; CD – circular dichroism; FWHM – full-width at half maximum; PDB ID – identification code from protein data bank *www.pdb.org*.

Introduction

Photosystem II (PSII) is one of several protein assemblies that function cooperatively in photosynthesis. In spite of great progress in study of the molecular structure and protein composition of PSII by an electron microscopy and X-ray crystallographic analysis, the resolution is too low (up to 3.0 Å) to see individual atoms so far (Loll et al. 2005; Biesiadka et al. 2004; Ferreira et al. 2004, Kamiya and Shen 2003, Zouni et al. 2001). As more structural data on PSII become available, new questions arose, ranging from details on the intermolecular interactions to the processes that convert light to chemical energy. Many discussions have been concerned with the nature of the so-called exciton interactions between the PSII RC chlorin pigments (chlorophyll *a* and pheophytin *a*). The exciton interactions (delocalization of the excited states) are caused by dipole-dipole coupling between proximal pigments and are important for photosynthetic function in defining the precursor state to the initial charge separation. The exciton interactions can be essential in the interpretation of experimental results because they can strongly influence ferritin and has been re-discovered as a useful agent to promote crystallization or to increase diffraction quality in a number of cases [Trakhanov 1998]. However, even with a mechanistic explanation of this effect, no rational prediction regarding the probability of success – except statistical evidence – is available!

The specific morphology of thaumatin and cytochrome crystals may depend on factors such as the source of material used during crystal growth and chemicals in the crystallizing buffer in the mother liquor, or on the mother liquor itself. For a single crystal form the angles between the faces are constant, but this is not true if the crystals belong to the different crystal forms such as tetragonal bipyramids and hexagonal prisms as in thaumatin. Their appearance depends on the use of metal salt cations, such as cupric chloride, and partially on the buffer and the precipitating agent used. We assume these metal ions influence evaporation in the protein drop even if they are absent from that drop. As this effect was tested on two different proteins only, we cannot speculate about how universally applicable this will be. However, the influence of Cu^{2+} ions on cytochrome crystal growth appears to be specific, because no other successful combination of ion salts with cytochrome was found among these four salts singly or in pairs. A similar effect was observed even in thaumatin crystallization when conditions with cupric chloride produced thaumatin crystals with a different morphology. The combination of four particular salts that promote crystallization can be quite reproducible also with other chemicals or even other volumes of the same drop in the remaining drop chambers.

References

1. I. Tomčová, R.M.M. Branca, G. Bodó, Cs. Bagyinka, I. Kutá Smatanová, *Acta Cryst.* **F62** (2006) 820-824.
2. A. McPherson, Crystallization of biological macromolecules, Cold Spring Harbor laboratory press, New York, 1999.
3. T.M. Bergfors, Protein crystallization: Techniques, strategies and tips, International University Line, La Jolla, USA, 1999.
4. A. McPherson, J. Weickmann, *J. Biomolecular Structure & Dynamics* **7** (1990) 1053-1060.
5. J. Jancarik, R. Pufan, C. Hong, S.H. Kim, R. Kim, *Acta. Crystal. Sec.* **D60** (2004) 1670-1673.
6. H. Sigel, A. Sigel, Metal ions in biological systems, Marcel Dekker - Taylor & Francis - CRC, California, USA, 1990.

Acknowledgements

This work is supported by grants MSM6007665808 and LC06010 of the Ministry of Education of the Czech Republic and Institutional research concept AVOZ60870520 of Academy of Sciences of the Czech Republic to I.K.S.

CRYSTALLIZATION AND STRUCTURE - FUNCTIONAL STUDY OF PHOTOSYSTEM II FROM HIGHER PLANTS

Tatyana Prudnikova[1], Michal Kutý[1,2], José A. Gavira[3], Peter Palenčár[1], František Vácha[1,5], Pavlína Řezáčová[4], Juan M. García-Ruiz[3] and Ivana Kutá Smatanová[1,2]

[1]Institute of Physical Biology USB CB, Zamek 136, 373 33 Nove Hrady, Czech Republic
[2]Institute of Systems Biology and Ecology AS CR, Zamek 136, 373 33 Nove Hrady, Czech Republic
[3]Laboratorio de Estudios Cristalografico, Edf. Lopez Neira, P.T. Ciencias de la Salud, Avenida del Conocimiento, s/n, 18100 Armilla, Granada, Spain
[4]Institute of Molecular Genetics AS CR, Flemingovo n. 2, 16637 Prague, Czech Republic, current address: Dep. Biochemistry, UT Southwestern Medical Center, 5323 Harry Hines Boulevard, Dallas, Texas 75390-8816
[5]Biological Centre IPMB AS CR, Branisovska 31, 370 05 Ceske Budejovice, Czech Republic
ivas@greentech.cz

Keywords

Photosystem II, reaction center, counter-diffusion method, vapor diffusion, membrane protein, absorption spectra, precipitation, exciton interaction, transition monopoles, transition dipole moments.

Abstract

Oxygen-evolving complex of photosystem II was crystallized using both counter-diffusion method and common vapor diffusion techniques. Absorption spectra of Photosystem II (PS II) reaction centres (RC) upon reduction of primary acceptor pheophytin of the D1 protein subunit were studied and compared with spectra calculated on the basis of Exciton Limit (Matrix Method).

Introduction

Photosynthesis realized by photosystem II (PSII) uses light energy to couple the formation of molecular oxygen to the fixation of carbon dioxide. This process simultaneously generates an aerobic atmosphere and produces a readily usable carbon source, both of which act to sustain almost all life on this planet. PS II is located in the thylakoid membrane of higher plants, algae and cyanobacteria. Its function to capture sunlight is realized by two antenna proteins CP47 and CP43. They transfer the excitation energy from the antenna system to the photochemical reaction center (RC) with primary electron donor P680, which is formed by chlorophyll *a* (Chl *a*) molecules is exited to P680*, followed by release of an electron that travels along the electron transfer chain [1, 2]. This large multisubunits